Master of Science Thesis

# Numerical investigation of an upper airway in a patient suffering from stridor

## A fluid-structure-acoustic interaction simulation in OpenFOAM®

**W.C.P. van der Velden**

November 16, 2012

Faculty of Aerospace Engineering

Delft University of Technology

# Numerical investigation of an upper airway in a patient suffering from stridor

## A fluid-structure-acoustic interaction simulation in OpenFOAM®

Master of Science Thesis

For obtaining the degree of Master of Science in Aerospace Engineering
at Delft University of Technology

W.C.P. van der Velden

November 16, 2012

Faculty of Aerospace Engineering · Delft University of Technology

**Delft University of Technology**

DELFT UNIVERSITY OF TECHNOLOGY
DEPARTMENT OF AERODYNAMICS

The undersigned hereby certify that they have read and recommend to the Faculty of Aerospace Engineering for acceptance the thesis entitled **“Numerical investigation of an upper airway in a patient suffering from stridor”** by **W.C.P. van der Velden** in fulfillment of the requirements for the degree of **Master of Science**.

Dated: November 16, 2012

Supervisors:

Prof. dr. ir. drs. H. Bijl

Dr. ir. A.H. van Zuijlen

Dr. H.L.J. Hoeve

Dr. ir. A.T. de Jong

*"... as Sir Cyril Hinshelwood has observed ... fluid dynamicists were divided into hydraulic engineers who observed things that could not be explained and mathematicians who explained things that could not be observed."*

Sir James Lighthill (1924-1998)

# Preface

This report is written as the final part of obtaining a Master's degree in Aerodynamics at the faculty of Aerospace Engineering at the Delft University of Technology. This report presents, demonstrate and describes the work of my final thesis study under the professional supervision of Prof. dr. ir. drs. H. Bijl and Dr. ir. A.H. van Zuijlen.

A multidisciplinary study is the keyword for this final thesis. Imagine a Master's thesis combining both medical and technical attributes. This is absolutely rare at the Aerodynamics department. On top of that, imagine a study combining the fluid flow, acoustic and structural analysis. This results in a combination of a study which has never been proposed before. This Master's thesis change this, by contributing in the numerical simulation areas of all topics. An acoustic simulation of a human upper airway in a patient suffering from stridor will be derived from a fluid flow and structure simulation. Different theories currently exists for each different field of study. However, this thesis tries to combine all theories, into one new theory.

First of all, I wish to thank my supervisors Prof. dr. ir. drs. H. (Hester) Bijl and Dr. ir. A.H. (Alexander) van Zuijlen from Delft University of Technology for their enthusiastic supervision. I learned a lot about scientific work and research, and Hester and Alexander really helped me with the difficulties I experienced during my thesis. They always stay critical, thereby keeping high expectations. Also, I would thank Dr. H.L.J. (Hans) Hoeve from Sophia Children's Hospital, Erasmus Medical Centre Rotterdam, for helping me with the medical part of this thesis. Thanks to Hans, medical papers and pictures made sense. Next, I would like to thank Prof. dr. sc. dipl. ing. H. (Hrvoje) Jasak, also known as the founding father of OpenFOAM®. Hrvoje helped me with difficult programming issues and guided me in the correct direction. Also thanks for Dr. ir. A.T. (Arjen) de Jong. Arjen was the acoustic specialist, helping me with some of my acoustic problems.

I also take this opportunity to thank my dear parents, brother and sister, friends and my girlfriend Lindsay, for their constant encouragement, support and patience during the stressful times. Especially my parents, Cees and Anne, for making studying possible.

Thank you all!

# Summary

In this master thesis, the numerical investigation of an upper airway in a patient suffering from stridor is investigated using a fluid-structure-acoustic interaction simulation in OpenFOAM®. The geometry of an upper airway model is very difficult, leading to various cross sections and a large spectrum of flow phenomena. Many flow forms were discovered during the analysis, such as flow separation, flow attachment, laminar flow, transitional flow and turbulent flow. Next, there is a large difference in geometry per patient, especially with respect to the age. Neonates and adults have different upper airway's, making a comparison very difficult. Also, taking into account the various possible causes of stridor, detection methods are scarce and mostly unsuccessful. There are too many variables and there is too much variation in a detection model in order to accurately predict the noise. This thesis is an attempt to create one numerical detection method, allowing to change one variable each time a simulation is run.

To make such a detection method happen, a fluid flow model is modeled using the Navier-Stokes equation. A Large Eddy Simulation is used to accurately predict the turbulence flow, together with direct wall modeling. To complete the system, a subgrid-scale (SGS) based on the selective Smagorinsky is used. This is an adapted version of the original SGS model. Therefore, an new in-house solver is implemented in OpenFOAM®, together with a new acoustic and structural solver. The acoustic solver is based on the hybrid methodology. This involves a weak-coupling procedure with the fluid flow model. Instead of using the integral solution of an acoustic analogy, the complete partial differential equation is solved. On the right hand side of this equation, the Ffowcs-Williams and Hawkings sources are used. This yields quadrupole (volume), dipole (surface) and monopole (surface) source terms. Finally, to complete the cycle, a Finite Volume linear stress analysis solver is used to solve the structural mesh. Small displacements are assumed, making a linear stress solver a valid solution. The vibrations (which are present due to the large accelerations of the structure) are used for the acoustic monopole source term. No mesh deformation is assumed, creating a complete weak-coupling mechanism between fluid, structure and acoustics. For the structural mesh, real mechanical properties of the human skin are used.

The in-house solver is validated using analytical models. For the quadrupole sources, a co-rotating vortex pair is used while for the dipole and monopole sources, the analytical integral solution of Curle and Ffowcs-Williams and Hawkings analogy is used. The overall resemblance is good, the numerical models closely match the (approximate) analytical solution. Another model, more closely related to an upper airway model, is used for validation of the fluid and acoustic domain. The so-called diaphragm involves most of the flow phenomena and is used for validating all acoustic sources. Hence, also a structural shell is created around the fluid domain. The Computational Fluid Dynamics (CFD) result for the two-dimensional case is poor, while the three-dimensional case result shows similar results as described in reference papers. The diaphragm model is also reviewed for its acoustical accuracy. The acoustic results for the dipole source term are showing the same pattern as the reference solution. However, the quadrupole sources seems to be somewhat over-predicted, while the dipole result closely match the reference line. Also the monopole source term is effective in the diaphragm model. This source is simulated twice with varying tissue properties. The result shows a clear difference between soft and firm tissue modeling, with large and small pressure perturbations respectively.

Before a real upper airway model can be modeled, the in-house solver needs to be validated using a simplified upper airway model (SUAM). This model is a simplified derivation of a original upper airway model, showing approximately the same flow characteristics as in a real upper airway. Three models were used (0%, 50% and 75% constriction), to observe the difference between different constrictions. The CFD results were as expected: when increasing the constriction size the jet velocity increases, more turbulence regions are observed, larger and stronger recirculation zones appeared, the backflow velocity increased, the strength of the vorticity increased and larger pressure drops were observed. These fluid characteristics affects the noise spectrum results. Again, the Lighthill sources are the most dominant noise sources. Also, no clear peaks at specific frequencies could be found. This makes the SUAM not so good for noise prediction. Another study into the differences between the inlet and outlet signal showed that the outlet signal is much stronger than the inlet signal. This is due to the fact that the majority of the noise production takes place behind the constriction, closer to the outlet (lungs). The constriction itself also blocks the noise, leading to a lower sound pressure level (SPL). The different models were compared with respect to their inlet and outlet probe. In case of the quadrupole sources, the 50% constriction case shows the largest SPL at the inlet probe. When looking at the dipole source term results, the result is as expected. The largest SPL at the inlet is observed at the 75% case.

Finally, after validating all models, a realistic upper airway model (RUAM) is simulated. This model is a CT-scan derived upper airway model of a patient with subglottic stenosis. The model is adapted, with the help of a medical doctor, to create another "healthy" patient model. The CFD results are as expected. With respect to the noise results, the source term magnitudes for the stridorous patient model are much larger compared to the healthy patient model. The quadrupole and dipole sources are each showing different peaks and the outlet results are much higher than the inlet results. Also, the inlet probes per model are compared. The result is as expected: the stridorous model has the most dominated sources for both the quadrupole and the dipole term. Also good resemblance is found with patient acoustic data results. The same peak in the SPL is found for a patient with a similar stridor cause. Finally, the structural mesh is verified using a soft and firm tissue model, showing similar results as with the diaphragm. The soft tissue model displays new peak, which could indicate stridor.

# Table of Contents

# List of Figures

# List of Tables

# Nomenclature

## Abbreviations

| | |
|---|---|
| BC | Boundary Condition |
| CAA | Computational Aero-Acoustic |
| CAD | Computer Aided Design |
| CFD | Computational Fluid Dynamics |
| CN | Crank Nicholson |
| CT | Computed Tomography |
| CV | Control Volumes |
| dB | Decibels |
| DES | Detached Eddy Simulation |
| DIC | Diagonal-based Incomplete Cholesky |
| DILU | Diagonal Incomplete LU |
| DNS | Direct Numerical Simulation |
| FEM | Finite Element Method |
| FV | Finite Volume |
| FVM | Finite Volume Method |
| FW-H | Ffowcs-Williams and Hawkings |
| GAMG | Generalized Geometric-Algebraic Multi-Grid |
| GUI | Graphical User Interface |
| LES | Large Eddy Simulation |
| MAE | Matched Asymptotic Expansions |
| MRI | Magnetic Resonance Imaging |
| NS | Navier-Stokes |
| PBiCG | Preconditioned Bi-Conjugate Gradient |
| PCG | Preconditioned Conjugate Gradient |
| PDE | Partial Differential Equation |
| PISO | Pressure Implicit with Splitting of Operators |
| PIV | Particle Image Velocimetry |
| RANS | Reynolds-Averaged Navier-Stokes |

| | |
|---|---|
| RUAM | Realistic Upper Airway Model |
| SGS | SubGrid-Scale |
| SI | Sound Intensity |
| SPL | Sound Pressure Level |
| SUAM | Simplified Upper Airway Model |
| TVD | Total Variation Diminishing |

## Greek Symbols

| | |
|---|---|
| $\Delta$ | Cut-off length-scale of the filter |
| $\delta_{ij}$ | Dirac delta function |
| $\epsilon$ | Strain tensor |
| $\epsilon$ | Turbulent dissipation rate |
| $\Gamma$ | Circulation intensity |
| $\lambda$ | Lamé coefficient |
| $\mu$ | Dynamic viscosity |
| $\mu$ | Lamé coefficient |
| $\nu$ | Kinematic viscosity |
| $\nu$ | Poisson's ratio |
| $\nu_t$ | Eddy, turbulent or subgrid viscosity |
| $\omega$ | Angular speed |
| $\omega$ | Specific turbulent dissipation rate |
| $\phi$ | Any tensor field |
| $\Phi(z,t)$ | Potential function |
| $\rho$ | Density |
| $\sigma$ | Stress tensor |
| $\tau$ | Viscous stress |
| $\theta$ | The angle between the vorticity vectors |

## Latin Symbols

| | |
|---|---|
| $\mathrm{J}_2(z)$ | Second-order first kind Bessel function |
| $\mathrm{Y}_2(z)$ | Second-order second kind Bessel function |
| $A$ | Surface area vector |
| $c_0$ | Wave speed propagation |
| $Co$ | Courant number |
| $E$ | Young's modulus of elasticity |
| $e$ | Total specific energy |
| $F$ | Volume flux through the face |
| $f$ | Body forces |
| $f_s$ | SGS selection function |
| $G$ | LES filter function |
| $H$ | Heaviside function |

| | |
|---|---|
| $k$ | Turbulent kinetic energy |
| $K_c$ | Cut-off wavenumber |
| $p$ | Pressure |
| $P_{ij}$ | Pressure stress tensor |
| $q$ | Energy source term |
| $R$ | Universal gas constant |
| $r$ | Distance between location and sound source |
| $Re$ | Reynolds number |
| $S$ | Strain rate tensor |
| $T$ | Temperature |
| $t$ | Time |
| $T_{ij}$ | Lighthill stress tensor |
| $u$ | Velocity |
| $u^*$ | Friction velocity at the nearest wall |
| $v$ | Surface velocity |
| $x$ | Location of the observer |
| $x$ | Structural displacement |
| $y$ | Distance to the nearest wall |
| $y$ | Location of the sound source |
| $y^+$ | Wall distance |
| $Z$ | Acoustic impedance |

## Superscripts

| | |
|---|---|
| $\bar{u}$ | Large resolved scales or mean |
| $u'$ | Smaller unresolved scales or perturbation |

# Chapter 1

# Introduction

When neonates are born too early, most of the time they are exposed to an incubator. Then, a ventilator or endotracheal tube is required for artificial respiration. This tube can create scar tissue within the upper airway, resulting in an obstruction of the airway. Some of these obstructions grow and might lead at a certain point to noisy breathing due to the turbulence properties of the air. This type of breathing is known as stridor. Stridor is a term used for defining the high-pitched, abnormal noise, resulting from turbulent airflow and vibrating tissue through a partially obstructed upper airway. This can be associated with any phase of respiration, therefore, monophasic or biphasic, inspiratory or expiratory. Any obstruction at the level of the upper airway (glottis or sub-glottis) causes inspiratory stridor. Especially with neonates stridor is a large problem, since a reduction of half the radius of the trachea due to an obstruction leads to a decrease of 75% of cross-sectional area and an increase of 16 times the airway resistance. Many papers have been written how to treat and cure patients with upper airway obstructions. Additionally, outside the medical community, the popularity of numerical computations inside a human airway tract is growing. Studies have been conducted and papers are written about numerically determining the fluid flow, obtaining the geometry from CT and MRI scans, analyzing the fluid structure interaction and obtaining the acoustics using probes. However, a numerical method combining all components is not present at this point.

In collaboration with the Otorhinolaryngology department from the Sophias Childrens Hospital, Erasmus Medical Centre in Rotterdam a proposal is set up to conduct numerical investigations into the simulation of stridor. The feasibility of Computational Fluid Dynamics (CFD) is going to be investigated to predict the noise generated by the obstruction and the propagation of the noise through the airways, taking into account the components introduced in previous paragraph. As a result, when the computations are shown to be sufficiently accurate, the inverse problem might be solved. Then, the method could be used as a tool to predict the approximate location and size of the obstruction, just by the sound produced by a patient when breathing. In the end, this prediction method might save a dangerous endoscopy, for which a neonate must be sedated.

## 1.1 Goal

Currently, no methods exists to find an obstruction in the upper airway with noise data using CFD simulations on a CT-scan derived model. Therefore, the research question and goal of this thesis is to explore to possibilities of combining current knowledge from various fields of study into a new single model to predict the noise produced by stridor. As a first step, this project will focus on the very first question: can CFD accurately simulate the flow inside the upper airway and predict the noise produced by an obstruction in the upper airway. To that end, a three-dimensional model of the trachea, obtained through a CT-scan of an actual patient is used to generate the mesh on which a CFD computation is performed. From the CFD simulation, parameters required for the acoustic simulation are investigated, such as velocity and pressure. Different acoustic analogies are proposed and compared in order to judge the modeling error of each thereby finding the most appropriate analogy for a human airway system. Firstly, only velocity volume sources (quadrupole) and pressure surface sources (dipole) are investigated. Since the upper human airway consists of soft tissue, it is also likely that vibrations will occur. Therefore, the last goal is to investigated a weak fluid-structure-acoustic coupling procedure, to determine the additional surface source (monopole), originating from accelerations at the wall.

## 1.2 Project set-up

To achieve the goal, presented in previous paragraph, this thesis is structured as follows. Firstly, a good understanding of the geometry is required. Therefore, Chapter 2 deals with the geometric properties of the human upper respiratory tract. Different sections are analyzed and a comparison between adults and children is made. Chapter 2 also includes a discussion on the phenomenon stridor, to get a better understanding of the actual problem. Different causes and different types of stridor are also discussed in Chapter 2. Chapter 3 starts with an introduction of the type of flows occuring in an upper airway system. After theses types are extracted, it is time to look into the numerical method. The governing flow equation is discussed and the type of turbulence modeling is explained. Next, in Chapter 3, also boundary conditions are discussed. The chapter is closed by an elaborated discussion on the modeling software, OpenFOAM®. The discretization, the preconditioner and iterative solver is mentioned. Next, Chapter 4 deals with the physics and the modeling of sound. After a small introduction in wave propagation, the three different acoustic analogies are discussed. The chapter is concluded by a description of the implementation of the acoustic wave equation into OpenFOAM®. Now that the physics of the fluid and sound model are explained, only the theory about the structure interaction model needs to be discussed. This is done in Chapter 5. Firstly the mathematical model of a linear elastic solid is explained, including the implementation and discretization of the governing partial differential equation. In the next section, the interface conditions and coupling procedures are extensively discussed. The following chapter verifies and validates the programmed theory of previous chapters. First, in Chapter 6, the source terms are verified. This is done using analytical expressions for the quadrupole, dipole and monopole sources, which shows a clear representation of the actual simulation. Also, the propagation of sound is validated using a diaphragm model. This model has a fully internal flow and might show behavior that is similar to what is seen in an upper airway model, since both Reynolds and jet velocity number are within the range of an upper airway tract simulation. Also for the diaphragm model, frequency spectra from literature are available. In Chapter 7 the code is tested on a Simplified Upper Airway Model (SUAM) of which numerical and experimental data for the CFD simulation is available. The model is a simplified form of a CT-scan derived model and should show flow structures that are similar to a realistic human airway model. For this model, fluid flow and acoustic properties are investigated. Finally, in Chapter 8 the code is applied on a Realistic Upper Airway Model (RUAM), which is derived from an actual CT-scan. Both a healthy person as well as a person with stridor is investigated using the proposed fluid-structure-acoustic interaction method. This thesis is concluded in Chapter 9, where a general conclusion of the proposed method is given, as well as recommendations for any further study.

# Chapter 2

# Characteristics of the human upper airway track and stridor

In this chapter, the computational domain is discussed, as well as the stridor phenomenon. The entire upper airway tract is discussed in the first section, while the next section concludes on the cause of stridor as well as a discussion on current detection methods.

## 2.1 Geometrical structure

In order to understand the particular domain of interest, discussed in the introduction, firstly the anatomy of the upper airway system is considered. The upper airway system is part of the entire respiratory system, indicated in Figure 2.1. The respiratory system is a system of an organism that performs gas exchange (oxygen and carbon dioxide) by introducing respiratory gases to the interior. This system includes the airways, lungs and respiratory muscles. The process diffusion occurs in the alveolar region of the lungs (Figure 2.1), where molecules of oxygen and carbon dioxide are passively exchanged between the gaseous external environment and the blood. Since for this numerical study, only the upper airway is considered, the following sections will contain some detailed information about the geometry of the nasal geometry, the oral geometry, the pharynx and the larynx. Stridor is addressed in next section.

### 2.1.1 Nasal cavity

An overall image of the nasal cavity is displaced on the left side in Figure 2.2. Air enters the nasal cavity from the outside through two openings, known as the nostrils or the external nares. The two openings from the nasal cavity into the pharynx are the internal nares. A

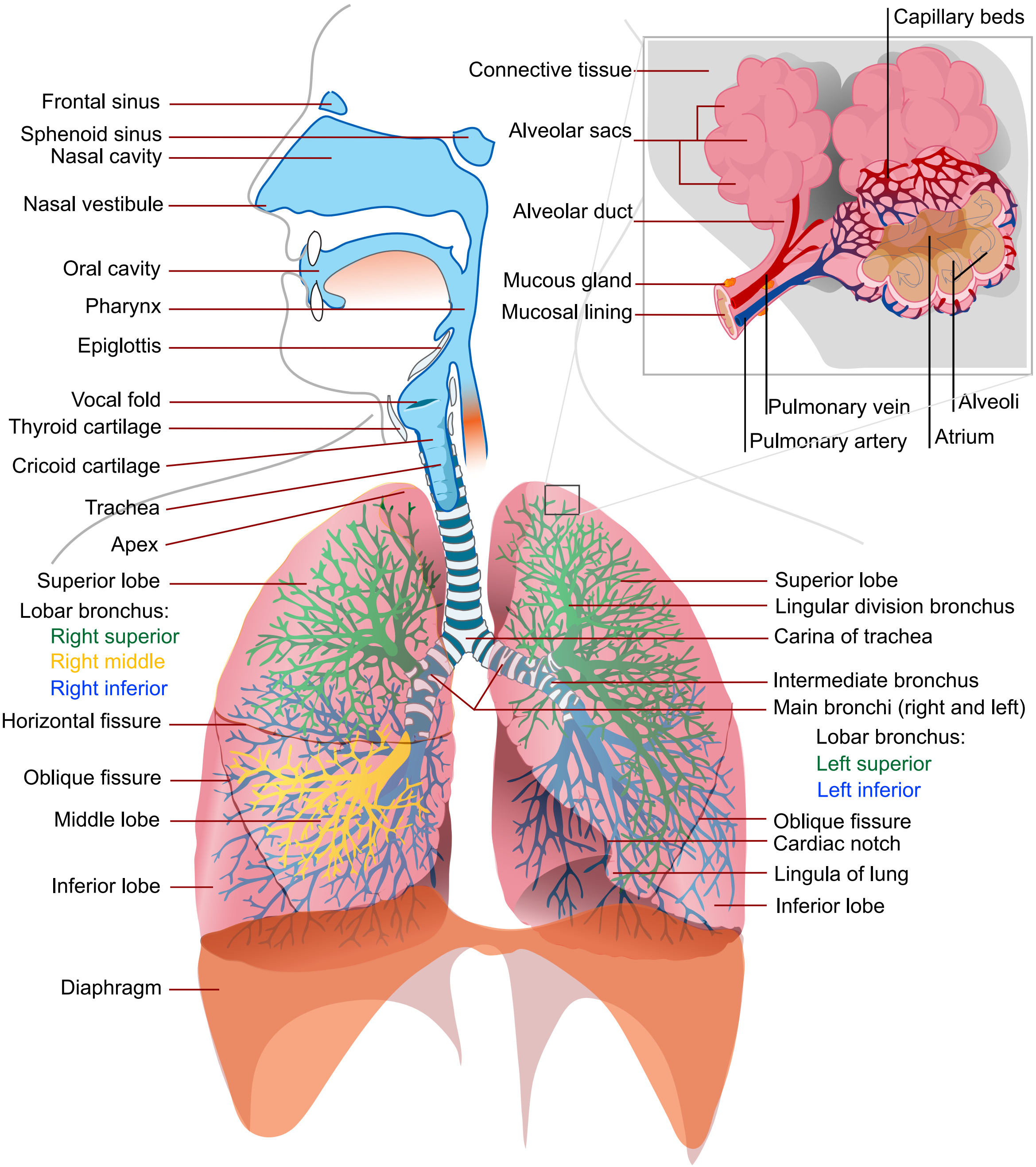

**Figure 2.1:** Overview of the entire respiratory system, Haton et al. (2009)

cross-section image of the nares is illustrated in Figure 2.2. The main flow goes through the medial passage (Figure 2.2) while flow slows down in the superior, middle and inferior meatus (Xi et al. (2011)). Also, flow has to bend 180° from the external naris to the nasopharynx (Figure 2.2). This might has great impact on the flow conditions inside the nasal cavity.

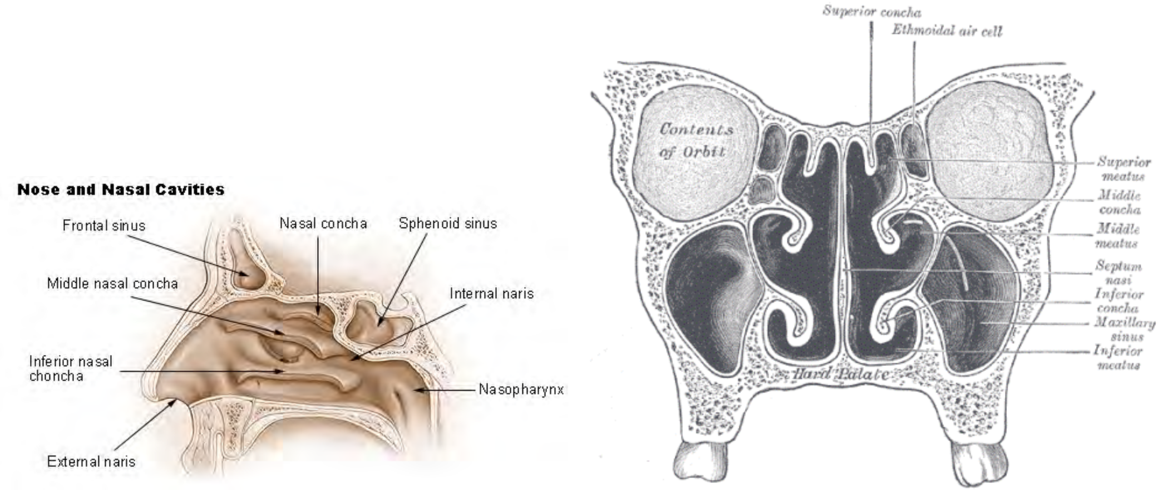

(a) Nasal cavity layout (b) Detailed slice of the external nares

**Figure 2.2:** Nasal cavity, Standring (2008)

### 2.1.2 Oral cavity

Compared with the nasal cavity, the oral cavity layout is much more straightforward. A sketch is depicted in Figure 2.3. It is the beginning of the digestive system. However it has also a significant role in communication. The primary aspects of the voice are produced in the throat. However, the jaw, the tongue and the lips could also be used to produce different ranges of sounds. Every small change of geometry can lead to a totally different sound production.

### 2.1.3 Pharynx

The pharynx is the part of the throat situated behind the mouth and nasal cavity, and before the esophagus and larynx. One can divide the pharynx into three sub-parts: the nasopharynx, the oropharynx and the laryngopharynx, (Standring (2008)). A detailed view is attached in Figure 2.3. The pharynx is part of the digestive system, but also part of the respiratory system. Therefore a primary aspect of the pharynx is the vocalization. The nasopharynx is the upper part of the pharynx. It extends from the base of the skull to the upper surface of the soft palate. The oropharynx is positioned behind the oral cavity, extending from the uvula to the level of the horseshoe shaped bone (known as the hyoid bone). Finally, the laryngopharynx is the lowest part of the pharynx; it is the part of the throat that lies inferior to the epiglottis and extends to the location where the pharynx diverges into the respiratory and digestive track.

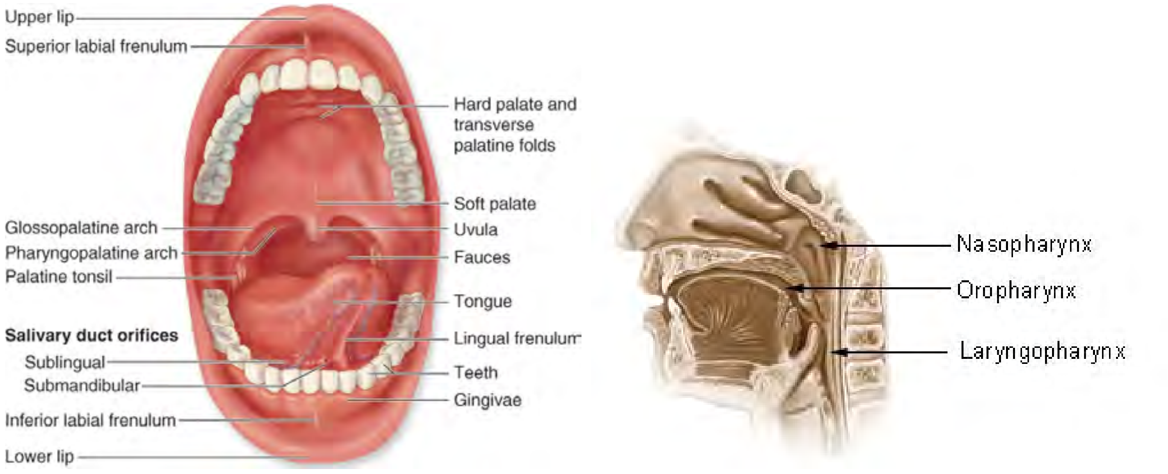

(a) Oral cavity (b) Pharynx

**Figure 2.3:** Two parts of the human airwayOral cavity, Standring (2008)

### 2.1.4 Larynx

The larynx is involved in breathing, sound production and protecting the trachea against food aspiration (epiglottis). It houses the vocal folds, which is used for phonation and the manipulation of pitch and volume. The vocal folds are positioned just below the split of the pharynx with the trachea and esophagus. The upper part of the larynx is connected to the epiglottis. The function of the epiglottis is to prevent food from going into the trachea. Details of the layout are presented in Figure 2.4.

### 2.1.5 Lower respiratory tract

The lower part of the larynx is connected to the trachea (Figure 2.4). The trachea is part of the lower respiratory tract and connects with the lungs. The trachea has C-shaped rings to keep its shape. It bifurcates into the primary bronchi at the fourth thoracic spinal nerve. Bronchi keep splitting up until finally the alveoli are reached. These are also depicted in Figure 2.1.

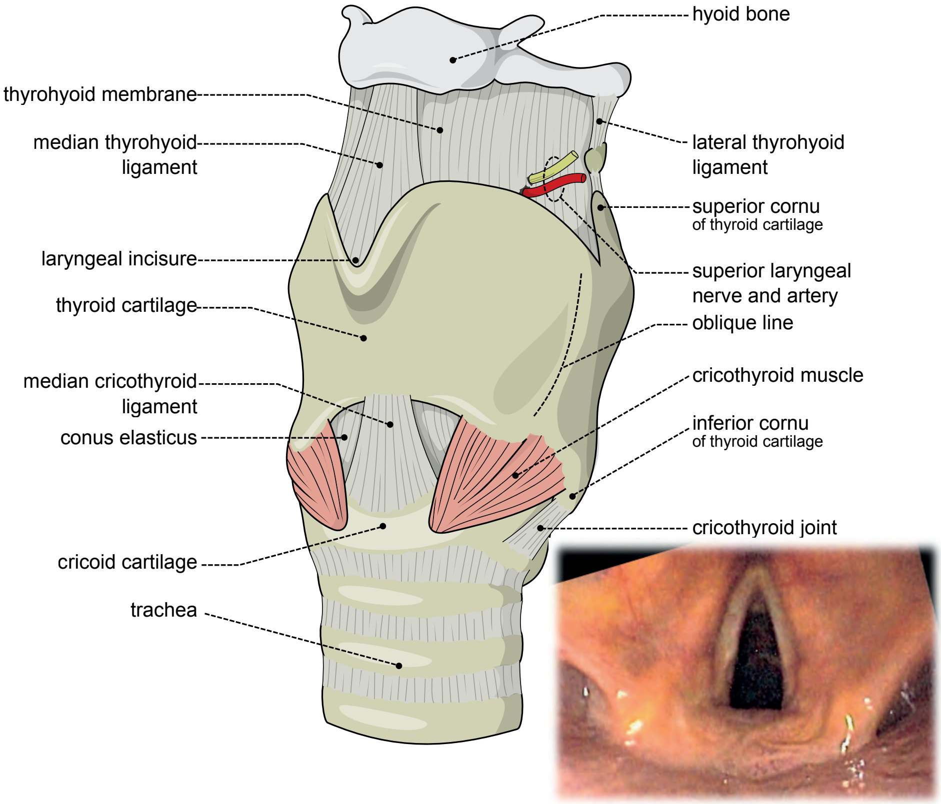

**Figure 2.4:** Larynx lay-out and endoscopic image, Standring (2008)

### 2.1.6 Geometrical differences between adults and children

As shortly discussed in the introduction, stridor is a real problem with neonates. Up until now, the anatomy discussed was based on adults. Also the simulations of airway sections, which will be discussed in further chapters, are mostly based on an adults geometry. Therefore, it is important to track any geometrical changes between adults and infants. Xi et al. (2011) performed a research in the simulation of airflow and aerosol deposition in the nasal cavity of a 5-year-old child. For this research, he compared child-adult differences in the nasal airways. The differences were quite obvious in both morphology and dimensions. Compared to an adult, a child airway has smaller sized nostrils, shorter turbinate region, a slender nasopharynx, thinner pharynx and a thinner larynx.

Cotton and Reilly (1996) also studied the differences in geometry between an adult and a pediatric airway. In a neonate, the larynx is placed high in the neck. The tip of the epiglottis is at the level of the atlas. Due to the close apposition of the epiglottis to the soft palate, nasal breathing for neonates is obligatory. Newborns also have a short epiglottis. As the larynx grows, the epiglottis increases in length even faster. The growth of the rest of the larynx is proportional. In a newborn, the narrowest area (which is about 4 a 5 mm) of the airway is at the sub-glottis, (Majumdar (2006)). To verify, a quantitative analysis is performed, indicated in Figure 2.5 and Table 2.1, from Xi et al. (2011). Results are mentioned in the plot.

**Table 2.1:** Nasal airway dimension of a 5-year-old boy and a 53-year-old male, Xi et al. (2011)

| **Anatomical sections**[a] | **Volume, *V* (cm$^3$)** | | **Surface area, *A* (cm$^2$)** | | **Effective diameter, $d_e$**[b] **(cm)** | |
|---|---|---|---|---|---|---|
| | 5-year-old | Adult | 5-year-old | Adult | 5-year-old | Adult |
| V&V | 3.37 | 5.50 | 23.74 | 35.58 | 0.568 | 0.619 |
| TR | 11.03 | 12.63 | 107.34 | 112.59 | 0.411 | 0.449 |
| NP | 3.95 | 16.33 | 15.27 | 40.93 | 1.034 | 1.595 |
| Pharynx | 2.64 | 13.89 | 14.59 | 45.10 | 0.724 | 1.232 |
| Larynx | 1.22 | 6.70 | 7.20 | 21.81 | 0.676 | 1.228 |
| Total | 22.21 | 55.05 | 168.14 | 256.01 | 0.528 | 0.860 |

[a] V&V (vestibule and valve region), TR (turbinate region), NP (nasopharynx).
[b] Effective diameter $d_e$=4 V/A.

### 2.1.7 Computational model

This section deals with the conversion of the original geometry, described in previous section, to a computational model. Firstly, an accurate patient derived model is presented. Next approximate models from different literature are shortly elaborated.

#### Patient derived model

The domain of interest is presented in previous section. In case of modeling the upper airway, a close resemblance of the reality is wanted. Therefore, Computer Aided Design (CAD) models should be obtained from imaging methods from a real patient. Possibilities

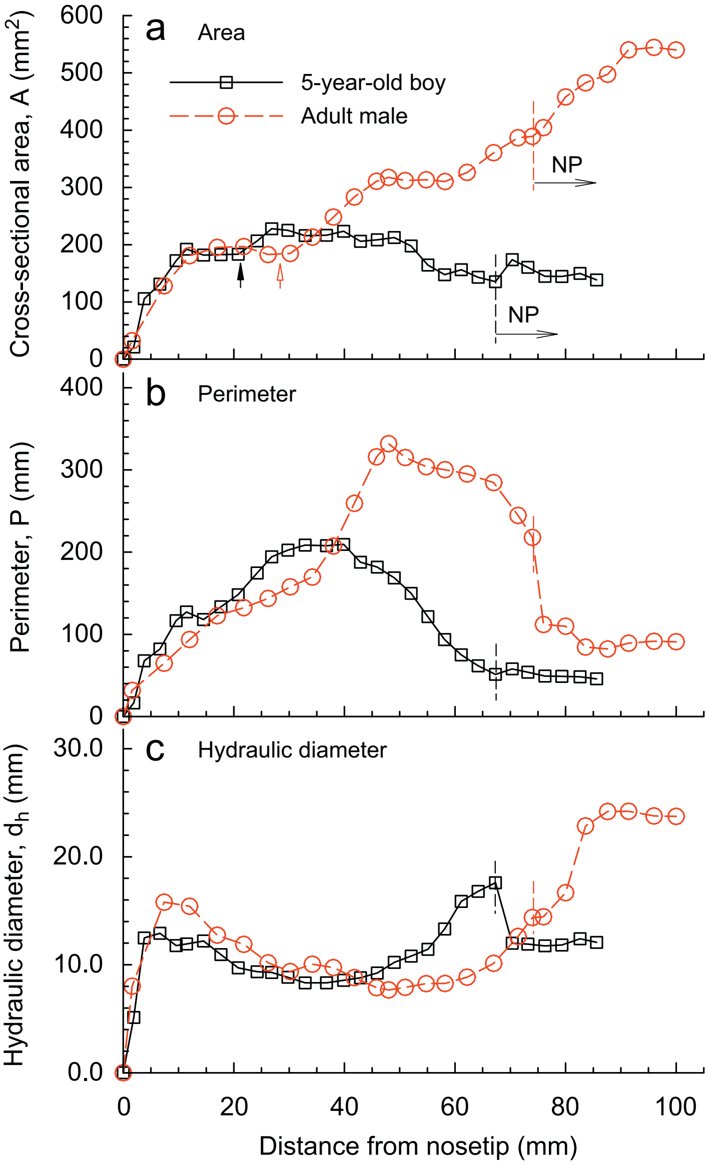

**Figure 2.5:** Comparison of nasal-cross-sectional area, perimeter and hydraulic diameter between a 5-year-old boy and a 53-year-old male as function from the nose tip. The nasal valve is marked with a solid arrow for the child and a hollow arrow for the adult. The vertical dashed line denotes the start of the nasopharynx (NP). The area and perimeter are a summation of the right and left passages, Xi et al. (2011)

here are for example Magnetic Resonance Imaging (MRI) and Computed Tomography (CT). Segmentation of the column of air behind the tongue, from the nasopharyngeal region down to the pharyngeal area results in a model for the upper airway. For a graphical illustration, Figure 2.6 (de Backer et al. (2008b)).

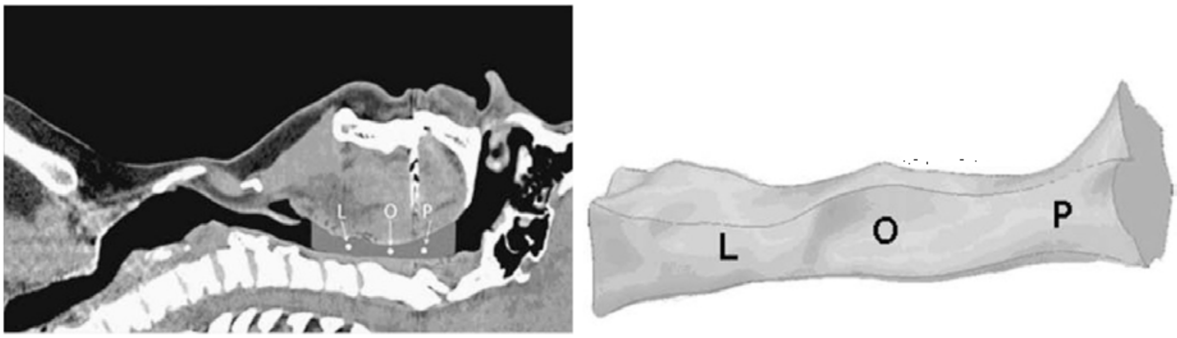

**Figure 2.6:** Three-dimensional reconstructions of the upper airway from a CT scan. L indicates the larynx, O the oropharynx and p the palatopharynx, de Backer et al. (2008b)

Various literature studies show that both CT and MRI scans have advantages and disadvantages. Some arguments are collected in Table 2.2. The largest advantages of using MRI is the principle of work compared with CT. Avoiding any radiation is crucial. To reconstruct the geometry, it is essential that any changes due to inhaling or exhaling are collected. Also, the scan should be applied on neonates, where the stridor problem also can occur. Therefore, it is essential to have short examination time to avoid any sedation. Since the examination of CT is only a few seconds, it is a practical tool for obtaining the geometry of a patient suffering from stridor.

**Table 2.2:** Comparison between CT and MRI scans

| Description | CT | MRI |
|---|---|---|
| **Principle** | X-ray attenuation | Magnetic field |
| **Examination time** | Short | Long |

After specifying the domain, a computational grid must be constructed for solving the flow equations. This boils down to subdividing the CAD model into a large number of discrete elements. Every cell is then used to calculate the local velocity, pressure and density. By using a finer grid, the result is more accurate but at the same time it increases the computational cost for the simulation. Hence, a trade-off must be made. From literature, a typical computational grid of the upper airway regions consists of 500,000 to 1,600,000 cells (de Backer et al. (2008a), Brouns et al. (2007), Jeong et al. (2007), Sung et al. (2006), Xu et al. (2006)). However, using a priori knowledge of the basic flow behaviour inside the upper airway, the amount cells can be reduced even further, while keeping the same accuracy. Since, high gradient regions require a finer grid compared to low gradient regions (Anderson (1995)). Hence, at this point, a grid choice cannot be made.

### Approximate model

In order to validate a numerical scheme used to simulate a realistic upper airway, it is interesting to run a simulation on an approximate model first. First of all, this can result in a dramatically decrease of computational time. Next, it allows one to compare results with experiments, thereby providing insight in the accuracy of the physical model (validation) and the accuracy of the numerical model (verification) with respect to the required grid. This will also be done on simplified and real geometry of an upper airway tract. In addition, a rigorous analysis of different types of acoustic sources will be tested for different types of obstructions and boundary conditions.

Many approximate models of the upper respiratory tract are available in literature. This section describes only some of them, used by Lynch (2012) in his MSc thesis. Lynch (2012) initially analyzed the acoustics of a diaphragm. The diaphragm is a fully internal flow model and shows flow behavior which is similar as in an upper airway model (turbulent flow and Coandă effect). For both geometries, experimental and numerical data was available for similar velocities as present in a real human airway, presented in Bailly et al. (1996), Gloerfelt and Lafon (2007) and Miyamoto et al. (2010). Results can be found in chapter 6.

Lynch (2012) tested a Simplified Upper Airway Model (SUAM) as a first step towards a real CT scan derived geometry. This model is an idealized model, derived from real airway geometries and shows the same type of flow structures that are encountered in a real airway. This SUAM, illustrated in Figure 2.7, is discussed in the paper by Jayaraju et al. (2008), where a Large Eddy and Detached Eddy Simulation (LES and DES) analysis is performed. Also experimental reference data is available, from a Particle Image Velocimetry (PIV) measurement by Brouns et al. (2006). The SUAM model can also be used to investigate the effects of the constriction size and the corresponding acoustic behavior. Lynch (2012) used multiple versions, with (50 % and 75 %) constriction and without constriction, for comparison. These models are re-used in this analysis, in combination with a newly proposed acoustic analogy. Results are presented in chapter 7. Next to the SUAM, Lynch (2012) tested a realistic CT scan derived upper airway model (RUAM). Two versions were created. One directly derived from a CT-scan of a patient suffering from a subglottic stenosis, performed by Wim Vos at FluidDA, and an adapted version by Lynch (2012) to represent a healthy person. An illustration of both models is presented in Figure 2.8. In this thesis, the same model is used to test the acoustics. Results are written down in chapter 8.

More models are presented in various literature papers. Examples of realistic models, derived from CT and MRI scans can be found in the following literature: de Backer et al. (2008b), Mylavarapu et al. (2009), Wang et al. (2012). Mostly, idealized or approximate models of the upper airway are used, such as in Heenan et al. (2003), Jayaraju et al. (2008), Luo et al. (2004), Mihaescu et al. (2008), Stapleton et al. (2000) and Zhang et al. (2002). All these papers are concerning a model for the upper airway. However, also for the lower respiratory system, for example the airway bifurcation model, models exist (Calay et al. (2001), Farkas and Balásházy (2007), Luo and Liu (2008), Luo et al. (2004), Xia et al. (2010)). The information from these papers is used to better interpret the results from this thesis.

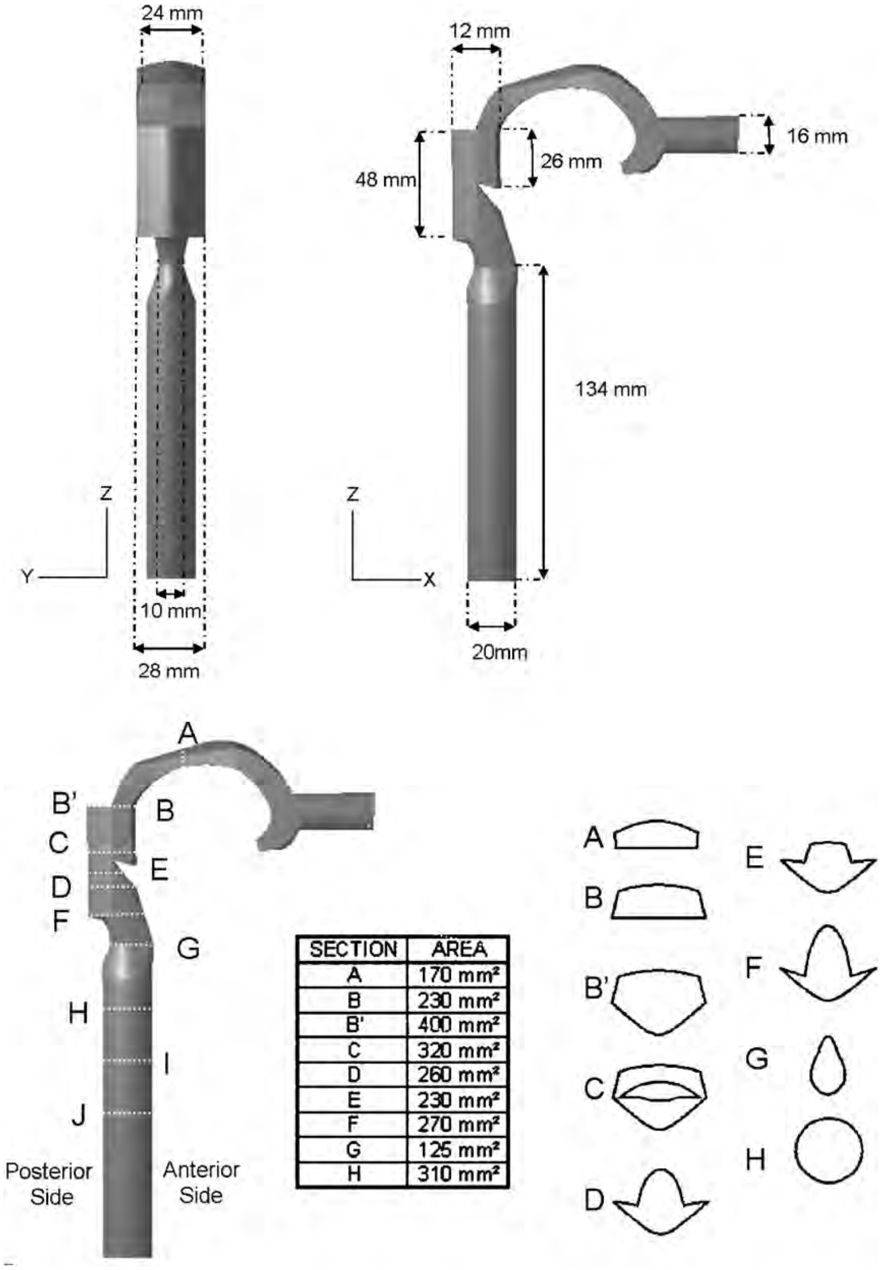

| SECTION | AREA |
|---|---|
| A | 170 mm² |
| B | 230 mm² |
| B' | 400 mm² |
| C | 320 mm² |
| D | 260 mm² |
| E | 230 mm² |
| F | 270 mm² |
| G | 125 mm² |
| H | 310 mm² |

**Figure 2.7:** Simplified upper airway model (SUAM), Jayaraju et al. (2008)

**Figure 2.8:** Realistic CT-scan derived upper airway model. The original with obstruction is presented left, while the adapted (healthy person) is depicted on the right, Lynch (2012)

## 2.2 Stridor

Stridor is a term used for defining the high-pitched, abnormal noise, resulting from turbulent airflow and vibrating tissue through a partially obstructed upper airway. This can be associated with any phase of respiration, therefore, monophasic or biphasic, inspiratory or expiratory. Any obstruction at the level of the upper airway (glottis or sub glottis) causes inspiratory stridor. Expiratory stridor indicates lower airway tract obstruction (Hirschberg (1980), Majumdar (2006), Slawinsky and Jamieson (1990)). Supraglottic obstruction will usually cause stridor or more commonly stertor, a low-pitched snoring type of noise. And an obstruction of the extra-thoracic trachea tends to cause biphasic stridor while obstruction of the intra-thoracic trachea usually causes expiratory stridor (Hirschberg (1980)).

When an adult or infant shows signs of stridor, immediate attention is required. After diagnosing stridor in a child, the primary task is to assess and secure the airway. There are basically two physical principals that are crucial for patients with stridor. First of all, linear flow of air in a tube produces forward pressure but reduces the lateral pressure. If one assumes a flexible airway, this linear flow might lead to a collapse of the upper airway wall. Another principle originates from the fact that the resistance of the airway is inversely proportional to the fourth power of the radius of the airway. So, if a neonate has a reduction of half the radius of the trachea, an increase of 16 times the airway resistance is encountered. Overall, this leads to a decrease of 75 % of the cross-sectional area (Claes et al. (2005), Majumdar (2006)).

### 2.2.1 Causes

There are many possible causes for stridor. The following paragraphs will give a short explanation of the most common causes of stridor for children.

#### Laryngotracheobronchitis

Laryngotracheobronchitis, also known as croup is the most common cause of acute stridor in children under the age of 2 years (Klassen (1999)). It is a respiratory condition that usually is triggered by an acute viral infection (think about parainfluenza virus) of the upper airway. The infection leads to a swelling inside the throat, which will interfere with normal breathing, which causes stridor.

#### Epiglottitis

Another aethiology, which produces stridor, is epiglottitis. This is a bacterial infection of the epiglottis most commonly caused by a certain type of influenza. The condition usually occurs in children between 2 and 6 years old. Here also swelling of the airway occurs (Majumdar (2006)).

### Retropharyngeal abscess

Another possible cause is a retropharyngeal abscess. This is a rare but extremely dangerous condition with a high mortality (Lalakea and Messner (1999)). It is an abscess located in the tissues in the back of the throat behind the posterior pharyngeal wall. Because the abscess typically occurs in deep tissue, it is very difficult to diagnose by physical examination. It can lead to airway obstruction, including a stridorous sound.

### Foreign bodies

A more uncommon but important cause of stridor in pre-school children is foreign bodies (like toys or food). If high in the airway an inhaled foreign body is present, stridor may occur. Impacted pharyngeal or oesophageal foreign bodies may cause stridor by airway compression. A example of a foreign body inside the trachea is depicted in Figure 2.9, from Majumdar (2006).

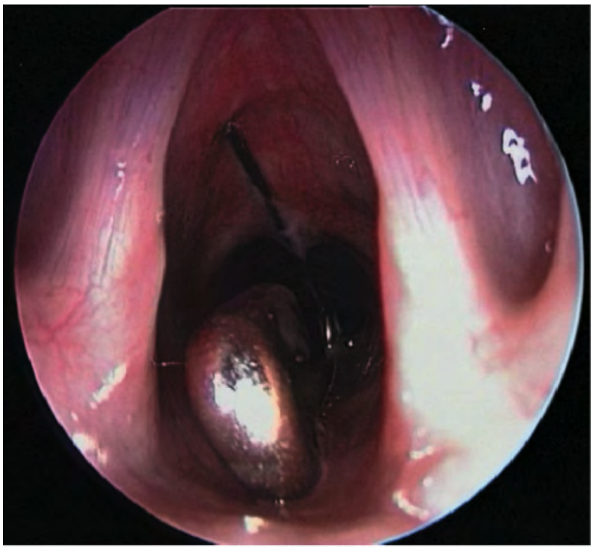

**Figure 2.9:** Foreign body in the sub-glottis, Majumdar (2006)

### Laryngomalacia

The most common case of congenital stridor is laryngomalacia. It appears usually shortly after birth and it resolves by the time the child is 12-18 months. This type of stridor is characteristically inspiratory and squeaky and a literally translation of soft larynx. The soft immature cartilage of the upper larynx collapse inward during inhalation, causing airway obstruction. This cause is clearly presented in Figure 2.10. It is also commonly associated with feeding problems and a failure to thrive (Majumdar (2006)).

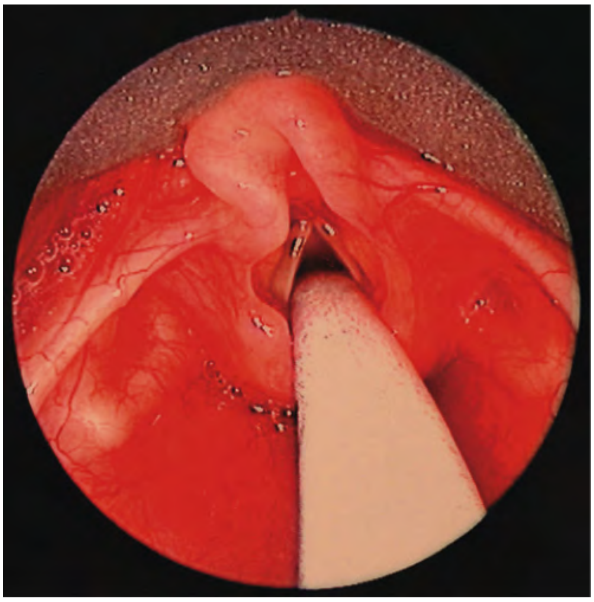

**Figure 2.10:** Laryngomalacia, showing "omega" shaped epiglottis and short folds, Majumdar (2006)

### Vocal cord paralysis

Vocal cord paralysis is the second most common airway problem (after laryngomalacia). It is a common cause with newborns and indicates the weakness of one or both vocal folds. It is associated with a weak cry and hoarseness. The stridor is often biphasic and louder when the child is awake (Majumdar (2006)).

### Laryngeal papillomatosis

Laryngeal papillomatosis, indicated in Figure 2.11, is caused by the human papilloma virus. It is a rare medical condition; only 3-5 people out of 100.000 will suffer from this disease (Majumdar (2006)). It causes tumors or papillomas in the throat. Without any treatment, it is potentially fatal since it can obstruct the entire airway.

### Subglottic stenosis

Subglottic stenosis is a very common cause with neonates. It may be congenital or acquired narrowing of the subglottic airway. It may cause respiratory stridor and is the third most common congenital airway problem (after laryngomalacia and vocal cord paralysis). Prolonged placement of endotracheal tubes in premature babies is the most common cause of acquired stenosis, Majumdar (2006). The luminal diameter may be less than 3 mm in pre-term babies. A four-grade scale is developed for stenosis that indicates the severity of the situation. Grade 1 indicates an obstruction of 50 % or less, grade 2 51-70 % obstruction, grade 3 71-99 % obstruction and grade 4 indicated that no lumen can be detected. For an illustration, an airway endoscopy of an upper airway with a subglottic stenosis is presented in Figure 2.12.

**Figure 2.11:** Laryngeal papilloma, Majumdar (2006)

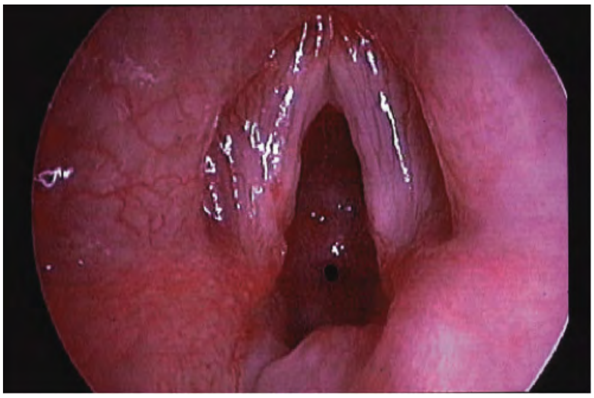

**Figure 2.12:** Subglottic stenosis, Majumdar (2006)

Another form is the tracheal stenosis. It may result from congenitally complete tracheal rings and can vary from relatively minor narrowing to a congenital micro-trachea. Hence, some cases of tracheal stenosis will lead to the death.

#### Tracheomalacia

Tracheomalacia is the name for lack of cartilaginous support of the trachea. This causes the trachea to collapse of its lumen with a resultant stridor. In normal condition, the trachea dilates slightly during inspiration and narrows slightly during expiration. Hence, in the case of tracheomalacia, these above described processes are exaggerated, leading to airway collapse. This might lead to expiratory stridor (Majumdar (2006)).

### 2.2.2 Current detection methods

Detecting the location of an obstruction in the upper airway is a topic that is widely studied by doctors and engineers. In this section, some of the research is mentioned and summarized.

Zwartenkot et al. (2010) established a research to determine the inter-observer reliability in localization of recorder stridor sounds in children. The stridor was recorded via a high quality digital recorder. The participants were asked to score the sounds. Valid choices were: pharyngeal, supraglottic, glottis, subglottic and tracheal. The scores were analyzed per group of participant, per location of obstruction and per diagnosis. The result was that supraglottic sounds were significantly better differentiated from the other locations. However overall result shows poor level of localization (i.e. overall score of 30 %).

Zwartenkot also investigated stridor via spectrograms in Zwartenkot (2010). Different causes of stridor and different locations were investigated. Overall result was also poor; it was difficult to find a correlation between the diagram (example attached in Figure 2.13), location and cause.

Verbanck et al. (2010) tried to detect an upper airway obstruction in patients with tracheal stenosis. They used a so-called forced oscillation test modality for detecting upper airway obstruction as an alternative to a spirometric upper airway obstruction test. From oscillometry performed at different breathing flow rates, the airway resistance was determined and the flow dependence of resistance was computed. They conclude that the tests at different breathing flow rates are useful to provide a measure of the upper airway obstruction (flow dependence of resistance), which can indicate a critical level of stenosis.

Another frequency dependent research was carried out by Modrykamien et al. (2009). Here the frequency of detecting upper-airway obstruction is measured via a quantitative and visual assessment of flow-volume loops. They measured the ratio of forced expiratory volume and the ratio of the flow at the mid-point of the forced expiratory versus inspiratory maneuver. The visual assessment was based on criteria such as: the presence of a plateau, biphasic shape and oscillations. The results of the quantitative criteria were better compared with the qualitative criteria. However, still a low sensitivity was obtained.

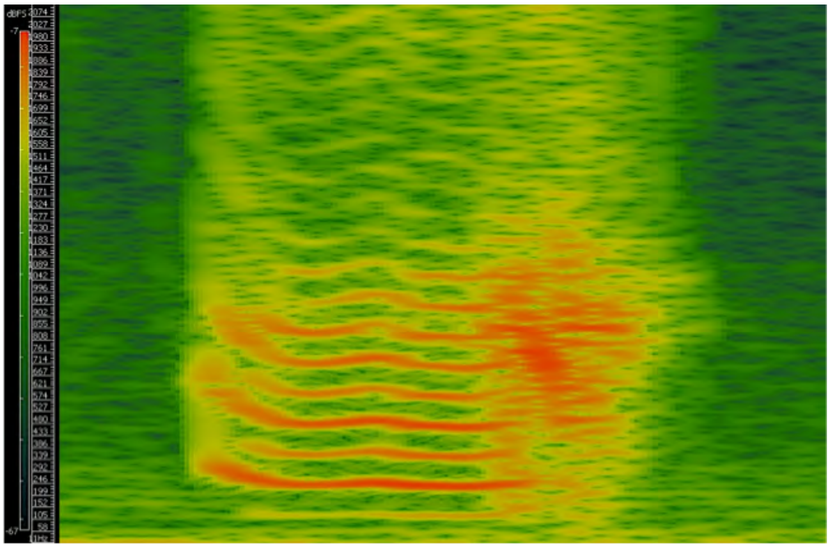

**Figure 2.13:** Spectrogram of child suffering from laryngomalacia, Zwartenkot (2010)

Slawinsky and Jamieson (1990) performed an in-depth research into the acoustical analyzes and tests of respiratory stridor. Multiple physical characteristics from acoustical analysis were found, from which it should be able to specify stridor. For the sake of completeness, the most important conclusions extracted from Slawinsky and Jamieson (1990) are repeated below:

- *The location of constriction*: constrictions placed close to the nostrils emphasize higher frequencies and maintain similar values of murmur duration and intensity in both respiration cycles. Constrictions close to the bifurcation increase the amplitude of lower frequencies and prolong the expiration cycle.

- *The mass and elasticity of the tissue surrounding the constriction*: large mass and low elasticity tend to result in a fricative source, reflected in the murmur as a noise with formants corresponding to natural frequencies of the respiratory tract. Smaller mass and higher elasticity tend to result in a voiced source, which appears in the murmur as a tone.

- *The shape of the constriction*: long constrictions tend to generate fricative sources, while short constrictions tend to generate voiced sources (if the pressure drop is sufficiently large).

- *The cross-sectional area of the construction (for fricative sources)*: lower frequencies dominate the signal spectrum when the airway is relatively large, while higher frequencies emerge as the airway narrows.

- *The tissue tension (for voiced sources)*: high tension gives a high-frequency tonal quality to the murmur, while lower tension shifts the fundamental frequency (pitch) of the murmur to lower values.

- *The mobility of the constriction*: with stable constrictions, resistance to airflow is equivalent in both cycles of respiration and stridor is produced in both cycles. Unstable constrictions produce changes in the spectrum from one cycle to the next and within each cycle.

- *The ratio of the duration of the constriction opening to the period of tissue vibration (for voiced sources)*: a small value of ratio (much lower than 1) is reflected in the spectrum of a murmur by many harmonics of fundamental frequency, while an appearance of only a few harmonics indicates that a constriction lumen is open much longer.

Other researches, which are worthwhile mentioning, are the studies of Leiberman et al. (1986) and Milenkovic (1984). Leiberman et al. (1986) analyzed computerized digital stridor and snoring sounds from 5 children. For this, the upper airway tract was assumed to be an acoustic tube with varying cross-sectional areas, starting from the glottis, and ending at the lips and nose. The tube was arbitrarily divided into sections each with equal lengths, but different cross-sections. The tube was assumed to be rigid and discretized sufficiently well. Using these assumptions, it was possible to directly find the cross sectional areas from the acoustical signal/stridorous sound. The result showed a consistent acoustical pattern, but further acoustic analyses are needed to standardize this method.

Milenkovic (1984) described a formulation to determine the cross-sectional areas of the vocal tract by using the pressure spectrum. The pressure spectrum is the magnitude squared of the transfer function relating acoustic pressure at the glottis to pressure measures in the acoustic radiation beyond the lips. Hence, a two point system was used. Milenkovic (1984) was able to reproduce area functions using the measurement data of speech. The algorithm is effective for a vocal tract with lossless walls.

# Chapter 3

# Physics and modeling of fluid flow

This chapter describes the current knowledge about fluid flow in the upper airway system. Initially, a general overview is presented about typical airflow inside the human airways. After this general introduction, the most suitable method for this particular simulation, which was selected in the literature study of van der Velden (2012), is elaborated. The governing flow equations of the model are given and the turbulence model is elaborated. Also, an introduction in the Computational Fluid Dynamics (CFD) software OpenFOAM®is given. Finally, the discretization methods and boundary conditions will be treated.

## 3.1 Brief overview

Based on an overall view of the geometry, typical airflow conditions in the upper airway can be deduced. Since the human airways are complex in shape (even in the case of children), a complex flow regime exists. Inspiration is usually a process from the nasal cavity to the alveoli. In between these regions the flow can bend, encounters sharp edges, cavities and ducts. The flow can take many forms and different phenomena could occur, such as flow separation and flow re-attachment, laminar, transitional and turbulent flow.

With this in mind, it is worthwhile asking whether the flow in the entire upper respiratory tract is in fact turbulent (Finlay et al. (1996)). This issue has been raised by different authors, such as Ahmed and Giddens (1983), Dekker (1961) and Olsen et al. (1973), but it is worthwhile mentioning again here. The geometry of the upper airway system is basically a series of bifurcating tubes. Using White (1994) a first estimate of Reynolds number $Re = 2300$ is given to deduce the flow pattern inside the model. However this value has no meaning, since it is a very rough estimate based on experiments in smooth walls, straight pipes, far from any inlet (hence the flow is fully developed). So it can easily vary between 1800 and $10,000$ due to the complex geometry and different flow characteristics (Finlay et al. (1996)). Detailed studies are performed to determine specific flow rate values and corresponding Reynolds numbers (based on the normal distance to the nearest wall) for an upper respiratory system of a child and an adult. These values are presented in Table 3.1 (Jeong et al. (2007) and Xi et al. (2011)).

**Table 3.1:** Normal flow rates and Reynolds numbers for an adult's and childs upper respiratory system, Jeong et al. (2007) and Xi et al. (2011)

| | **Normal flow rates [L/s]** | | **Reynolds number [-]** | |
|---|---|---|---|---|
| | *Light breathing* | *Heavy breathing* | *Light breathing* | *Heavy breathing* |
| **Adult** | 0.2 | 1.67 | 800 | 9300 |
| **Child** | 0.05 | 0.5 | 368 | 3302 |

According to Finlay et al. (1996), from a fluid dynamics point of view, the flow near the nose, teeth, mouth, pharynx and larynx shows little resemblance to fully developed pipe flow, since:

- The flow is near the entrance, thereby impossible to fully develop,
- There are separated regions, where the flow recirculates,
- There are free shear layers, where away from any walls, adjacent regions of fluid move at considerably different velocities.
- There is a mean streamline curvature.

The turbulence associated with the last three flow features, tends to develop at lower Reynolds numbers, compared with the turbulence in a straight pipe.

The transition from laminar to turbulent in the human trachea was already a field of discussion in 1961. Dekker (1961) investigated the critical velocities at which turbulence appears using 21 plastic casts of the human trachea. The flow patterns were very different for each individual cast. For a regular inflow, turbulent flow appeared. This is visualized in Figure 3.1. Only for quiet breathing, with flow rates around 125 - 200 ml/s and a breathing frequency of 0.25 Hz (which are 15 cycles per minute) a Strouhal number of 0.2 in the nasal cavity is found. The Strouhal number is defined as $St = \frac{\omega L}{U}$, with the length-scale $L$ based on the axial length from the entrance. According to Keyhani et al. (1995), this indicates that a quasi-steady approximation is valid. Olsen et al. (1973) also verified this statement by an experiment. He found out that a steady flow assumption is valid for flow rates up to 2.5 L/s. When a peak velocity is reached, the flow seems to be comparable with a quasi-steady flow. But, during acceleration and deceleration different velocity profiles are encountered (Calay et al. (2001)).

Another research into the flow field is carried out by Ahmed and Giddens (1983). They studied the result of steady flow through an axisymmetric stenosis (25, 50 and 75 % area reduction) at different Re numbers (in a range from 500 to 2000). The so-called Coandă effect was captured (wall attachment away from the obstruction). These experimental results are later frequently used for comparison with numerical methods (for example in Luo et al. (2004) and Zhang et al. (2002)).

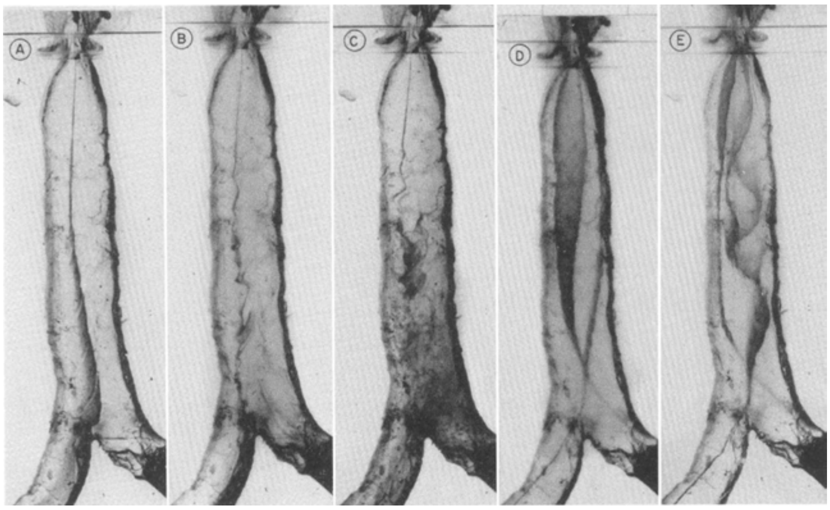

**Figure 3.1:** Traces of dye in a plastic cast of the human trachea, perfused with water at different speeds. A, B and C: inspiratory flow equivalent to, respectively, 28, 72 and 116 ml/air/sec; D and E: expiratory flow equivalent to, respectively, 54 and 95 ml/air/sec. A:laminar flow; B: beginning turbulence; C: well-developed turbulence; D: laminar flow in expiratory direction; E: spiral pattern of expiratory flow, beginning of turbulence, Dekker (1961)

Thus, based on previous research and as suggested by previous authors, the flow in the nose, mouth and throat is probably not laminar (except at quite low inhalation rates).

## 3.2 Governing flow equation

The goal of this thesis research is to investigate the noise from turbulent structures, originating from an obstruction in the human upper airway tract. Since these flows are typically in the very low Mach regime, and subjected to Newtonian fluid properties, the Navier-Stokes equations can be used as the governing equations describing the fluid dynamics of the specific domain. The Navier-Stokes equations are a collection of five equations. The first Equation (3.1a) describes the conservation of mass, the second Equation (3.1b) the conservation of momentum (three equations for the $x$, $y$ and $z$ direction in Cartesian coordinates) and the last Equation (3.1c) formulates the conservation of energy.

$$\frac{D\rho}{Dt} = \frac{\partial\rho}{\partial t} + \nabla\cdot\rho\mathbf{u} = 0, \tag{3.1a}$$

$$\frac{D\rho\mathbf{u}}{Dt} = \frac{\partial\rho\mathbf{u}}{\partial t} + \nabla\cdot(\rho\mathbf{u}\mathbf{u}) = -\nabla p + \nabla\cdot(\mu\nabla\mathbf{u}) + \mathbf{f}, \tag{3.1b}$$

$$\frac{D\rho e}{Dt} = \frac{\partial\rho e}{\partial t} + \nabla\cdot(\rho\mathbf{u}e) = -\nabla p\mathbf{u} + \nabla\cdot(\mu\mathbf{u}\nabla\mathbf{u}) - \nabla q, \tag{3.1c}$$

wherein $D/Dt = \partial/\partial t + \mathbf{u}\nabla$ indicates the material derivative. Other important variables are $p$, $\rho$, $u$, $e$, $q$ and $f$, also known as the pressure, density, velocity, total specific energy, energy source term and the body forces of the fluid. In addition, $\nabla$ refers to the Nabla operater, defined as:

$$\nabla = \left( \frac{\partial}{\partial x} \quad \frac{\partial}{\partial y} \quad \frac{\partial}{\partial z} \right)^{\mathsf{T}} . \tag{3.2}$$

As indicated in previous section, the flow inside the human upper airway is characterized by a low Mach number flow. Hence, the flow can be assumed to be incompressible which results in a homogenous constant density in the entire domain. To further simplify the Navier-Stokes Equations (3.1) the assumption is made that no external forces are exerted on the fluid. Hence gravity forces and other body forces are neglected. Also temperature changes are ignored, making the fluid flow equations independent of temperature. Applying these assumptions, only four different quantities remain; the different velocity components and the pressure. The Navier-Stokes equations reduce to:

$$\nabla \cdot \mathbf{u} = 0, \tag{3.3a}$$

$$\frac{\partial \mathbf{u}}{\partial t} + \nabla \cdot (\mathbf{u}\mathbf{u}) = -\frac{\nabla p}{\rho} + \nabla \cdot (\nu \nabla \mathbf{u}), \tag{3.3b}$$

wherein $\nu$ indicates the kinematic viscosity. The entire last term in Equation (3.3b) is also known as the viscous stress term, defined as $\nabla\tau$.

## 3.3 Turbulence modeling

Concerning the computation of the turbulent flows, different CFD schemes can be used. Nowadays, improvements in computational performance and a better understanding of the characteristics of turbulent flows allows one to simulate physically accurate turbulent fluid flow fields for many real applications. For this specific domain, it is therefore important to select an accurate method, since the fluid properties such as velocity and pressure are going to be the main source for conducting the acoustic computations. The physics and modeling of the acoustics is discussed in the next chapter.

Although the upper respiratory airway tract has a very specific geometry many studies have already been devoted to it. During these studies, mainly the typical airflow features and the aerosol (particle) distribution are investigated and discussed. Together with some research into the field of upper airway obstructions a large amount of papers is published. Next, there is a large amount of variation on the type of CFD scheme. So, it is always a challenge to find the best airflow model to get the most accurate solution. In general, a large influence on the type of model is the geometry. Even simplified geometries require unstructured meshes, leading to large grids. Hence, the size of the grid and the complexity of the geometry, and therefore the type of airflow, has a large influence in the type of turbulence models that can be chosen.

The first option is to compute all turbulent eddies, which are essential for the acoustic sources. This is known as Direct Numerical Simulation (DNS) of the Navier-Stokes equations. This requires a resolution on the order of the finest scales of turbulence (the Kolmogorov scale), which would require on the order of hundreds of millions of grid points required for the simulation of the upper airways (i.e. of the order $Re^{9/4}$ (Hulshoff (2011)). Unfortunately, this method is too computationally expensive for an airway model. Besides, not all turbulent scales may be relevant for a acoustic analysis.

Therefore it might be better to directly resolve the larger turbulence scales that should be important for the acoustic sources, while modeling the smaller eddies that are not significant for the acoustic sources. This is known as a Large Eddy Simulation (LES). Still, the LES method is classified as a method with a relatively high computational cost. However, with the LES method it is already possible to simulate turbulent flows with fairly low $Re$ numbers and complex geometries. This makes it a suitable method for an upper airway model Wagner et al. (2007).

The majority of the studies presented in the previous decades solve turbulence using the Reynolds-Averaged Navier-Stokes (RANS) equations. Whenever solving this type of equations, one has the option to solve the flow as if it was laminar throughout the entire domain, as performed by Huang et al. (2005). This reduces the complexity of the simulations, therefore increasing the computational speed. However, from the introduction of this chapter did follow that a laminar approach is only valid for extremely low Re numbers. Another option is to close the system of RANS equations by using a turbulence model. There are a number of options, but the two most commonly used RANS turbulence models in industry are: $k-\epsilon$ and $k-\omega$. Now turbulent flow features are modeled by solving the variables for turbulent kinetic energy ($k$) and turbulent dissipation rate ($\epsilon$) or specific turbulent dissipation rate ($\omega$). One of the advantages of the $k-\omega$ model is that there exists a low Re number model that can obtain an accurate laminar solution when the turbulent viscosity approaches zero, as mentioned by de Backer et al. (2008b). This becomes necessary when dealing with flows in transitional regions. A larger disadvantage is that due to the fact that all eddies are modeled, there is a possible loss of fluctuations which can be relevant for acoustic sources.

In this thesis, a LES model is used together with a special implemented SubGrid-Scale (SGS) model, required to close the system of equations. The following sub-sections therefore continues on the theory of the LES and the SGS model. For the interested reader, the literature study by van der Velden (2012) contains a review of all used turbulence methods inside a human upper airway tract. Here, also hybrid methods are discussed.

### 3.3.1 LES

The idea of LES originates from the early 60's and was well documented by Smagorinsky (1996). The theory is based on the theory of the Kolmogorov large scales, which contains most of the energy in a turbulent free field. The largest scales contribute most to the transport and are therefore calculated directly. The smaller scales are then modeled, with the assumption that they behave uniformly. This leads to the fact that in a turbulent energy spectrum, the smaller scales only contribute a fraction of the total energy. This can be summarized by Figure 3.2, presented in the course notes from Hulshoff (2011). The energy spectrum is roughly divided in three regions:

- The first region is the *large scale range*. The largest scales in the flow are those responsible for turbulence production, and carry out the majority of turbulent kinetic energy. This energy is extracted from the mean flow, and have comparable length and velocity scales. They have a macroscopic effect on geometry and forcing, and are therefore of primary importance in the computation of acoustics. Besides the turbulence scales, the frequency of the fluctuations can also be important to identify the correct acoustic sources.

- The second range is the *inertial subrange*. The eddies will follow Kolmogorov's law. It is a region dominated by transitive scales. Hence, energy transfer between the larger and smaller eddies takes place in this range.

- The last region is the *dissipation range*. In this range, the behavior of eddies is assumed to be dominated by the viscosity and the rate of energy transferred from the large scales. The eddies are very small, compared with large scale range and are not dependent on the larger scales.

Figure 3.2 also indicates the resolved and unresolved scales region. The separation takes places at the cut-off wavenumber $K_c$.

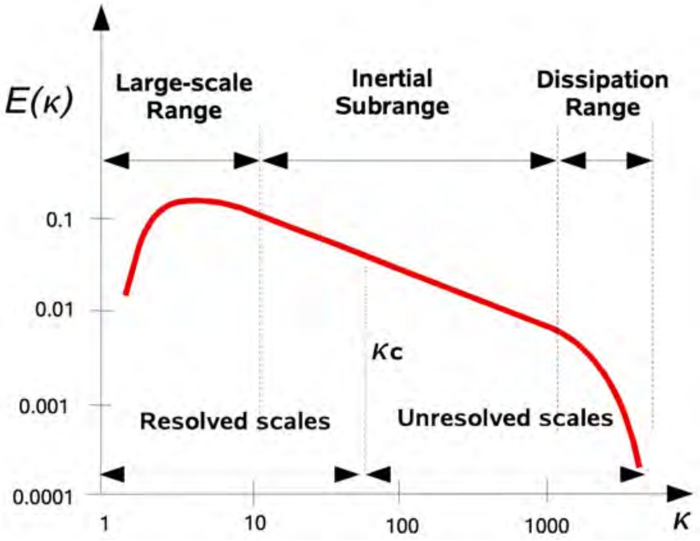

**Figure 3.2:** Resolved and unresolved scales in LES, Hulshoff (2011)

### 3.3.2 Scale separation using filtering

To separate different scales, a filter function is required. In LES, a locally derived weighted average of the flow properties over a volume of a fluid is used. Important here is the filter width $\Delta$. The turbulent scales larger than $\Delta$ are solved directly, while the scales which are smaller than $\Delta$ are modeled using a SGS model.

First, any flow variable should be rewritten in the form of a contribution of a large scale and small scale. For example, the velocity can be written as:

$$\bar{\mathbf{u}} = \mathbf{u} - \mathbf{u}', \tag{3.4}$$

wherein the over-bar refers to the larger scales, while the prime indicate a smaller scale velocity. A way to define a filtered and therefore large-scale velocity is to use convolution over the physical domain, $\Omega$:

$$\bar{\mathbf{u}} = \int_{\Omega} \mathbf{u}(x') G(x, x'; \Delta) dx', \tag{3.5}$$

where the convolution kernel should satisfy:

$$\int_{\Omega} G(x, x'; \Delta) dx' = 1. \tag{3.6}$$

The standard filter used in OpenFOAM®(an open-source CFD software package that will be described later) is the top-hat filter, defined as:

$$G(x, \Delta) = \left\{ \begin{array}{ll} \frac{1}{\Delta}, & \text{if } |x'| \leq \frac{\Delta}{2} \\ 0, & \text{otherwise} \end{array} \right. . \tag{3.7}$$

This filter is simply defined as the average over a rectangular region and often applied in finite volume methods (FVM).

### 3.3.3 The filtered Navier-Stokes equations

If a filter is applied to the incompressible Navier-Stokes equations in Equation (3.3), the fluid equation of motion can be derived only based on the larger eddy scales:

$$\frac{\partial \bar{u}_i}{\partial x_i} = 0, \tag{3.8a}$$

$$\frac{\partial \bar{u}_i}{\partial t} + \frac{\partial}{\partial x_j}(\bar{u}_i \bar{u}_j) = -\frac{1}{\rho}\frac{\partial \bar{p}}{\partial x_i} + \frac{1}{\rho}\frac{\partial \tau_{ij}^R}{\partial x_j} + \nu \nabla^2 \bar{u}_i. \tag{3.8b}$$

Reordering and making above equations non-dimensional, results in the following set of equations:

$$\frac{\partial \bar{u}_i}{\partial x_i} = 0, \tag{3.9a}$$

$$\frac{\partial \bar{u}_i}{\partial t} + \frac{\partial}{\partial x_j}(\bar{u}_i \bar{u}_j) = -\frac{\partial \bar{p}}{\partial x_i} - \frac{\partial \tau_{ij}}{\partial x_j} + \frac{1}{Re}\frac{\partial^2 \bar{u}_i}{\partial x_i \partial x_j}, \tag{3.9b}$$

where the $Re$ number is calculated using a reference velocity $u_0$ and a reference lengthscale $l_0$. Due to the non-linear convection term of the Navier-Stokes equations, the dynamics of the resolved scales are not independent of those of the unresolved (sub-filter) scales. The effect of the unresolved scales are encapsulated in the additional stress-tensor like term, defined as:

$$\tau_{ij} = \overline{u_i u_j} - \overline{u}_i \overline{u}_j. \tag{3.10}$$

Since the SGS model to be presented belongs to the eddy-viscosity family, the stress tensor in Equation (3.10) can be split in a deviatoric and isotropic part. For incompressible flows, the term involving $\tau_{kk}$ can be added to the filtered pressure. The deviatoric term of the sub-grid scale stress tensor is then modeled as:

$$\tau_{ij}^{D} = -2\nu_t \bar{S}_{ij}, \quad \text{with } \bar{S}_{ij} = \frac{1}{2}\left(\frac{\partial \bar{u}_i}{\partial x_j}\frac{\partial \bar{u}_j}{\partial x_i}\right), \tag{3.11}$$

where $\nu_t$ is the eddy, turbulent or subgrid viscosity.

### 3.3.4 Subgrid-scale model

To determine the eddy viscosity $\nu_t$, initiated in previous section, a SGS model is needed. Previous studies (e.g. Lynch (2012)) investigated different SGS models in a realistic upper airway model. As a general conclusion, a selective Smagorinsky SGS model performed best on transitional flows in wall bounded regions (a characteristic of an upper airway flow). Therefore, for this thesis research, a selective Smagorinsky SGS model is used as is described in the paper by Sagaut et al. (1999). This is a quite complicated model, not standard available in OpenFOAM®, but necessary for correctly representing the physics inside the upper airway. For more information about other SGS models, please review the literature study of van der Velden (2012).

The Smagorinsky model assumes the following dependency:

$$\nu_t = (c_1\Delta)^2|S_{ij}|, \quad \text{with } |S_{ij}| = \sqrt{2\overline{S}_{ij}\overline{S}_{ij}}, \tag{3.12}$$

where the constant $c_1$ is taken equal to 0.1, $\Delta$ the earlier introduced cut-off length-scale of the filter and $|S|$ the mixing length for the sub-grid scales.

The selective model is a combination of a basic subgrid-viscosity model with a selection function (Sagaut et al. (1999)). The selection function, referred to as $f_s$, checks a specific property of the test field of the quantity $\bar{u}'$, and turns off the SGS model when this parameter does not correspond to a certain threshold which would indicate fully turbulent flow. In practice, a velocity field is assigned as turbulent (and should thus require a SGS model) if and only if the local angular fluctuations of the instantaneous vorticity is higher then a given threshold $\theta_0$. This parameter determines the three dimensionality of the flow, in this case, the angle between the vorticity vectors. The selection function can be mathematically written as:

$$f_s(\theta,\theta_0) = \left\{ \begin{array}{ll} 1 & \text{if } \theta \geq \theta_0 \\ r(\theta,\theta_0)^{1/2} & \text{else} \end{array} \right. , \tag{3.13}$$

with $r(\theta,\theta_0)$ defined as

$$r(\theta,\theta_0) = \frac{\tan^2(\theta/2)}{\tan^2(\theta_0/2)}. \tag{3.14}$$

where $\theta$ is defined as the angle between the average vorticity of all neighbors cells and the own cell's vorticity. The flow property criterion as given in Farhadi and Rahnama (2006) is used. From this the treshold angle of $\theta_0 = 20°$ is extracted.

Finally, the deviatoric term of the stress tensor reads:

$$\tau_{ij}^D = -2f_s(\theta, \theta_0)\nu_t \bar{S}_{ij}. \tag{3.15}$$

Numerically, a time integration and spatial discretization method is required. In general these will be addressed in Section 3.5.2. This paragraph only briefly describes the condition for the SGS model. A special treatment is used for the SGS term in case of time integration. This is based on a splitting which decouples the dispersive contributions, which can be written as $\nabla\nu_{SGS} \cdot (\nabla\bar{u} + \nabla^T\bar{u})$, from the dissipative ones, which read $\nu_{SGS}\nabla^2\bar{u}$. The dispersive ones should be determined explicitly, because they could affect the efficiency of the implicit method, while the second ones are treated implicitly (Sagaut et al. (1999)).

## 3.4 Boundary conditions

When solving the Navier-Stokes equations, one needs boundary and initial conditions. For an airway model, there are roughly three conditions which should be taken into account; the inlet, outlet and wall conditions. This section describes the general conditions, used in most of the simulations.

### 3.4.1 Inlet and outlet

Depending on the model different inlet and outlet conditions are used. In case of the boundary conditions (BC) for the velocity $u$, either a von Neumann, a Dirichlet or pressure driven normal velocity boundary condition is used. The last mentioned boundary condition is a special one. In that case, OpenFOAM®determines the inlet velocity based on the pressure gradient. This then results in a non-uniform flow. Therefore smoothing is applied near the inlet, to reduce peak velocities.

At the inlet and outlet, the pressure condition can be determined using a Dirichlet (fixed value at the wall) or a Von Neumann (fixed gradient at the wall) condition. Both conditions can cause reflections. In a direct acoustic calculation equation, this is a major problem. However, this may also affect a decoupled analysis. Lynch (2012) therefore tried to implement a sponge layer as formulated by Chen et al. (2004) for the pressure at the inlet and outlet. Poor results were obtained and the flow field became unstable. Hence, since for this thesis the main focus is on the acoustic simulation, a simpler boundary condition for the CFD pressure is used.

### 3.4.2 Wall modeling

Wall modeling in CFD can be roughly divided in three different methods: wall functions, hybrid methods (i.e. DES) and direct calculations. Important dimensionless parameter for wall modeling is the wall distance $y^+$, defined as:

$$y^+ \equiv \frac{u^* y}{\nu} \tag{3.16}$$

wherein $u^*$ equals the friction velocity at the nearest wall, $y$ the distance to the nearest wall and $\nu$ the local kinematic viscosity of the fluid. If one uses a high $y^+$ value of the cell near the wall, wall functions and hybrid methods are sufficient. However, other cases can give erroneous results. For example, wall functions will work well for fully developed non separated flow and hybrid methods will work good in separated flow but not in laminar flow. For the complex flow in the human upper airway, which was already described in Section 3.1, neither a wall function or hybrid method will fit. Therefore a direct wall approach is used for evaluating the separation, back flow, unsteadiness and laminar regions near the wall. With this direct approach, it is attempted to keep the $y^+$ value for the first cell layer within the viscous sub layer ($y^+ < 5$) (Breuer et al. (2007)).

## 3.5 Modeling software

This section brings a brief overview of the software used during this thesis to solve the fluid flow equations as well as the acoustic and structural equations. A detailed description of the software can be found in various literature and user manuals, widely available on the internet. In this section the basic principles are addressed, the discretization method is elaborated and the numerical schemes which are used are mentioned. Most of the information presented in this section is extracted from OpenFOAM (2011) programmers guide.

### 3.5.1 OpenFOAM®

This thesis is based on the research conducted in OpenFOAM®. There is a large variety of CFD packages available today to perform a decent LES simulation. Some of these software packages, already include a build-in acoustic solver. Examples are Fluent®, which couples various CFD solvers with an acoustic solver based on the intergral solution of the Ffowcs-Williams and Hawkings (FW-H) acoustic analogy. Another example is FINE Hexa®. Both software packages are extensively used to determine the flow and acoustical properties of various geometries.

There are various reasons why OpenFOAM®is chosen instead of other CFD packages. Some of the reasons are:

- Free software. Any other commercial package is very costly, making buying a volume license very expensive.

- Open source software, structured and written in C++. Therefore it is possible to adapt the code and build new functionalities, such as a in-house acoustic solver (discussed in next chapter). Due to the fact that it is open source, many discretization methods and post-processing tools are widely available.

- Community driven and increasingly popular in industry, making a fast evolution curve possible.

- Can work in parallel for fluid flow equations, without additional software costs. However, for Fluid Structure Interaction (FSI) algorithms, it is already much more difficult to work in parallel.

- It has been used for computing acoustic sources before. However, a standard solver was not available at the time of this thesis research.

Although, since OpenFOAM®is relatively new, program errors are still possible and often reported in the community. Therefore, validation and verification is still required and advisable. There is no support, it lacks of detailed documentation and it is hard to install the software. Due to the fact that there is also no Graphical User Interface (GUI, it is also a challenging job to work with OpenFOAM®. Benchmarks results are used in Chapter 6 to validate the results from the in-house solver in OpenFOAM®.

### 3.5.2 Discretization

As a numerical approach for the discretization of the governing equation, a Finite Volume (FV) approach is used. This sub section describes the details of the discretization of the governing equations in OpenFOAM®.

A FV model is based on a subdivision of the domain in space and time. Using the method of lines, a separation is made between the spatial and temporal discretizations. A FV method for spatial discretization results in a semi-discrete system, which still contains the continuous time derivative. Next, a time-marching method is required to solve for the quantities in time. For the spatial discretization, a set of control volumes (CV) is required. In each CV, a computational point (i.e. $\mathbf{P}$) is defined. The cell is bounded by a set of flat faces, given the generic label $f$. Each CV also consist of a vector $\mathbf{d}$, which connects the cell center of the adjacent volume and a vector $\mathbf{A}$ indicating the face normal area. OpenFOAM®defines the majority of the variables (such as $p$ and $\mathbf{u}$) at $\mathbf{P}$, resulting in a collocated variable arrangement. Next, due to the unsteady behavior of the flow, a temporal discretization is required as well. The time domain will be divided in a certain amount of time intervals/steps and a solution is obtained by marching $\Delta t$ from the initial condition.

With previous discussion in mind, it is now possible to discretize the filtered Navier Stokes equations as presented in Equation (3.8). According to the FV method, and after integration of the CV in space and time yields the following equation:

$$\int_V \nabla \cdot \overline{\mathbf{u}} dV = \int_{\partial V} d\mathbf{A} \cdot \overline{u} = \quad 0, \tag{3.17a}$$

$$\int_t^{t+\Delta t} \left[ \frac{d}{dt} \int_V \overline{\mathbf{u}} dV + \int_V \nabla \cdot (\overline{\mathbf{u}\mathbf{u}}) dV - \int_V \nabla \cdot \nu_{eff} (\nabla \overline{\mathbf{u}} + \nabla \overline{\mathbf{u}}^T) dV \right] dt = \\ - \int_t^{t+\Delta t} \left[ \int_V \frac{\nabla \overline{p}}{\rho} dV \right] dt. \tag{3.17b}$$

Equation (3.17) is a second-order equation due to the presence of a second derivative diffusion term. Hence, to obtain a reasonable accuracy, at least a second order method is required. Also, the temporal discretization scheme should be a second order scheme. Quantities such as pressure and velocity are assumed to vary linearly around a point in time $t$. Therefore, one can apply a Taylor series around that point, resulting in:

$$\phi(x) = \phi_P + (\mathbf{X} - \mathbf{X}_P) \cdot (\nabla \phi)_P + \mathcal{O}\left( |\mathbf{X} - \mathbf{X}_P|^2 \right), \tag{3.18a}$$

$$\frac{\partial \phi(t)}{\partial t} = \frac{3\phi(t + \Delta t) - 4\phi(t) + \phi(t - \Delta t)}{2\Delta t} + \mathcal{O}(\Delta t^2), \tag{3.18b}$$

where $\phi$ can represent any tensor field. Each term in the governing equations for the spatial and temporal discretization will be discussed separately in the following paragraphs.

### Spatial discretization

FV discretization of each term is formulated by first integrating the term over a cell volume $V$. Most spatial derivative terms are then converted to integrals over the cell surface $A$ bounding the volume using Gauss's theorem:

$$\int_V \nabla \star \phi dV = \int_A d\mathbf{A} \star \phi, \tag{3.19}$$

where $A$ is the surface area vector and $\star$ represent any tensor product, i.e. inner, outer and cross and their respective derivatives: divergence $\nabla \cdot \phi$, gradient $\nabla \phi$ and $\nabla \times \phi$. Volume and surface integrals are then linearized using appropriate schemes which are described in the next paragraphs.

**The Laplacian term** In the governing Equations (3.17) the diffusion term represents the laplacian term. The laplacian term is integrated over a control volume and linearized as follows:

$$\int_V \nabla \cdot (\nu \nabla \phi) dV = \int_A d\mathbf{A} \cdot (\nu \nabla \phi) = \sum_f \nu_f \mathbf{A}_f \cdot (\nabla \phi)_f. \tag{3.20}$$

The three different terms on the right hand side should be evaluated with an appropriate method. First, the scalar $\nu_f$ can be found by interpolation. Next, the complete term $\mathbf{A}_f \cdot (\nabla \phi)_f$ is very dependent on the mesh. If the mesh is orthogonal, the face gradient of $\phi$ can be expressed as:

$$\mathbf{A}_f \cdot (\nabla \phi)_f = |A_f| \frac{\phi_N - \phi_P}{|\mathbf{d}|}, \tag{3.21}$$

where the vectors $\mathbf{d}$ and $\mathbf{A}$ are parallel and $N$ refers to the neighboring cell of $P$. When the mesh is non-orthogonal, the second order accuracy is not valid anymore. Therefore, an additional explicit term is introduced reflecting the non-orthogonal properties. If the non-orthogonality is high, this can result in a negative coefficient which can lead to instability. Therefore, one should aim for a mesh with high orthogonality.

**The convection term** The convection term is integrated over a control volume and linearized as follows:

$$\int_V \nabla \cdot (\bar{\mathbf{u}}\phi) dV = \int_A d\mathbf{A} \cdot (\bar{\mathbf{u}}\phi) = \sum_f \mathbf{A}_f \cdot (\bar{\mathbf{u}})_f \phi_f = \sum_f F\phi_f, \tag{3.22}$$

where $F$ is defined as the volume flux through the face $F = \mathbf{A}\bar{\mathbf{U}}_f$. A second-order interpolation scheme is required to determine the face field $\phi_f$. Example of a centered scheme used in this thesis research is the linear interpolation (central differencing), while examples of Total Variation Diminishing (TVD) schemes used in this thesis are the Limited Linear Differencing and the Van Leer Limiter scheme.

### Temporal discretization

Like with the spatial discretization, there are many ways to perform a temporal discretization. The most important thing to keep in mind when selecting a temporal discretization scheme, is that each term in the transport Equation (3.17) should be second order accurate (otherwise a very small time-step is required). The following two paragraphs describe the first and second time derivative discretization. Note that the transport equation does not consist of a second order time derivative. However, this time derivative is later required for the discretization of the inhomogeneous wave equation, to determine the acoustic propagation.

**First time derivative** The first time derivative is integrated over a control volume as $\frac{\partial}{\partial t}\int_V \phi dV$. The term is discretized by a multi-step backward differencing scheme in time using:

- **new values** $\phi^n \equiv \phi(t + \Delta t)$ at the current time step;
- **old values** $\phi^0 \equiv \phi(t)$ that were stored from the previous time step;
- **old-old values** $\phi^{00} \equiv \phi(t - \Delta t)$ stored from a time step previous to the last.

Two second-order schemes are considered for the first time derivative. Firstly, a Crank Nicholson (CN) scheme can be used. It uses the trapezoid rule to discretize the spatial terms, thereby taking a mean of current values of $\phi^n$ and old values of $\phi^0$. It is unconditionally stable but the approximate solutions can still contain spurious oscillations if the ratio of the time steps to the square of space step is large. This makes the scheme very unsuitable for acoustic computations. Also, this scheme is considered to be rather expensive and therefore unwanted.

Another method is the second order backward differencing approach, which also stores the old-old values. This makes it a larger overhead in data storage compared with, for example, the first order Euler or CN scheme.

Throughout the simulation, the truncation error should be minimized. However, any small variation in derivatives and face fluxes can cause errors, which could have an undesirable effect on the LES simulation. The problem is due to the fact that such errors exceed the sub-grid diffusion. Therefore, to maintain stability throughout the entire simulation, the cell face Courant ($Co$) number should stay always below one:

$$Co = \frac{\mathbf{U}_f \cdot \mathbf{d}}{|\mathbf{d}|^2 \Delta t}, \tag{3.23}$$

where $\mathbf{U}_f$ is a characteristic velocity, in this case the velocity of the flow. Due to the limitation of the $Co$ number, the time-step in a LES simulation should be very small, resulting in a small temporal diffusion error.

**Second time derivative** The second time derivative is integrated over a control volume and linearized as $\frac{\partial}{\partial t} \int_V \frac{\partial \phi}{\partial t} dV$. For the second time derivative, the implicit Euler scheme is used, which is the standard option within the OpenFOAM®structure. Unfortunately, this scheme is only first order accurate in time.

### Coupling between pressure and velocity

If one considers the discretized form of the Navier-Stokes system, the form of the equations shows a linear dependence of velocity on pressure and vice-versa. This inter-equation coupling is also known as the velocity-pressure coupling. A special treatment is required in order to solve this coupling. For unsteady LES simulations, OpenFOAM®uses the Pressure Implicit with Splitting of Operators (PISO) method, as proposed by Issa (1986). The idea of PISO is as follows:

- The pressure-velocity system contains two complex coupling terms; the non-linearity in the convection term $\nabla \cdot (\mathbf{uu})$, handled using an iterative solution technique: $\nabla \cdot (\mathbf{u}^0 \mathbf{u}^n)$, where $\mathbf{u}^0$ is the current solution and $\mathbf{u}^n$ is the new solution. The other complex term is simple, based on the linear pressure-velocity coupling,
- on low Courant numbers (small time-step), the pressure-velocity coupling is much stronger than the non-linear coupling,
- it is therefore possible to repeat a number of pressure correctors without updating the discretization of the momentum equation (without updating $u^0$),
- in such a setup, the first pressure corrector will create a conservative velocity field, while the second and following establish the pressure distribution.

The pressure equation is based on a semi-discretized formulation of the momentum equations and reads:

$$a_p \bar{\mathbf{u}}_p = \mathbf{H}(\bar{\mathbf{u}}) - \nabla \bar{p}, \quad \text{with the operator } \mathbf{H}(\bar{\mathbf{u}}) = \mathbf{r} - \sum_N a_N^u \mathbf{u}_N, \tag{3.24}$$

wherein $a_p$ contains a set of coefficients of $\bar{\mathbf{u}}_p$ and $\mathbf{r}$ contains the portion of the temporal and spatial derivative which is not dependent on $\mathbf{u}_N$. The final form can be written as:

$$a_p \bar{\mathbf{u}}_p = \mathbf{H} - \sum_f \mathbf{A} \cdot \bar{p}_f, \tag{3.25a}$$

$$\sum_f \mathbf{A} \cdot \left(\frac{1}{a_p}\right)_f (\nabla \bar{p})_f = \sum_f \mathbf{A} \cdot \left(\frac{\mathbf{H}}{a_p}\right)_f. \tag{3.25b}$$

A detailed derivation can be found in Issa (1986). The PISO algorithm solves above equations successively.

### 3.5.3 Solvers

Now that the Navier-Stokes equations are discretized and the coupling method between the pressure and velocity is discussed, the governing equation can be solved to perform a LES simulation. The `pisoFoam` algorithm in OpenFOAM®is used as a starting point, which is an incompressible transient flow solver. Globally this algorithm involves the following steps:

1. Firstly, a RANS solution is used as initial field to start the LES simulation. Quantities as pressure, velocity, turbulent viscosity and face fluxes are used for this.
2. Turbulent properties are determined and updated, such as the selection function for the SGS model.
3. The pressure-velocity coupling is solved using the earlier described PISO algorithm. A prediction of the velocity field is made, based on previous fields and based on Equation (3.25). A Bi-Conjugate Gradient (PBiCG solver is used, which is applicable for asymmetric matrices. As a preconditioner, Diagonal Incomplete LU (DILU) is applied. Both solver and preconditioner are easily accessible withing the OpenFOAM®structure.
4. The **H** vector, presented in Equation (3.24) is updated by the new predicted velocities. Then the pressure can be solved via a Preconditioned Conjugate Gradient (PCG). As a preconditioner a Diagonal-based Incomplete Cholesky (DIC) method is used.
5. The pressure equation is solved iteratively and non-orthogonal correctors are used to improve the convergence.
6. The fluxes and velocities are updated with the new pressure results using the continuity formulations. The number of PISO loop correctors can be set to obtain a certain accuracy. For the simulation in this thesis, two correctors were required.

7. The simulation can proceed to calculate the acoustic sources, but first the structural solver is run.
8. Acoustic sub-cycles are set, and the acoustic solver is activated.
9. Simulation proceeds to next time step, and the calculated values are used to make a new initial guess for the solution.

The following two chapters are used to discuss step 7 and 8 in above process.

# Chapter 4

# Physics and modeling of sound

This chapter focuses on the acoustic analogies, presenting different methods to solve the acoustic wave equation. Numerical prediction of noise can be classified into two groups: the direct methods and the hybrid approaches. A schematic diagram of different Computational Aero-Acoustic (CAA) methods is given in figure 4.1. One can see that there are quite a few numerical approaches to simulate flow generated noise. The direct method will solve the compressible Navier-Stokes equations using Direct Numerical Simulation (DNS) which compute both sound and flow field together. The hybrid approach computes flow and acoustic field separately where a solution from the flow computation is required to start the acoustic computations. If performed parallel, this type of method reduces computational time and storage drastically while still keeping an accurate solution (Lynch (2012)). Therefore, a hybrid method is proposed in this thesis. Multiple methods exist and will be discussed in the following sections. The theory is mostly extracted from technical and PhD reports from Testa (2008), Zhu (2007), Caridi (2008), Uosukainen (2011) , Escobar (2007) and Wagner et al. (2007). However, firstly homogenous and non-homogenous wave propagation is discussed.

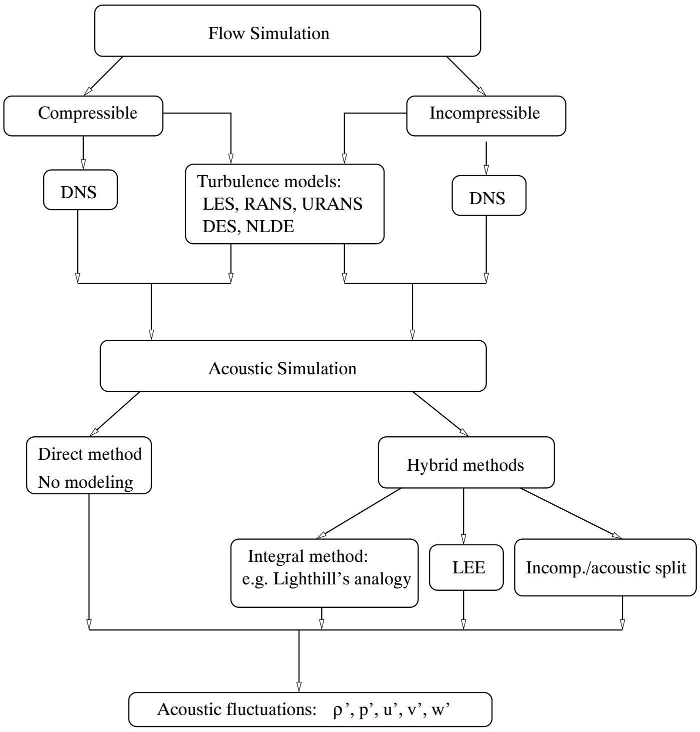

**Figure 4.1:** A diagram of CAA methods, Zhu (2007)

## 4.1 Wave propagation

### 4.1.1 Homogeneous

In order to derive the acoustic analogies used in this MSc thesis, firstly consider a zero averaged flow field and neglect the viscosity effects. Since an acoustic wave is related to all flow variables, each quantity can be considered as the sum of an averaged component and a fluctuating component, usually called the acoustic component:

$$p(\vec{x},t) = \bar{p} + p'(\vec{x},t), \tag{4.1a}$$

$$\rho(\vec{x},t) = \bar{\rho} + \rho'(\vec{x},t), \tag{4.1b}$$

$$u_i(\vec{x},t) = \bar{u}_i + u_i'(\vec{x},t). \tag{4.1c}$$

Because of the assumption of a zero uniform flow field, $\bar{u}_i = 0$, also the quantities $\bar{p}$ and $\bar{\rho}$ are considered to be constant. Thanks to these assumptions and neglecting any higher order terms, the Navier-Stokes equations can be linearized to:

$$\frac{\partial \rho'}{\partial t} + \bar{\rho}\frac{\partial u_i'}{\partial x_i} = 0, \tag{4.2a}$$

$$\bar{\rho}\frac{\partial u_i'}{\partial t} + \frac{\partial \rho'}{\partial x_i} = 0. \tag{4.2b}$$

When assuming the air to be a perfect gas, such that $p = \rho R T$, then

$$p' = c_0^2 \rho', \tag{4.3}$$

where $c_0^2 = \frac{\partial p}{\partial \rho}$ is the wave speed propagation in case of constant entropy. When taking the time derivative from Equation (4.2a) and the divergence from Equation (4.2b) and then subtracting the result from Equation (4.2a) from Equation (4.2b) the following relation results:

$$\frac{\partial^2 \rho'}{\partial t^2} - \frac{\partial^2 p'}{\partial x_i^2} = 0. \tag{4.4}$$

If one applies Equation (4.3) to Equation (4.4) it is possible to obtain a homogeneous equation completely defined for the pressure fluctuation:

$$\frac{1}{c_0^2}\frac{\partial^2 p'}{\partial t^2} - \frac{\partial^2 p'}{\partial x_i^2} = 0. \tag{4.5}$$

In a single dimensional case a solution of this equation can be written in the form

$$p(x,t) = f_1(c_0 t - x) + f_2(c_0 t + x), \tag{4.6}$$

where $f_1$ and $f_2$ are two arbitrary functions.

### 4.1.2 Non-homogeneous

A density based acoustic analogy often leads to a non-homogeneous wave equation. For better understanding the acoustic analogies, described in next sections, a brief introduction into non-homogeneous wave equations are given. No specific analytic solving details are discussed, since in this thesis the wave equation is solved numerically on the same grid as the fluid flow equations. This involves discretization (as discussed in Section 3.5.2) of the general differential equation of the acoustic analogy.

In general, a non-homogeneous wave equation assumes the following form

$$\left(\frac{1}{c_0^2}\frac{\partial^2}{\partial t^2} - \nabla^2\right) p = f(\vec{x}, t), \tag{4.7}$$

where $f(\vec{x}, t)$ is a generic distribution of sources. In order to solve this differential equation, a free field Green function is needed, which is defined as the solution of the wave equation related to a punctual and impulsive source.

## 4.2 Lighthill's analogy

The comprehensive study of CAA was started with Lighthill analogy, developed in the early 1950s with the purpose of reducing noise from jet engines (Lighthill (1952)). The acoustic relation is derived from the momentum and continuity equations. The equations of an arbitrary fluid motion can be rewritten by splitting terms and grouping the nonlinear terms into a source term. This source term is also known as the Lighthill stress tensor $T_{ij}$. The wave equation is described by a scalar partial differential equation (PDE) with fluctuating density as the only primary variable.

The mass and momentum equations for a compressible fluid motion without external forces are written as:

$$\frac{\partial \rho}{\partial t} + \frac{\partial}{\partial x_i}(\rho u_i) = 0, \tag{4.8a}$$

$$\frac{\partial}{\partial t}(\rho u_i) + \frac{\partial}{\partial x_j}(\rho u_i u_j) = -\frac{\partial p}{\partial x_i} + \frac{\partial \tau_{ij}}{\partial x_j}, \tag{4.8b}$$

where the viscous stress tensor for a Newtonian fluid is defined as:

$$\tau_{ij} = \mu \left[ \frac{\partial u_i}{\partial x_j} + \frac{\partial u_j}{\partial x_i} - \frac{2}{3} \left( \frac{\partial u_k}{\partial x_k} \right) \delta_{ij} \right], \tag{4.9}$$

where $\delta_{ij}$ is the Kronecker delta. Combining the Equations from (4.8), Lighthill's analogy can be derived:

$$\frac{\partial^2 \rho'}{\partial t^2} - c_0^2 \frac{\partial^2 \rho'}{\partial x_i^2} = \frac{\partial^2 T_{ij}}{\partial x_i \partial x_j}, \tag{4.10}$$

where the fluctuation density is equivalent to $\rho' = \rho - \rho_0$, with $\rho_0$ the fluid density at rest. The Ligthill stress tensor $T_{ij}$ is defined as

$$T_{ij} = \rho u_i u_j + \left[ (p - p_0) - c_0^2 (\rho - \rho_0) \right] \delta_{ij} - \tau_{ij}. \tag{4.11}$$

The viscosity term $\tau_{ij}$ is often neglected in case of very low Mach number air flows. Therefore the Lighthill's stress tensor is simplified by neglecting the viscous stress tensor $\tau_{ij}$. Next, if adiabaticity is well held and incompressibility is assumed, the Lighthill's stress tensor can be further simplified to:

$$T_{ij} = \rho_0 u_i u_j. \tag{4.12}$$

Note that these are the first simplifications made in this complete derivation. Therefore, Equation (4.10) and (4.11) did still represent the exact formulation and contained all physics.

Now, with the presented assumptions, the right hand side of Equation (4.10) can be fully calculated from a CFD simulation. When the noise source region is acoustically compact and no significant sources close to the computational boundary are present, it is allowed to decouple the acoustic and flow simulation. The implementation is discussed in Section 4.5.

## 4.3 The Ffowcs Williams-Hawkings analogy

Lighthill's theory is further developed and adapted by Williams and Hawkings (1969), Farassat (1996) and Brentner and Farassat (1998) who introduced the effect of surface loading (dipole) and thickness loading (monopole) contributions due to the presence of solid boundaries. This new analogy became a more generalized approach for noise predication, but was still based on Lighthill's acoustic analogy. The Ffowcs Williams and Hawkings's (FW-H) integral approach has some resemblance with Kirchhoff's theory, which was proposed in 1882. In Kirchhoff (1883), a wave equation is represented by a surface integral and was originally applied for light diffraction and electromagnetic problems.

In order to derive the governing differential equation, let $f(\mathbf{x}, t) = 0$ be a permeable surface moving with velocity $\mathbf{v}$, enclosing both the noise sources and solid surfaces such as the body surface; $f = 0$ is defined such that $\nabla f = \mathbf{n}$, where $\mathbf{n}$ is the outward unit normal vector, and $|\nabla f| = 1$. Furthermore, assume that $f > 0$ is outside the control surface, while $f < 0$ is located inside the control surface. For the sake of completeness, this is illustrated in figure 4.2. Assume that the interior motion is very simple, and consequently does not match the exterior flow at the boundaries. Thus, mass and momentum forces are introduced to maintain these discontinuities, which ultimately act as a sound generator. After the reformulation of mass and momentum equation they become

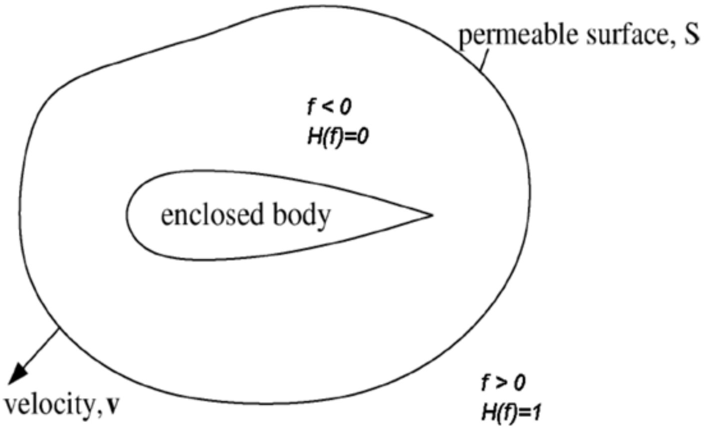

**Figure 4.2:** A permeable control surface, Testa (2008)

$$\frac{\partial \widetilde{\rho}}{\partial t} + \frac{\partial}{\partial x_i}\left(\widetilde{\rho u_i}\right) = \rho_0 v_i \delta(f) \frac{\partial f}{\partial x_i}, \tag{4.13a}$$

$$\frac{\partial \widetilde{\rho u_i}}{\partial t} + \frac{\partial}{\partial x_j}\left(\widetilde{\rho u_i u_j} + \widetilde{P_{ij}}\right) = P_{ij} \delta(f) \frac{\partial f}{\partial x_j}, \tag{4.13b}$$

where $v_i$ is the surface velocity. The presence and orientation of the surface is accounted for by the already introduced quantity $f$. Herewith, $\delta(f)$ is the one-dimensional delta function, which is zero everywhere except where $f = 0$, which thus means, on the surface. The equations above are governing the unbounded fluid and are valid throughout space, being their variables defined in the following way

$$\widetilde{\rho} = \begin{cases} \rho & f > 0 \\ \rho_0 & f < 0 \end{cases}, \tag{4.14a}$$

$$\widetilde{\rho u_i} = \begin{cases} \rho u_i & f > 0 \\ 0 & f < 0 \end{cases}, \tag{4.14b}$$

$$\widetilde{P_{ij}} = \begin{cases} (p - p_0)\delta_{ij} & f > 0 \\ 0 & f < 0 \end{cases}. \tag{4.14c}$$

In order to obtain the inhomogeneous wave equation governing the generation and propagation of sound, mass and momentum equations are differentiated with respect to $t$ and $x_i$ respectively. Next, $\widetilde{\rho u_i}$ is eliminated from the set of equations. Finally, the equation is changed to the dependent variable; the density perturbation $\rho'$. Now the FW-H equation can be written as

$$\frac{\partial^2 \rho'}{\partial t^2} - c_0^2 \frac{\partial^2 \rho'}{\partial x_i^2} = \underbrace{\frac{\partial^2}{\partial x_i \partial x_j} \left\{ \overline{T}_{ij} H(f) \right\}}_{\text{Quadrupole}} \underbrace{- \frac{\partial}{\partial x_i} \left( P_{ij} \delta(f) \frac{\partial f}{\partial x_j} \right)}_{\text{Dipole}} \underbrace{+ \frac{\partial}{\partial t} \left( \rho_0 v_i \delta(f) \frac{\partial f}{\partial x_i} \right)}_{\text{Monopole}} \tag{4.15}$$

In Equation (4.15), $P_{ij}$ represents the difference of the stress tensor from its mean value $p_0 \delta_{ij}$, and the complete term containing this tensor yields an integral over the surface of the obstacle. The generalized tensor $\overline{T}_{ij}$ is equal to Lighthill's tensor, already presented in Equation (4.12). The tensor is zero within each surface. This is accomplished by the Heaviside function $H(f)$ in Equation (4.15). The presence of both Dirac and Heaviside functions points out the different nature of the noise source terms at the right hand side of the wave equation. The last two terms in Equation (4.15) are called the pseudo-loading and pseudo-thickness terms whereas the first one is the quadrupole source term from Lighthill's analogy. The pseudo-thickness term describes the contribution of the net mass flux through a surface, while the pseudo-loading term is related to the net momentum flux. Mathematically, the pseudo-thickness and pseudo-loading terms correspond to the monopole and dipole non-stationary surface distributions respectively.

When the surface $f = 0$ is a solid surface, such as a body surface, the application of the impermeability condition implies that the normal velocity of the fluid is equal to the normal velocity of the surface, i.e. $u_n = v_n$. In that case, the monopole term can be interpreted as the noise generated by the displacement of the fluid forced by the body passage while the dipole term can be assigned to noise resulting from the pressure distribution upon the body surface. The sum of these two contributions provide an accurate noise prediction when extreme transonic flow conditions do not occur and noise is not characterized by turbulence phenomena. See for example the results from Hanson and Fink (1979), Schmitz and Yu (1986) and Farassat and Tadghighi (1990). These studies show, that when pressure, density and velocity fields surrounding the source of noise are related to high-speed transonic operating conditions or to massive turbulence flow, the inclusion of the non-linear quadrupole volume term (non-linear due to the $\mathbf{u} \otimes \mathbf{u}$ term) is required. However, this requires a much finer mesh in order to accurately capture the volume source term. This increases the computational time enormously. In case of only a simulation including monopole and dipole sources, a coarser mesh should be sufficient.

## 4.4 Curle's analogy

The acoustic differences between Curle and FW-H are similar since both of these approaches do take into account the presence of solid bodies. However, it is worthwhile mentioning the work done by Curle (1955), since his theory was developed earlier than FW-H, but without considering the effect of surface motion. This method is a widely used method inside CAA, for example in noise generation from open cavities and flow induced cylinder noise in a uniform flow (Zhu (2007)).

The starting point of the derivation of Curle's analogy is similar to the one by FW-H, presented in previous section. Assuming that the fluid is divided by the stationary solid body $S$ and the fluid is at rest at infinity, Curle wrote the solution of Lighthill's equation with surface and volume source terms. This resulted in Equation (4.16), where a non-homogeneous wave equation is shown together with a surface term (dipole source term) and a volume source term (quadrupole source term). The equation is indeed almost similar, compared with Equation (4.15).

$$\frac{\partial^2 \rho'}{\partial t^2} - c_0^2 \frac{\partial^2 \rho'}{\partial x_i^2} = \underbrace{\frac{\partial^2}{\partial x_i \partial x_j}\{\overline{T}_{ij} H(f)\}}_{\text{Quadrupole}} \underbrace{- \frac{\partial}{\partial x_i}\left(P_{ij}\delta(f)\frac{\partial f}{\partial x_j}\right)}_{\text{Dipole}}. \tag{4.16}$$

To further clarify the terms in above equation, it is useful to look at the magnitude of both terms. Assuming that the characteristic length scale divided by the frequency and the Lighthill's stress tensor are proportional to $u_0$ and $\rho_0 u_0^2$, the pressure fluctuation for the quadrupole term can be written such as, Caridi (2008):

$$p'(\mathbf{x}, t) \sim \rho_0 u_0^2 M^2 \frac{L}{\|\mathbf{u}\|}. \tag{4.17}$$

In this equation, $L$ is a characteristic length scale. Acoustic power density is defined as:

$$I_{ac} = \frac{p'^2}{\rho_0 c_0}. \tag{4.18}$$

Combining Equations (4.17) and (4.18) a dimensional analysis can be performed on the quadrupole term. For the quadrupole sources, Lighthill found out that the intensity of sound varies with the eight power of the mean velocity:

$$I_{ac_{quad}} \sim \rho_0 u_0^3 M^5 \frac{L^2}{\|x\|^2} \sim u_0^3 \cdot M^5. \tag{4.19}$$

Curle performed the same analysis for the dipole source. For this source, the proportionality of the pressure fluctuation and the acoustic intensity are:

$$p'(\mathbf{x}, t) \sim \rho_0 u_0^2 M \frac{L}{\|\mathbf{u}\|}, \tag{4.20a}$$

$$I_{ac_{dip}} \sim \rho_0 u_0^3 M^3 \frac{L^2}{\|x\|^2} \sim u_0^3 \cdot M^3. \tag{4.20b}$$

Comparing the quadrupole and dipole source term: $I_{ac_{quad}}/I_{ac_{dip}} \sim M^2$ it is possible to say that in the case of $M \ll 1$ the contribution of the surface sources (dipole term) is dominant.

## 4.5 Implementation into OpenFOAM®

This section explains the modeling of the acoustics inside OpenFOAM®. Firstly, the idea behind the coupling of the fluid and acoustic analogy is discussed. In further sections, the implementation of the source terms is shown.

### 4.5.1 Hybrid method

The introduction of this chapter already contained a comparison between direct and hybrid methods. This section is to clarify the choice made in the introduction by presenting the hybrid approach in a nutshell.

The hybrid analogy is based on decoupling the flow simulation from the acoustic simulation. With the flow computation, one creates a source field for the acoustic simulation. During the acoustic computation, source field data is post-processed in a non-homogeneous wave equation. This approach results in one fundamental assumption; a one-way coupling between the flow and the acoustics. It is assumed that unsteady flow produces sound and affect its propagation, however sound waves do not effect the flow field significantly. Therefore, the principal application for this hybrid approach are flow fields with no strong coupling.

To determine the source terms accurately, a preferred simulation method for the flow exists. This scheme must be accurate and must be able to collect unsteady, broadband turbulence data. A LES simulation satisfies these requirements. Especially for low Mach number applications, such as the upper airway tract, a hybrid LES acoustic solver can reduce CPU costs drastically compared with a DNS simulation, which requires a very high resolution for the simulation.

In this thesis, the source terms of the non-homogenous wave equation are extracted from OpenFOAM®. Also the wave equation itself is modeled in OpenFOAM®. This has several advantages: First of all, this allows for a quasi-simultaneous simulation of both the flow and acoustic simulation. Hence, after every flow time-step, several acoustic time-steps are performed. Since in general, the time step for the acoustic simulation needs to be smaller because of the higher wave velocity. Because the acoustic simulation is done directly after the CFD computation, there is no need to save the data every time-step thereby reducing memory demands. However, as a disadvantage, it is impossible to only redo the acoustic simulation if, for example, another acoustic analogy is preferred. Another advantage is the reduced programming effort, since both temporal and spatial discretization schemes are widely available within the OpenFOAM®structure. Also post-process algorithms are available, making the data access and analysis easier and more convenient. Finally, solving a PDE instead of the integral solution makes it possible to account for reflection and propagation, which is very crucial in an interior acoustic simulation. An integral solution of the FW-H analogy will be therefore unsuitable for any interior analysis.

### 4.5.2 Quadrupole source term

The quadrupole source term, depicted on the right hand side of Equation (4.10) consists of the Lighthill stress tensor. In case of a low Mach number, high Reynolds number flow, the tensor reduces to Equation (4.12). At the time of this MSc thesis, OpenFOAM®did not include any code to compute acoustic source terms. However, thanks to OpenFOAM®'s object oriented structure, the quadrupole source term can be easily extracted. The source term was simply declared as a scalar field. There are also pre-defined operations on the these general fields such as divergence, which is required to determine the quadrupole term. The framework also allows the discretization to be chosen at run time, saving the programmer a lot of work and making it easier to understand.

After each CFD time-step, the acoustic sub-cycle is start. In this cycle, the quadrupole source term is determined using:

$$Q_{quad} = \rho \cdot \nabla \left[ \nabla \left( \mathbf{U} \times \mathbf{U} \right) \right], \tag{4.21}$$

```
quadrupoleTerm = rho * fvc::div(fvc::div(U*U));
```

Here, `U*U` represents the velocity tensor field. Taking two times the divergence results in a scalar source field. This source field is added on the right hand side of the wave equation.

### 4.5.3 Dipole source term

The dipole source term was already introduced in Equation (4.16). It consist of the pressure stress tensor (Relation (4.14c)). In OpenFOAM®, the divergence is evaluated, which takes into account face interpolation of the volume pressure field. To verify the dimensions, the surface area is used (`magSf()`) and multiplied with a scalar $\gamma$, which is 1 at the wall and 0 on the inside. This way, the boundary can easily be accessed. Finally, the expression is multiplied with the density, since in OpenFOAM®the pressure is defined as a density normalized pressure. The code listing is summarized below:

$$Q_{dip} = -\rho \cdot \nabla \left( \gamma p \right), \tag{4.22}$$

```
dipoleTerm = rho*fvc::div((-mesh.magSf()*gammaField),p);
```

This source term can also be added (with a minus sign though) to the right hand side of the wave equation.

### 4.5.4 Monopole source term

The monopole source term requires information from the boundary. This information can only be obtained, when solving the stresses inside the structure surrounded by the fluid domain.

Details about the analysis method for the structure is found in the next chapter. For now, only the implementation of the source term is of interest. The term, which can be found in Equation (4.15), involves an acceleration term of the solid multiplied with the density of the fluid. This is obtained via:

$$\rho \cdot \frac{\partial^2 D}{\partial t^2}, \tag{4.23}$$

```
d2Ddt2 = rho * fvc::d2dt2(D);
```

Next, the magnitude of the acceleration is stored on the fluid-solid boundary, finalizing the monopole source term:

$$Q_{mon} = \left(\rho \cdot \frac{\partial^2 D}{\partial t^2}\right) \cdot \mathbf{n}, \tag{4.24}$$

```
\begin{verbatim}
monopoleTerm.boundaryField()[fluidPatchID] =
        interpolatorSolidFluid.faceInterpolate
                (d2Ddt2.boundaryField()[solidPatchID]) &
        (-mesh.Sf().boundaryField()[fluidPatchID]/
                mesh.V()[fluidPatchID]);
```

where `interpolatorSolidFluid` interpolates the values from the structural mesh to the fluid mesh using the `zoneToZoneInterpolation` algorithm inside OpenFOAM®1.6-ext. `V()` indicates the volume of a cell. This second term is important, for dimensionalizing the monopole term. More information about the structure, as well as a different method to incorporate for monopole sources is discussed in Chapter 5.

### 4.5.5 Density equation

Now that the source terms are introduced, it is possible to solve the non-homogeneous wave equation. The wave equation is programmed in OpenFOAM®as a normal PDE in such a way that you can easily describe the boundary and initial values. The code listing reads:

$$\frac{\partial^2 \rho'}{\partial t^2} - c_0^2 \frac{\partial^2 \rho'}{\partial x_i^2} = Q_{quad} - Q_{dip} + Q_{mon}, \tag{4.25}$$

```
solve((fvm::d2dt2(rhoPrime) - sqr(c0) * fvm::laplacian(rhoPrime)==
        quadrupoleTerm - dipoleTerm + monopoleTerm))
```

in the case that both quadrupole, dipole term and monopole term are used as source terms. The main advantage of solving a PDE instead of a integral solution of an acoustic analogy, is that one can consider boundary and initial conditions. This way, reflection and propagation of the noise can easily be taken into account.

### Inlets and outlets

At the inlet and outlet the density perturbations are prescribed by a convective outlet boundary condition, which is a subset of a Robin boundary condition. This allows the acoustic waves to leave the domain without any reflection. A convective outlet boundary condition for density perturbations can be written as:

$$\frac{d\rho'}{dt} + c_0 \frac{d\rho'}{dn} = 0. \tag{4.26}$$

In this equation, the spatial derivative is taken normal to the boundary. The initial value of the density perturbation field is simply a zero uniform field.

### Walls

For describing the walls inside an acoustic simulation, different possibilities arise. A physically correct representation near a rigid wall is to set the molecular velocity at the wall to zero. To make sure molecules do not travel normal to wall, there cannot be a pressure gradient at the wall. Hence, at the wall, the acoustic simulation contains a zero pressure gradient condition.

Another possibility is to also describe the propagation, transmittance and reflectance of the wall. In real life, not all the waves are reflected. Part of the waves are namely absorbed and transmitted due to the fact that the walls are not completely rigid, i.e. they can vibrate. To give a sense about impedance levels, Table 4.1 provides some numbers. The higher the acoustic impedance, the more difficult the material will transmit. This impedance level can be translated to a impedance boundary condition at the wall, as derived by Spa et al. (2010). The equation reads:

**Table 4.1:** Approximate values for the impedance of different parts inside the human body, Baun (2009), Hu et al. (2009) and Ludwig (1950)

| **Material** | **Impedance** [MRayl] |
|---|---:|
| Air | 0.0004 |
| Fat | 1.38 |
| Water | 1.48 |
| Blood | 1.51 |
| Soft tissue (average) | 1.63 |
| Muscle | 1.7 |
| Bone | 7.8 |

$$\frac{\partial p(\mathbf{x},t)}{\partial t} = -\frac{Z}{\rho}\frac{\partial p(\mathbf{x},t)}{\partial \mathbf{n}}, \tag{4.27}$$

wherein $p$ is the pressure, $\rho$ is the density and $Z$ is the acoustic impedance. This equation shows similarities with Equation 4.26, therefore making the implementation straightforward.

Lynch (2012) tested this boundary condition in his MSc thesis. He compared the zero gradient boundary condition with the impedance boundary condition (Equation (4.27)). The second condition allows a small part of the signal to be transmitted through the wall. Using the impedance value for human tissue (shown in Table 4.1), it was concluded that this type of boundary condition hardly affects the sound pressure results. Only a difference of 0.5 dB was observed. Therefore, for this thesis research, a simple zero gradient boundary condition is used. In chapter 5, issues such as vibration will be addressed.

## 4.6 Acoustic relations

After OpenFOAM®solves the density equation, as described in Section 4.5.5, some post-processing steps needs to be conducted to get some useful results. This section describes some acoustic relations, useful for post-processing.

First of all, in each geometric model, probes exist which collect the density perturbation ($\rho'$) data. These probes are located at strategic locations, such as near the inlet, outlet and before and after constrictions. This raw data is corrected using a moving average, where signals below the cut-off frequency are filtered and detrended. From this result, the fluctuating signal is collected by subtraction.

From this signal the Sound Pressure Level (SPL) is extracted. Pressure disturbances $p'$ are normally very low compared to the atmospheric pressure. A human ear can detect fluctuations between 20 Hz and 20 kHz. Due to this large range, the SPL is expressed on a logarithmic scale as:

$$SPL = 20 \log_{10} \frac{p'_{RMS}}{p'_{ref}}, \tag{4.28}$$

wherein the SPL is given in decibels (dB) and $p'_{ref} = 2 \cdot 10^{-5} Pa$. This corresponds to a $SPL$ of 0 dB.

Also, the sound intensity level ($SI$) is an interesting quantity to compare results. It is given by:

$$SI = 10 \log_{10} \left( \frac{\langle I \rangle}{I_{ref}} \right), \tag{4.29}$$

wherein $I_{ref} = 10^{-12} W m^{-2}$ and $\langle I \rangle = p'^2 / \rho_0 c_0$. Both $SPL$ and $SI$ are plotted in a frequency spectrum, by using a Fourier transform inside Matlab®. This is done after the line is detrended by a moving average, in order to filter out the low frequency noise.

# Chapter 5

# Physics and modeling of structure interaction model

Now that the fluid flow and acoustic theory are introduced, the theory behind the structural model should be discussed. A structural model is used for the interaction with the acoustic domain to incorporate for the vibrations on the wall of the geometry. The displacements on the wall are considered to be very small, and have therefore a negligible effect on the fluid flow. However, due to the soft tissue in the upper airway, large accelerations can occur. These accelerations can be incorporated by a monopole source in the FWH analogy, presented in the previous chapter.

This chapter starts by introducing the computational model, a finite volume linear stress analysis solver to solve for the stresses inside the solid (derived from Turteltaub (2009), Jasak and Weller (2000) and Rixen (2010)). Next the interface and boundary conditions are extensively discussed, as well as the weak coupling mechanism with the fluid flow and acoustical model.

## 5.1 Mathematical model

### 5.1.1 FEM or FVM

Currently, a Finite Element Method (FEM) solver dominates the area of stress analysis. These solvers are normally based on the variational principle, involving pre-defined shape functions depending on the topology of the element, usually extended to higher order discretization. Since this thesis research focuses on the parallel and simultaneous implementation of flow and sound into OpenFOAM®, it is useful to also implement the structural solver using OpenFOAM®based on the FVM analogy. This choice requires a trade-off between both methods. Some of the advantages, claimed by Jasak and Weller (2000) of using a FVM as structural solver are summarized below:

- FVM is inherently good at treating complicated, coupled and non-linear differential equations. If the mathematical model becomes more complex, a FVM outperforms a FEM.
- FVM is more efficient, since it has been developed for meshes of milions of cells, normally required for CFD analysis.

However it is good to know that both FVM and FEM can resolve the same PDE when the discretization is fine enough. Also, using a FEM model, it is easier to get higher order accuracy. But, for the structural model to be investigated, the structure dynamics is simple enough to be represented by an accurately fine FV mesh. And, taken into account the fact that when using OpenFOAM®to solve for the stresses in the structure, one can program everything simultaneously. Hence, FVM is a good choice to solve for the displacements in the structure.

### 5.1.2 Governing elastodynamic equations

Based on the balance of linear momentum ($\mathbf{F} = m\mathbf{a}$), a description of the force balance can be derived. For this, assume a simple mathematical model; a linear elastic solid. The force balance for the solid body element in differential form reads

$$\frac{\partial^2(\rho\mathbf{x})}{\partial t^2} - \nabla \cdot \sigma = \rho\mathbf{f}, \tag{5.1}$$

wherein $\mathbf{x}$ indicated the displacement vector, $\rho$ is the density of the solid, $\mathbf{f}$ is the body force vector and $\sigma$ is the stress tensor. For the specific case of an isotropic material, the strain tensor$\epsilon$ is defined (in terms of $\mathbf{x}$) as

$$\epsilon = \frac{1}{2}\left[\nabla\mathbf{x} + (\nabla\mathbf{x})^T\right]. \tag{5.2}$$

Consequently, the stress is related to the displacements using Hooke's law, relating stress and strain tensors. This closes the system using

$$\sigma = 2\mu\epsilon + \lambda\,\mathrm{tr}(\epsilon)\mathbf{I}, \tag{5.3}$$

where $\mathbf{I}$ is the unit tensor, "tr()" the trace (i.e. $\sum_{i=1}^{n} a_{ii}$) and $\mu$ and $\lambda$ are Lamé's coefficients, relating to Young's modulus of elasticity $E$ and Poisson's ratio $\nu$ as

$$\mu = \frac{E}{2(1+\nu)}, \tag{5.4}$$

and

$$\lambda = \begin{cases} \frac{\nu E}{(1+\nu)(1-\nu)} & \text{for plane stress} \\ \frac{\nu E}{(1+\nu)(1-2\nu)} & \text{for plane strain and 3D} \end{cases}. \tag{5.5}$$

With this information, the governing equation in (5.1) can be rewritten to its final expression:

$$\frac{\partial^2(\rho\mathbf{x})}{\partial t^2} - \nabla\cdot\left[\mu\nabla\mathbf{x} + \mu\left(\nabla\mathbf{x}\right)^T + \lambda\mathbf{I}\,\mathrm{tr}\left(\nabla\mathbf{x}\right)\right] = \rho\mathbf{f}, \tag{5.6}$$

making it an expression with the displacement vector $\mathbf{x}$ as primitive variable. Common values for the material properties of human skin, which are used in the simulation, are entered in Table 5.1.

**Table 5.1:** Mechanical properties of human skin, CES-Edupack (2011)

| **Property** | **Value** |
|---|---|
| Density [kg/m3] | $1110 - 1270$ |
| Poisson's ratio [-] | $0.35 - 0.43$ |
| Young's modulus [MPa] | $1 - 4$ |

### 5.1.3 Discretization, preconditioner and solver

The FV model of equation (5.6) can be discretized in a similar way as elaborated in Section 3.5.2. Integrating the control volume ($V_P$) in space and time yields:

$$\int_{V_p}\frac{\partial^2(\rho\mathbf{x})}{\partial t^2}dV - \int_{\partial V_p} d\mathbf{s}\cdot\left[\mu\nabla\mathbf{x} + \mu\left(\nabla\mathbf{x}\right)^T + \lambda\mathbf{I}\,\mathrm{tr}\left(\nabla\mathbf{x}\right)\right] = \int_{V_p}\rho\mathbf{f}dV, \tag{5.7}$$

where the spatial and time discretization schemes are explained in Section 3.5.2.

A special generalized Geometric-Algebraic Multi-Grid solver (GAMG) was selected as a preconditioner to solve the force balance equation. GAMG, uses the principle of generating a quick solution on a mesh with a small number of cells. Next, mapping this solution on a finer mesh and using this as an initial guess to obtain an accurate solution on the finer mesh (OpenFOAM (2011)). GAMG can be much faster than standard methods when the increase in speed by first solving coarser meshes outweighs the additional costs of mesh refinement.

The force-balance equation (5.6) was already pre-programmed in OpenFOAM®under the solver name `solidDisplacementFoam`. For this thesis research, an adaption of this solver is made and implemented in the in-house fluid-structure-acoustic interaction solver, creating a solver named `vibroAcousticFoam`. Details of the implementation and coupling are discussed in the next section.

## 5.2 Interface conditions and coupling procedures

### 5.2.1 Coupling between solvers

The force-balance equation requires input from either a body force or a boundary condition. Since the structural model is going to be used for an acoustic analysis, interface conditions from the fluid domain will be used for starting up the structural solver. For the sake of completeness, a schematic overview of the coupling between the fluid, structure and acoustic solver is given in Figure 5.1.

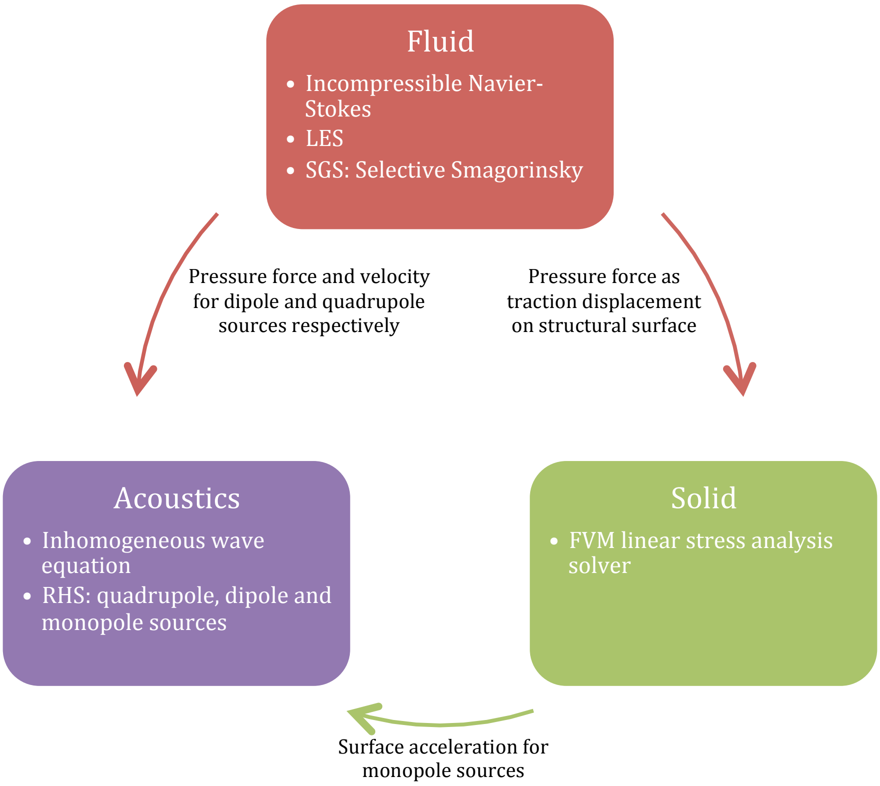

**Figure 5.1:** Fluid-Structure-Acoustic interaction: a schematic overview of all coupling procedures

The first step in the complete cycle of the in-house fluid-structure-acoustic solver is to solve the Navier Stokes equations. Details can be found in Chapter 3. Afterwards, it is possible to determine the quadrupole and dipole sources for the acoustic solver. For this step, only the flow quantities velocity and pressure are required to set up the quadrupole and dipole source term respectively. The acoustic solver cannot be started yet, since the monopole source term is still missing. This term requires acceleration data (i.e. vibrational data) from the structure. Therefore, the next step is to evaluate the structural solver. When the acoustic field is surrounded by flexible structures, which is the case in an upper human airway, an interface condition between the boundaries has to be used. Details of these coupling conditions are already briefly addressed in Figure 5.1, but will be elaborated in the upcoming paragraphs.

After the structure is solved, the sub-cycles of the acoustic solver can be started. As can be concluded from Figure 5.1, all coupling mechanism are weak couplings, i.e. one way coupling, so that the three different fields are solved independently. In a following research, it might be worthwhile to include a strong coupling between the acoustic and structural solver. This way, the acoustic volume sources (from the quadrupole source term) can be propagated through the structure, creating new acoustic sources at other boundaries of the domain (i.e. vibrations).

### 5.2.2 Structural interface conditions

From the fluid simulation, the resulting pressure is obtained and set as an equilibrium equation for the structural stresses on the interface. This means that the pressure in the fluid domain is applied as a force on the structural surface, such that (Rixen (2010)):

$$\sigma \cdot \mathbf{n} = -p\mathbf{n}. \tag{5.8}$$

This can thus be interpreted in such a way that the pressure force is like an external force that must equilibrate the internal structural stresses (proportional to the strains, thus to the displacement spatial derivatives). In OpenFOAM®, this results in an interpolation function between the two different patches of the two different meshes (fluid and solid). The pressure can be set as a traction boundary condition, which specifies the force on the boundary face. The governing equation actually represents the force balance for the control volume, so the result of Equation (5.8) can directly be added to the right hand side of Equation (5.6). For simplicity, the boundary that is not connected with the fluid interface is assumed to be clamped; no displacements are allowed ($\mathbf{x} = 0$). Another possibility is to fix only the top and button edges of the model. However, this can lead to unwanted oscillations. And since only acceleration data at the interface surface is required, the previous method seems to be sufficient. Another much more realistic option is to make use of back pressure. The pressure set on the interface wall will be copied and translated to the free wall, thereby creating a more realistic model of an upper airway.

The structural solver solves for the stresses and displacements in the model. Using an interpolation scheme, the resulting acceleration field (second derivative of the displacement field) is transferred from the solid patch to the fluid patch. The acceleration is then used in the monopole source term, shown in Equation (4.15). This source term can also be interpreted as a second compatibility equation, stating that the normal velocity of the structural surface should equal the velocity of the fluid on the boundary. This can be written as (Rixen (2010)):

$$\mathbf{n} \cdot \frac{\partial \mathbf{x}}{\partial t} = \mathbf{n} \cdot \mathbf{u}, \tag{5.9}$$

on the boundary. Since the fluid simulation is weakly coupled with the acoustic simulation, and the fluid velocity is not an unknown in the wave equation, the equation should be rewritten into a condition for the acoustic pressure/density perturbation. First, take the time time derivative of equation (5.9):

$$\mathbf{n} \cdot \frac{\partial^2 \mathbf{x}}{\partial t^2} = \mathbf{n} \cdot \frac{\partial \mathbf{u}}{\partial t}. \tag{5.10}$$

When using the linearized momentum equation (i.e. $\rho_0 \frac{\partial \mathbf{u}}{\partial t} = -\nabla p$), the final relation can be obtained:

$$\mathbf{n} \cdot \frac{\partial^2 \mathbf{x}}{\partial t^2} = \mathbf{n} \cdot \frac{-\nabla p}{\rho_0}. \tag{5.11}$$

Equation (5.11) is implemented as a fixed gradient (Von Neumann) boundary condition in OpenFOAM®. This boundary condition is changed after every cycle. Note that to translate from the acoustic pressure to the acoustic density field, the conversion from Relation (4.3) is used. The final implementation in OpenFOAM®is similar to the last steps of the monopole source term, elaborated in the previous chapter.

Now that all the parameters for the source terms are known, the acoustic wave equation (Equation (4.15)) can be solved. By reducing the time step within the fluid cycle, sub-cycles are created to keep the acoustic Courant number below the 1.0.

# Chapter 6

# Acoustic and vibro-acoustic verification and validation

After introducing the theory in the previous chapters, it is time to validate its implementation in OpenFOAM®. Firstly, the quadrupole, dipole and monopole terms are checked via an analytical solution. Finally, the (vibro)-acoustic and CFD results of the diaphragm model are shown for all acoustic sources.

## 6.1 Quadrupole source term

This section deals with validating the implementation of the quadrupole source term, also known as Lighthill's source term. Quadrupole sources were validated before in the field of CAA, usually using a co-rotating vortex pair (Link et al. (2009), Escobar (2007), Piellard and Bailly (2008) and Liow et al. (2001)). The possibility of an analytical approach makes this validation model so interesting. In the upcoming sections, the model, the analytical expression and the results are presented.

### 6.1.1 Model and approach

Vorticity acceleration produces an acoustic radiation, as investigated by Lighthill (1952). This mechanism is highlighted in the particular two-dimensional case of two co-rotating vortices. The co-rotating vortex pair consists of two point vortices which are separated by a fixed distance of $2r_0$ with a circulation intensity of $\Gamma$. A schematic illustration can be found in Figure 6.1. The vortex core rotates around each other with a period of $T = 8\pi^2 r_0^2/\Gamma$. The angular speed of the swirling flow is given by $\omega = \Gamma/4\pi r_0^2$ and the circumferential Mach number is given by $M_r = \Gamma/4\pi r_0 c_0$.

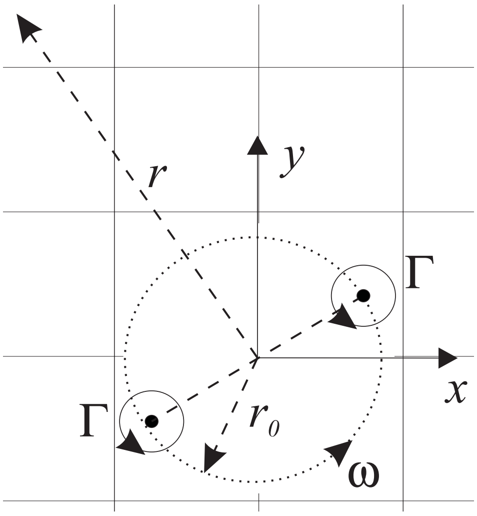

**Figure 6.1:** Schematic drawing of the co-rotating vortices, Escobar (2007)

The analytical solution of the acoustic pressure fluctuations from the co-rotating vortex pair is derived from Lighthill's acoustic analogy, together with the time-harmonic expression of Möhring's (vortex sound theory). By using the method of Matched Asymptotic Expansions (MAE), the solution for the far field was derived (Mitchell et al. (1995)):

$$P'(r,\theta,t) = \frac{-\rho_0\Gamma^4}{64\pi^3 r_0^4 c_0^2}\left[\mathrm{J}_2\left(\frac{2\omega r}{c_0}\right)\sin(2\theta+2\omega t) + \mathrm{Y}_2\left(\frac{2\omega r}{c_0}\right)\cos(2\theta+2\omega t)\right], \tag{6.1}$$

where $\mathrm{J}_2(z)$ and $\mathrm{Y}_2(z)$ are the second-order Bessel functions of the first and second kind respectively and $r$ and $\theta$ the locations in the polar coordinate system.

The induced flow field is assumed to be inviscid and incompressible. Since at the origin of the setup a singularity occurs, a vortex core model is applied, Escobar (2007). The flow can be determined numerically by the differentiation of the following complex potential function $\Phi(z,t)$:

$$\Phi(z,t) = \frac{\Gamma}{2\pi i}\ln z^2\left(1-\frac{b^2}{z^2}\right), \tag{6.2}$$

wherein $z = re^{i\theta}$ and $b = r_0 e^{i\omega t}$. Assuming that $\|\frac{z}{b}\| \gg 1$, the equation can be simplified as:

$$\Phi(z,t) = \frac{\Gamma}{2\pi i}\ln z^2 - \frac{\Gamma}{2\pi i}\left(\frac{b^2}{z^2}\right). \tag{6.3}$$

The first term represents the steady vortical flow, whereas the second term represents the fluctuation due to the vortex motion. Within the vortex core model, the velocity components are given by:

$$u_x = -\frac{\Gamma}{2\pi}\frac{y}{r_c + x^2 + y^2}, \tag{6.4a}$$

$$u_y = \frac{\Gamma}{2\pi}\frac{x}{r_c + x^2 + y^2}, \tag{6.4b}$$

with $r_c$ indicating the core radius. The hybrid methodology, as discussed in Chapter 4, will be used to evaluate and validate the acoustic field induced by the co-rotating vortex pair. The acoustic sources are obtained from the hydrodynamic velocity field. The flow field is initialised as the vector sum of the velocity field of each vortex core. At the computational boundaries, the velocity field is based on the analytical solution of a single vortex of circulation $\Gamma$. For simplicity reasons, the acoustical domain equals the fluid domain. Therefore no interpolation scheme was required for mapping the source term. Also three different meshes were used, from a coarse mesh to fine mesh ($0.04 \cdot 0.04$ m, $0.02 \cdot 0.02$ m and $0.01 \cdot 0.01$ m).

For evaluation of above equations, the density is chosen to be $\rho_0 = 1$ kg/m3, the speed of sound equals $c_0 = 1$ m/s, the spinning radius equals $r_0 = 1$ m and the core radius equals $r_c = 0.1$ m. The circulation is set to 1.00531 m/s (similar as in Link et al. (2009)). This choice leads to a Mach number of 0.08 and a wave length of approximately 39 m. In all computations presented in this section, the flow field is evaluated on a numerical region of 200 x 200 m. In OpenFOAM®, the quadrupole source term is extracted from the flow field (which was evaluated in Matlab®using the above equations), and used for solving the inhomogeneous wave equation (Section 4.5.5). The boundary of the domain is modeled via a convective outlet boundary condition and the analytical fluctuating pressure function, indicated in Equation (6.9), is applied at the surface source.

### 6.1.2 Results

First of all, in Figure 6.2, the overall contour plot of the acoustic pressure distribution at $t = 400$ s is shown. Clearly, the largest pressure is observed near the co-rotating vortex pair. The overall pressure peaks decrease, away from the vortex pair. This is also visualized in Figure 6.3(a), together with the numerical result of different meshes. The numerical results were extracted using a moving average, which filters signals below 50 Hz. This figure shows a comparison of the acoustic pressure decay along the x-axis between the analytical and the numerical results. Overall, the acoustic field predication is confirmed by the analytical solution, especially at dense mesh. The coarse mesh has an somewhat over-predicted acoustic pressure level and shows a small numerical dispersion in the waves reaching the acoustic boundary. Using this mesh study, the absolute error is found (see Figure 6.3(b)). The order of accuracy is approximately one.

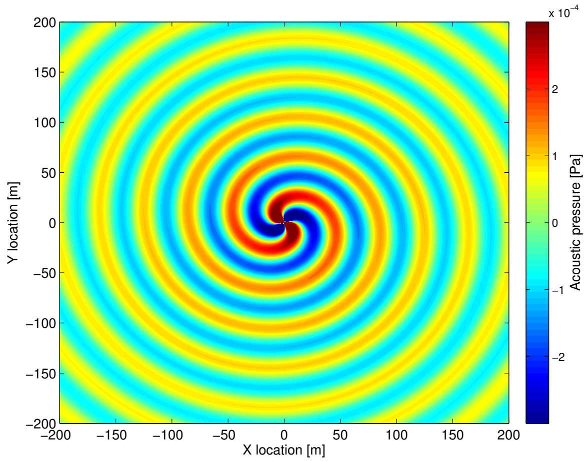

**Figure 6.2:** Pressure field of co-rotating vortex pair at t = 400 s

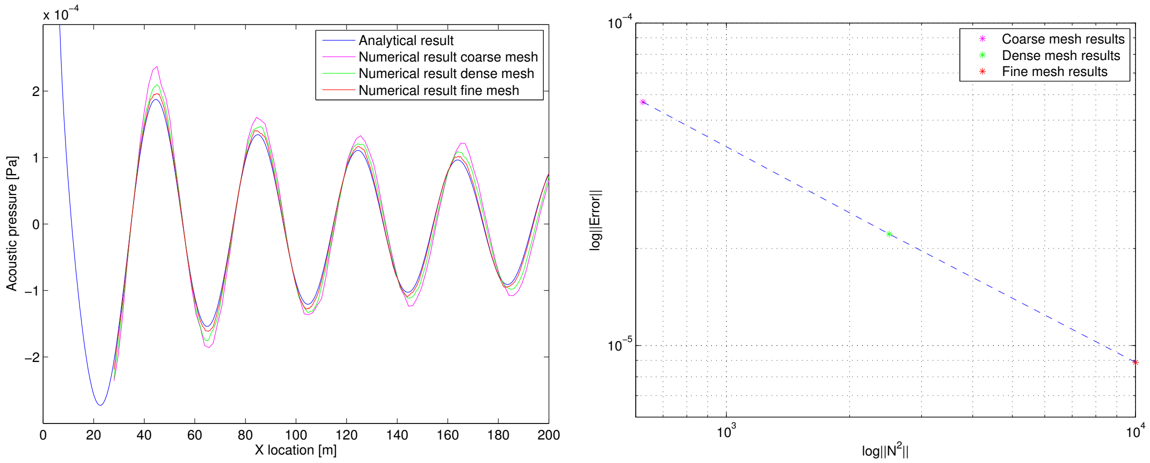

(a) Decay of the acoustic pressure values of the co-rotating vortex pair along the x-axis Pressure field of co-rotating vortex pair at t = 400 s

(b) Absolute error versus mesh results

**Figure 6.3:** Validation of the quadrupole source term using co-rotating vortices

## 6.2 Dipole source term

In this section, the dipole source term will be validated. As can been seen from Section 4.5.3, the implementation of the dipole source term is straightforward, only involving surface and volume fields. The following sections describe an analytical solution for the dipole source term, as well a simple simulation model in OpenFOAM®for verification.

### 6.2.1 Analytical solution

To validate the implementation in OpenFOAM®, first an analytical solution has to be found. As known from Section 4.1.2, a free field Green's function gives the approximate result of a non-homogeneous wave equation. Considering Equation (4.16), the most general solution of the non-homogeneous wave equation on a bounded domain is given by:

$$\rho' = \frac{1}{4\pi c_0^2}\int_V \frac{\partial^2 T_{ij}}{\partial y_i y_j}\frac{1}{|\mathbf{x}-\mathbf{y}|}dV(\mathbf{y}) + \frac{1}{4\pi}\int_S \left\{\frac{1}{r}\frac{\partial \rho}{\partial n} + \frac{1}{r^2}\frac{\partial r}{\partial n}\rho + \frac{1}{c_0 r}\frac{\partial r}{\partial n}\frac{\partial \rho}{\partial t}\right\} dS(\mathbf{y}). \tag{6.5}$$

In Equation (6.5), all the partial derivatives are evaluated at the retarded time, i.e. $t - \frac{r}{c_0}$. Here, $r = |\mathbf{x} - \mathbf{y}|$, where $\mathbf{x}$ is the location of the observer and $\mathbf{y}$ is the location of the sound source. The first integral is taken over the volume (containing the quadrupole sources) whereas the second integral contains the surface (dipole) source term. Equation (6.5) is rewritten by Curle (1955) in the following form:

$$\rho'(\mathbf{x},t) = \frac{1}{4\pi c_0^2}\frac{\partial^2}{\partial y_i y_j}\int_V \frac{T_{ij}}{r}dV(\mathbf{y}) - \frac{1}{4\pi c_0^2}\frac{\partial}{\partial x_i}\int_S \frac{n_j(p\delta_{ij} - \tau_{ij})}{r}dS(\mathbf{y}). \tag{6.6}$$

This solution is derived via a free-space Green's function $G$ and other mathematical operations. More information is presented in the paper by Curle (1955). When computing the solution of Curle analytically, it is favorable to transform the spatial derivatives into temporal ones. By applying the chain rule, making use of Equation (4.3) and assuming a non-moving body (surface velocity is zero), a compact form of Curle's analogy can be derived, only valid for a far field expression:

$$p'(\mathbf{x},t) \cong \frac{x_i x_j}{4\pi r^3 c_0^2}\int_V \frac{\partial^2}{\partial t^2}T_{ij}dV(\mathbf{y}) - \frac{x_j}{4\pi r^2 c_0}\int_S \frac{\partial}{\partial t}p n_i dS. \tag{6.7}$$

Since, in this validation only the dipole sources are considered, the first integral can be discarded. Besides, the time integral may be taken out of the spatial integration so that it reduces to a time-derivative of the surface integral of pressure:

$$p'(\mathbf{x},t) \cong -\frac{l_i}{4\pi c_0 r}\frac{\partial}{\partial t}\int_S n_j p \delta_{ij} dS(\mathbf{y}), \tag{6.8}$$

where $l_i = \frac{x_i - y_i}{r}$ is the unit vector directed from the source point $\mathbf{y}$ to the listener $\mathbf{x}$. The integral term can be interpreted as the total force exerted by the fluid on the body. Equation (6.8) is the analytical expression of the so called Gutin's principle for compact rigid bodies, which directly relates the force exerted by the fluid on the body to the radiated field in a far field approximation. In a two dimensional field, the $z$-integral vanishes and the amplitude of Green's function, based on the surface of the sphere ($4\pi r^2$) is interchanged for the surface of a circle ($2\pi r^2$) (You et al. (1998)).

### 6.2.2 Test domain and boundary pressure conditions

Now that the analytical solution is known, the implementation in OpenFOAM®can be verified. Since it is difficult to test the implementation with pressure fluctuations derived from an actual geometry (such as a diaphragm or an upper airway model), one can simply assume a known pressure function on a small rigid body to solve Equation (6.8) analytically. Therefore, the author proposes the following pressure function, which is dependent on time, but constant over the entire body:

$$p(\mathbf{x}, t) = 2000 \sin(700t) + 1500 \sin(700t) \cdot \cos(700t). \tag{6.9}$$

For this equation, an analytical solution can be easily found via Matlab®. For the numerical part of this analysis, an easy domain is required. Therefore, a free-field domain with a small solid boundary attached on the bottom is modeled in OpenFOAM®using the build-in `blockMesh` utility. The domain is illustrated in Figure 6.4(a), clearly stating the surface source location and the location of the far-field observer. A coarse, dense and fine mesh is used for solving the acoustic wave equation. In OpenFOAM®, a probe is placed at the observers location. The boundary of the domain is again modeled via a convective outlet boundary condition.

### 6.2.3 Results

A numerical simulation is run using OpenFOAM®to solve Curle's density equation (equation (4.16)), only containing dipole sources. Hence, a CFD simulation was not required, making the time-step only dependent on the acoustical Courant number. By using an time-step of $\Delta t = 1 \cdot 10^{-5}$, the acoustic Courant number stays under the required value of 1.0 for all individual meshes.

The resulting raw density field at $t = 0.05$ s is depicted in Figure 6.4(b), showing a fluctuating 'point-source' and a full motion period. This can be verified by comparing the period of the signal with the retarded time, i.e. $\frac{2\pi}{700} \approx 0.009$ s and $\frac{\sqrt{2^2+4^2}}{340} \approx 0.013$ s. The period of the fluctuating signal is smaller, making it possible to completely visualize the period in the domain.

From the microphone positioned at the observer location, the raw density data is extracted. Using a moving average, where using detrending signals below the 50 Hz are filtered, the fluctuating signal is retrieved. This fluctuating pressure can be compared with the analytical solution, which is retrieved by combining Equation (6.8) and (6.9). The result is plotted in Figure 6.5(a) for three different type of meshes.

A few interesting things can be derived from this figure. First of all, the overall resemblance of the numerical and analytical result is reasonably good. The result from the coarse mesh gives almost identical results as the pressure result from the fine mesh. Only one peak is overestimated, while another is underestimated. This error can be assigned to the detrending function required for correctly visualizing the perturbations. The numerically result in Figure 6.5(a) also indicates the retarded time, required to receive the signal at the probe. On

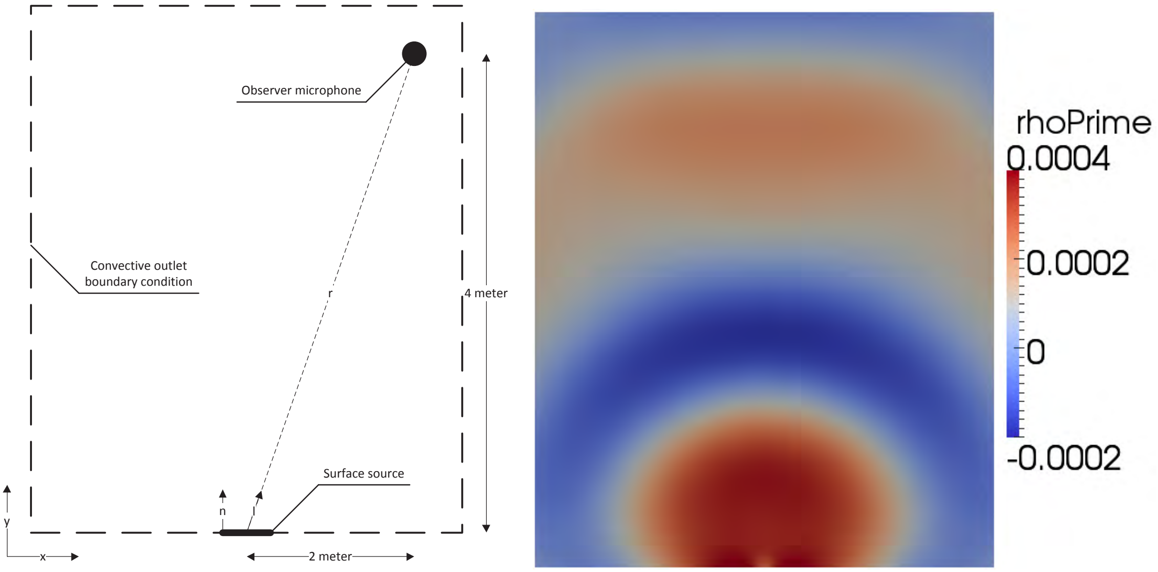

(a) Description of the domain

(b) Density field at $t = 0.05$ s of the domain

**Figure 6.4:** Domain modeled in OpenFOAM®for validating the dipole source term

the other hand, the analytical result is adapted to the retarded time in order to coincide with the numerical result.

By using a Fourier transform, the signal can be converted to a spectrum. The $SPL$ spectrum for the finest mesh is indicated in Figure 6.5(b). Again, overall a good resemblance is present between the analytical and numerical result. Both amplitudes of both peaks coincides, for the lower and higher frequencies. The higher frequency values are under-predicted in the numerical case. The first peak corresponds to the overall frequency of the analytical pressure function (i.e. $\frac{700}{2\pi} \approx 111$ Hz) while the second peak correspond to the period of the small oscillation inside the analytical pressure function, originating from the $(\sin(t) \cdot \cos(t))$ term in Equation (6.9).

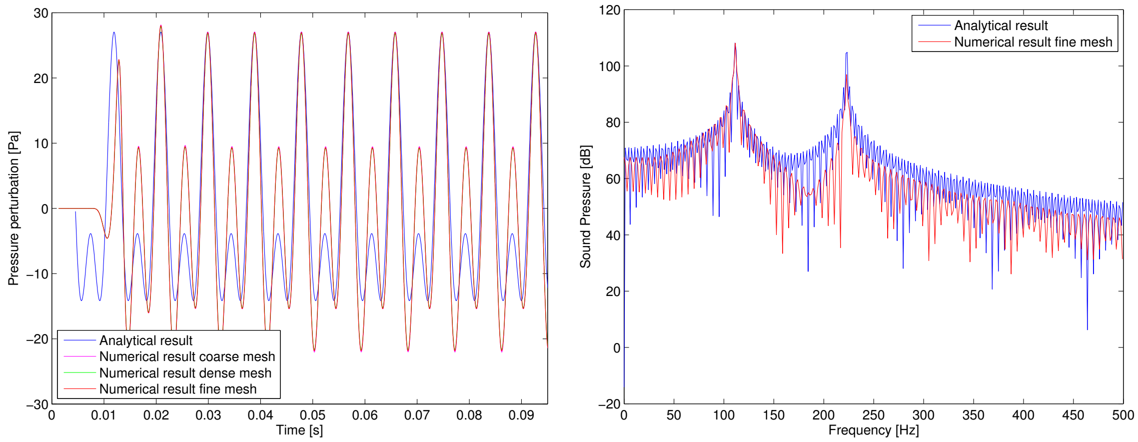

(a) Pressure perturbation versus time

(b) Sound Pressure Level versus frequency

**Figure 6.5:** Analytical and numerical result for the dipole verification model

## 6.3 Monopole source term

In a similar procedure as the dipole source validation, the monopole sources are evaluated. This section first introduces the analytical expression. Next both numerical models, the monopole source term and the fixed vibro-acoustic gradient condition, are compared with the analytical expression using the same model as used in the dipole source validation.

### 6.3.1 Analytical solution

To validate the implementation of the monopole source term (4.15), as well as the compatibility fixed vibro-acoustic gradient condition (5.11), first an analytical solution has to be found. Using the similar approach as presented in Section 6.2.1, including the free field Green's function, the analytical expression for the pressure perturbation from monopole sources is given by:

$$p'(\mathbf{x},t) \cong \frac{1}{4\pi r}\frac{\partial}{\partial t}\int_S \rho_0 v_n dS(\mathbf{y}), \tag{6.10}$$

where $v_n$ indicates the normal structural surface velocity. This expression is again rewritten in a two-dimensional format, similar as before.

The following analytical expression for the structural surface displacement is proposed, which can be implemented in previous formula.

$$\int v_n dt = \frac{1}{200}\left\{\cos^2(800t)\sin(800t) + \sin^2(600t)\right\}. \tag{6.11}$$

This displacement is set on the wall of the domain presented in Figure 6.4(a). Again, a convective outlet boundary condition for the boundary patches is chosen.

### 6.3.2 Results

A numerical simulation using OpenFOAM®, with a special solver able to solve the wave equation for monopole sources only (Equation (4.15)) and a solver able to handle the compatibility Equation (5.11) is used for validation and verification. No CFD simulation was run, making the time step dependent on the acoustical Courant number. The same time-step as in the dipole validation run was used. The resulting raw density field at $t = 0.5$ s is plotted in Figure 6.6. Multiple cycles can be observed in this snap-shot since the wavelength of the source term is smaller than the dimensions of the domain.

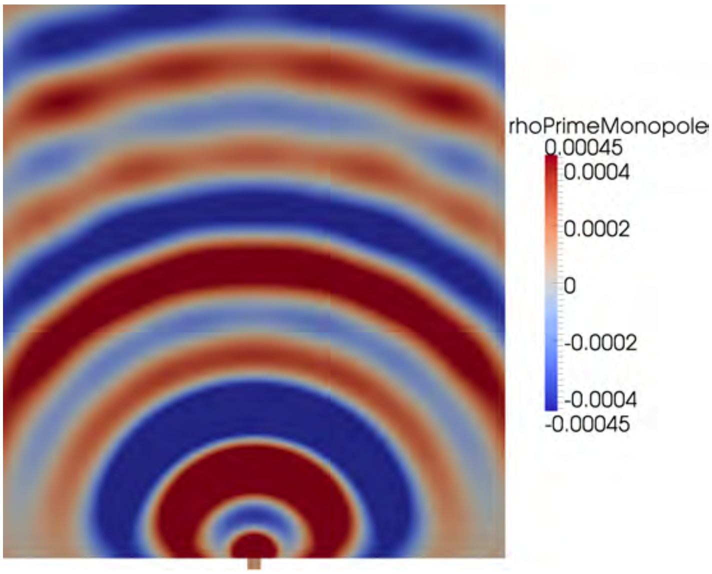

**Figure 6.6:** Density field at $t = 0.5$ s of the domain for the monopole validation

The pressure perturbation results, without detrending, are displayed for the monopole source term input as well as the vibro-acoustic compatibility input, in Figure 6.7(a) and Figure 6.7(b) respectively. A coarse, middle and fine mesh for the domain is used. Clearly, the numerical simulation of all meshes closely correspond to the analytical expression. The monopole source term result is almost identical to the results with the fixed vibro-acoustic gradient input. This verifies the correctness of both methods.

As a final check, the fine mesh Fourier transform results for the two methods are compared with the analytical results in Figure 6.8. Both methods, the monopole source term and fixed vibro-acoustic gradient input, are giving almost identical results and show good resemblance with the analytical solution. The three peaks are clarified by the three different wavelengths, appearing in the acceleration term of the structural boundary (the $\sin^3(800t)$, the $\cos^2(800t)\sin(800t)$ and the $\cos^2(600t)$ or $\sin^2(600t)$ term). The corresponding frequencies are respectively $\frac{3 \cdot 800}{2\pi} \approx 382$ Hz, $\frac{800}{2\pi} \approx 127$ Hz and $\frac{2 \cdot 600}{2\pi} \approx 191$ Hz.

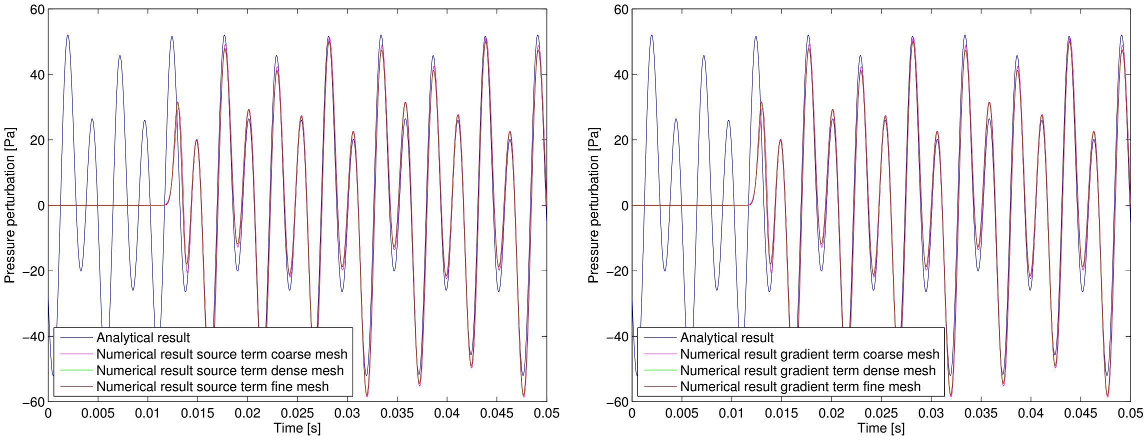

(a) Result for the monopole source term

(b) Result for the fixed vibro-acoustic gradient input

**Figure 6.7:** Pressure perturbation versus time for the monopole validation

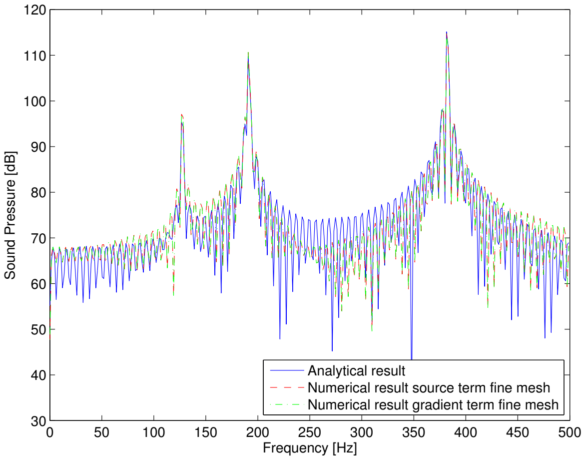

**Figure 6.8:** Sound Pressure Level versus frequency for the monopole source validation

## 6.4 Diaphragm

The diaphragm is a more realistic looking upper airway model, used for verifying the correctness of the implementation of the fluid, acoustic and structure. A diaphragm involves internal flow, which means that the acoustics are more restricted by means of reflections. This creates a complex acoustic field. Due to this complexity, it is useful to verify the result with a reference value. Three references are used, which do have the same model, as well as the same boundary and initial conditions. These are: Gloerfelt and Lafon (2007), Piellard and Bailly (2010) and Piellard and Bailly (2008).

### 6.4.1 Geometry

For the diaphragm a 2D and 3D fluid and structure model is created. The 2D model probably lacks accuracy (such as in-plane fluctuations and spreading of noise), but is useful to give a quick insight into both fluid, acoustic and structure properties. Also the 2D model is used to debug the OpenFOAM®solver. An overview of the fluid domain of the diaphragm is indicated in Figure 6.9. On the top and bottom of the diaphragm, a solid mesh is positioned with a thickness of 10 mm. The structure mesh is used for determining the monopole sources of the diaphragm model. The 2D fluid and structure mesh counts $1.39 \cdot 10^4$ and $2.75 \cdot 10^3$ cells respectively, while the 3D fluid and structure mesh counts $4.18 \cdot 10^5$ and $8.25 \cdot 10^4$ cells. Lynch (2012) already extensively discussed dense and coarse meshes for the diaphragm model, making it superfluous to do these tests again in this thesis. It is further interesting to mention that the reference papers did use a denser mesh, as well as a higher order CFD scheme. This probably influence the results.

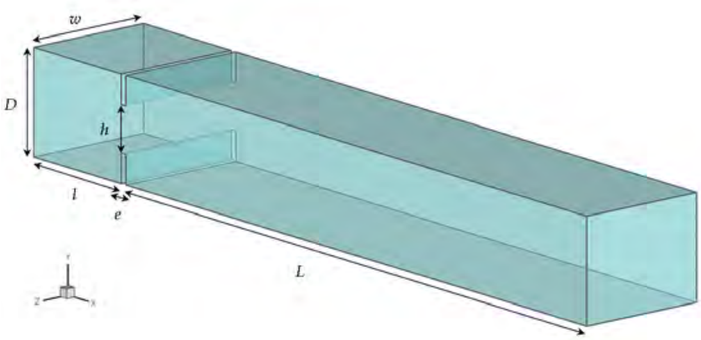

**Figure 6.9:** Diaphragm geometry, Piellard and Bailly (2008), where $w = 100$ mm, $D = 80$ mm, $h = 35$ mm, $l = 95$ mm, $e = 5$ mm and $L = 500$ mm. The $x$-axis indicates the streamwise flow direction; the $y$- and $z$-axis respectively indicate the transverse and spanwise directions.

### 6.4.2 Boundary and initial conditions

The boundary and initial conditions are set, such that they are similar to the reference data. The inlet flow can be assumed to be uniform, with a velocity vector of 6 m/s in $x$-direction. At the outlet, the pressure was set to 0 Nm/kg, which is possible due to the incompressibility of the model. The velocity has a zero gradient condition at the outlet, which corresponds to a von Neumann boundary condition. For the acoustic part, the condition for the density perturbation at the inlet and outlet was set as a convective outlet boundary condition, introduced in Chapter 4. At the walls the pressure and density are determined using a von Neumann boundary condition, while for the velocity a no-slip condition is used.

The structural mesh only consists of two boundary conditions. At the interface, there is a traction boundary condition, which interpolates the pressure data from the fluid to the structure mesh. All other boundaries are fixed, i.e. no structural displacement is allowed.

### 6.4.3 CFD results

To verify the correctness of the CFD results, the qualitative results from Gloerfelt and Lafon (2007) are used. Since the diaphragm is symmetric, one may assume that the flow also shows a symmetric pattern. However, from the results will follow that this is not the case, making it an interesting test case. In Figure 6.10, a snapshot of the instananeous velocity profile in $x$ direction is shown. The results for the $y$ and $z$ velocity are plotted in Figure 6.11 and Figure 6.12. In all cases, for comparison, the results from Gloerfelt and Lafon (2007) are attached. From a first observation, clearly all specific flow patterns are similar. The result from Gloerfelt and Lafon (2007) logically shows more details due to the very fine mesh compared with the diaphragm model. In case of the longitudinal velocity, the flow attaches to the wall. This is the so called 'Coandă' effect. The attachment point is similar, however from the diaphragm a much finer jet (the jet is mixed into the uniform flow a bit sooner) is observed. Another difference is, that after the attachment point, the jet in the reference plot separates from the wall again. This latter observation is not clearly visible in the diaphragm results. Here, the jet reattaches and stays at the wall. This might be because of the improved wall treatment.

Please note that these images are instantaneous plots of the velocity. Hence, due to the turbulent behavior, the velocity profiles will vary per plot. For the crossflow and spanwise velocity, clearly the fine mesh from Gloerfelt and Lafon (2007) shows much more structures. However, the same maximum and minimum values are reached in both plots, making the diaphragm results accurate enough.

Another interesting property to analyze is the vorticity modulus. The shedding of the two large vortices, due to the diaphragm, are plotted in Figure 6.13, together with the reference result from Gloerfelt and Lafon (2007). Again, the results lacks some detail due to the coarser mesh. The overall features are however still comparable, for example the point at which the center of the jet begins to show vorticity and the location where the vorticity breaks down.

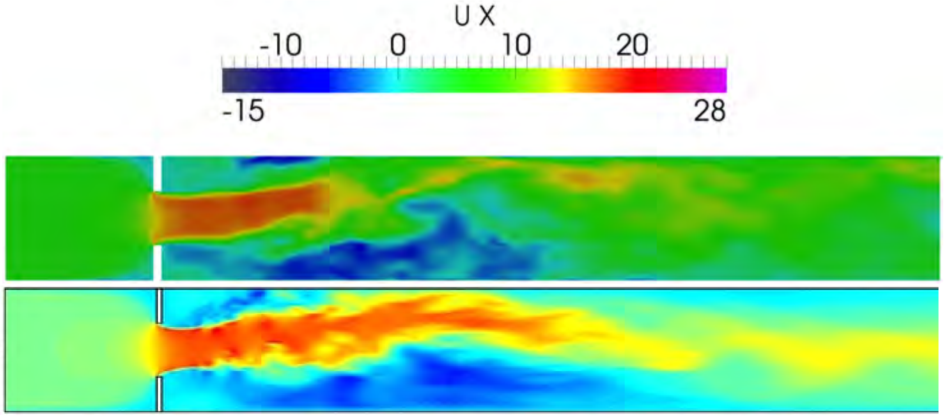

**Figure 6.10:** Snapshot of the instantaneous longitudinal velocity $u$ from the diaphragm model (top) and from Gloerfelt and Lafon (2007) (bottom)

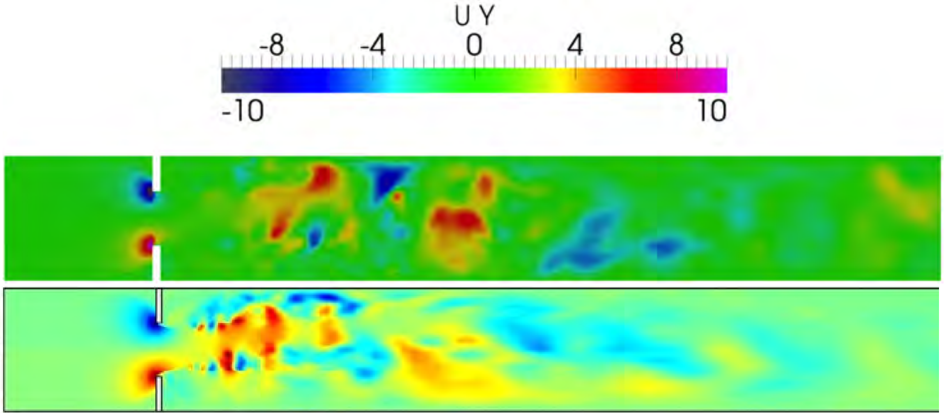

**Figure 6.11:** Snapshot of the instantaneous crossflow velocity $v$ from the diaphragm model (top) and from Gloerfelt and Lafon (2007) (bottom)

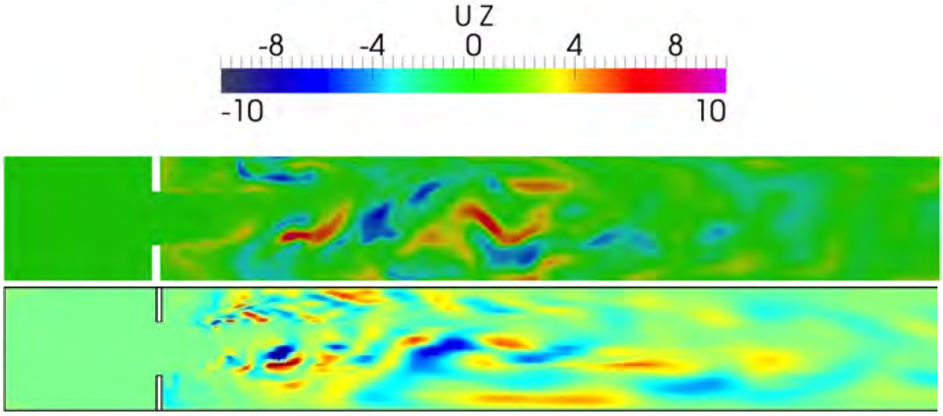

**Figure 6.12:** Snapshot of the instantaneous spanwise velocity $w$ from the diaphragm model (top) and from Gloerfelt and Lafon (2007) (bottom)

Since vorticity is closely related to quadrupole sources, it can be assumed that the fluid flow equations are accurate enough to predict the three acoustic source terms. The source terms will be discussed in the next section.

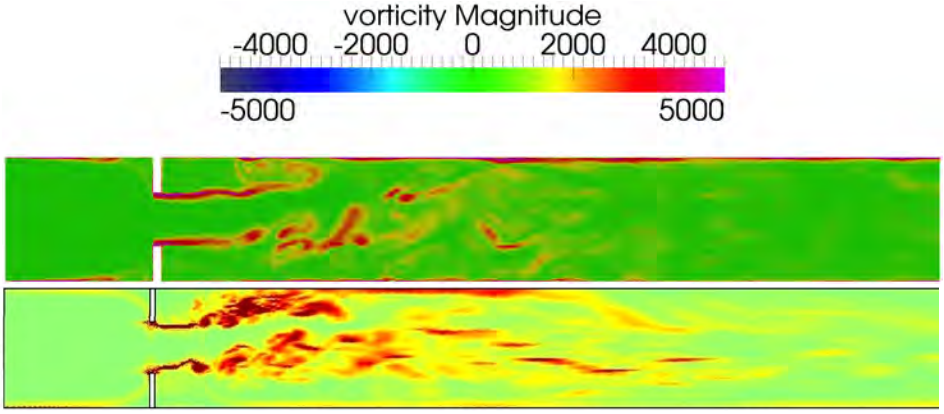

**Figure 6.13:** Snapshot of the vorticity modulus $\|\omega\|$ from the diaphragm model (top) and from Gloerfelt and Lafon (2007) (bottom)

A last interesting note is the result of the investigation into the differences between the 2D and 3D model. Therefore, in Figure 6.14 and Figure 6.15, the crossflow velocity and velocity magnitude is respectively plotted for the 2D and 3D case. The 2D case clearly shows a large difference with respect to the 3D case. The jet is not disappearing, and continuously bouncing on both walls. Also, the cross-flow velocity at the 2D case is much larger. Probably, the two-dimensional model is not representative for a visualizing a correct diaphragm flow.

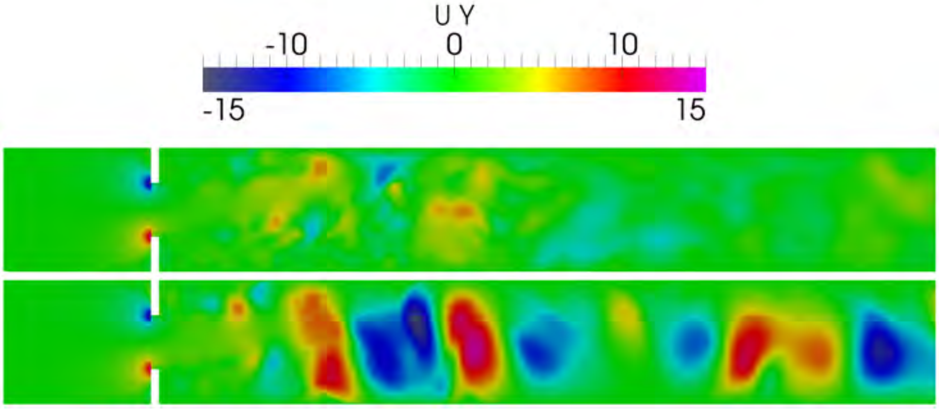

**Figure 6.14:** Snapshot of the instantaneous crossflow velocity u from the 3D diaphragm model (top) and from the 2D diaphragm model (bottom)

### 6.4.4 Acoustic results

The three acoustic sources, derived in Chapter 4, are used on the right hand side of the wave equation in order to generate an acoustic field in the diaphragm model. The raw signal is

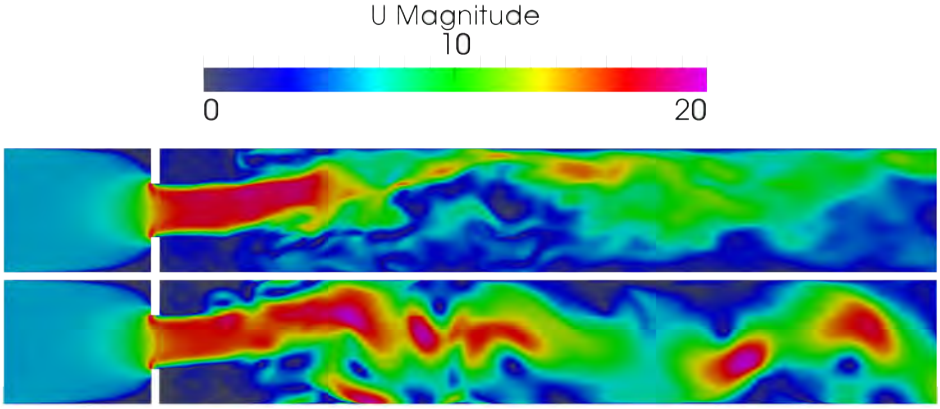

**Figure 6.15:** Snapshot of the instantaneous velocity magnitude u from the 3D diaphragm model (top) and from the 2D diaphragm model (bottom)

captured via a probe at the outlet and converted by a moving average scheme in Matlab®, using detrending with a cut-off frequency of 50 Hz. By subtraction, only the resulting fluctuating signal is retrieved. Also, in most simulations, the start-up of the simulation is clipped in order to capture the correct signal.

### Outlet probe results

The raw signal from the wave equation with monopole, dipole and quadrupole (and a combination of) sources for the diaphragm model is depicted in Figure 6.16(a), while the resulting pressure fluctuations are plotted in Figure 6.16(b). Here one can see clearly the difference in amplitude of the different sources. In general the Lighthill sources are having a large amplitude and low frequency spectrum, while the dipole and monopole sources are having a low amplitude and high frequency perturbation wave. And especially a combination of those three sources, the FW-H results, shows a large amplitude with low frequency, together with a small amplitude with high frequency wave. This might give an indication of a high sound pressure.

Using the pressure fluctuations, a sound spectrum can be calculated. Gloerfelt and Lafon (2007) also determined the sound spectrum. The result from this paper is extracted and plotted together with all the results from the acoustic wave equations. The overall spectrum, obtained from the Fourier transform function from Matlab®is plotted in Figure 6.17(a), while a zoomed spectrum can be found in Figure 6.17(b).

A first general observation is that all the different sources show a similar pattern in all parts of the frequency spectrum. Each single sound source (monopole, dipole and quadrupole) have different, but sometimes corresponding frequency peaks. These peaks can correspond to various things, such as the reflection of waves inside the domain (in the x, y and z-axis) or the vibration frequency of tissue. When taking a look at the zoomed spectrum, the sources can be compared with the reference source from Gloerfelt and Lafon (2007). The quadrupole sources (yellow line, almost completely positioned behind the magenta line) show an over prediction of sound pressure in the low frequency field whereas the dipole sources (green line) show a better

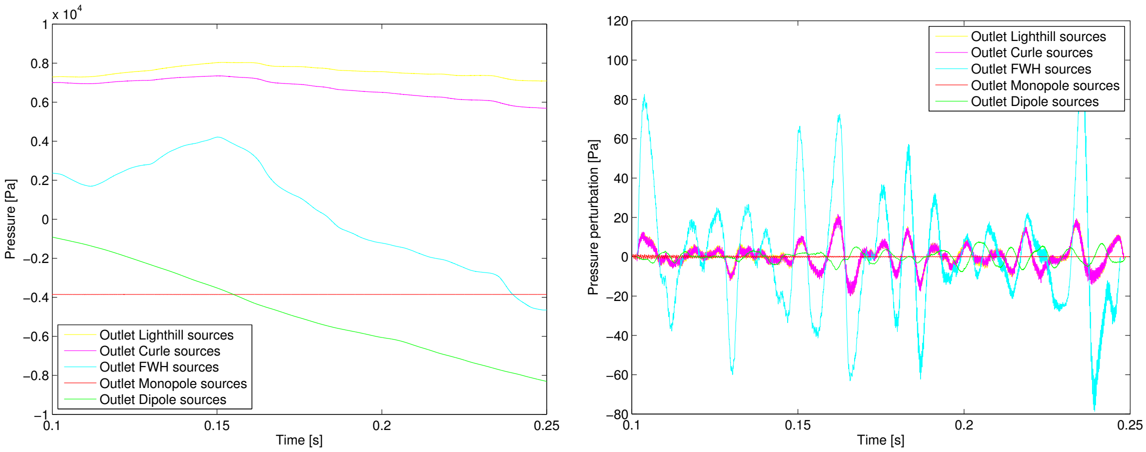

(a) Raw pressure data

(b) Resulting pressure perturbation data

**Figure 6.16:** Acoustic pressure results versus time from the outlet probe of the 3D diaphragm model

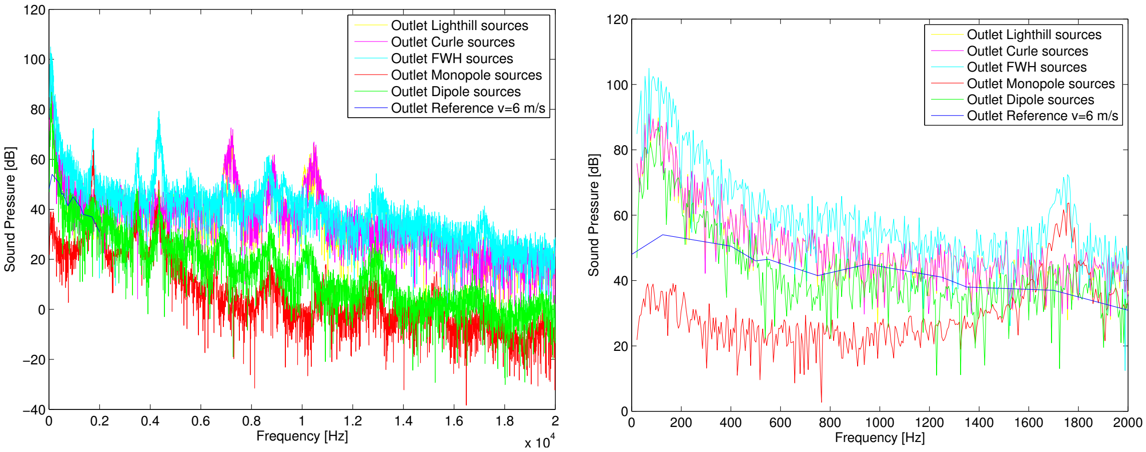

(a) Overall sound pressure data

(b) Zoomed sound pressure data

**Figure 6.17:** Acoustic sound pressure results versus frequency from the outlet probe of the 3D diaphragm model

correspondence with the reference values. A combination of both (Curle analogy, magenta line) also show a over prediction, making the quadrupole sources the dominant term. Te cyan line (FW-H analogy) even shows a larger over-prediction of sound level. Unfortunately, the monopole sources cannot be compared with any reference values, since no reference model exist for this acoustic source. However, pure qualitatively, the monopole sources have a small contribution between 0 and 1000 Hz and a more dominant contribution at the higher frequencies. Overall, it does not really affect the total SPL (see FW-H line).

### Quadrupole term analysis

Now that the general results are discussed, it is useful to go deeper into the results from above. As mentioned, the quadrupole sources are over predicted with respect to the results from Gloerfelt and Lafon (2007). First, this can be due to the fact that the larger turbulent structures are not broken up into smaller sources resulting in a increase of energy to the smaller frequencies. On the other hand, the quadrupole source term is based on large sinks and sources. If the model is not long enough, which might be the case in this current issue, not all the turbulent structures and therefore not all the sinks and sources of the quadrupole source term are captured. The end of the domain could be set at a intersection of a source and sink couple. If the corresponding sink is outside the domain, the sound pressure will be over-predicted. Therefore, it is interesting again to look at the vorticity plot in Figure 6.13, since the quadrupole source term is directly related to the vorticity (see Chapter 4. One can clearly distinguish some high vorticity area's near the end of the domain (see for example the upper right corner). This implies turbulence at the outlet of the domain. To completely damp out these effects, an infinite domain should be chosen. Other options are adapting the viscosity of the fluid or the cell volumes at the end of the domain, to partly damp out these effects. In this thesis, there is chosen to compare the standard model with an extended model with large volume cells at the outlet. The model is extended with 100 mm and 4 cells in x-direction. The resulting pressure perturbation and zoomed sound pressure spectrum is illustrated in Figure 6.18(a) and Figure 6.18(b). No clear difference can be found between both models. Still, each model shows an over prediction of quadrupole sources. Hence, further research into this subject is required to avoid the over-prediction of the SPL.

### Monopole term analysis

Another interesting sound source to further discuss is the monopole source, generated from the moving structure around the diaphragm. In previous plots, the mechanical properties of the structure were set by conservative values from human tissue. To understand the importance of setting correct mechanical properties, the two most extreme tissue properties are chosen from Table 5.1. This results in a monopole source term for firm and soft tissue. Results are plotted in Figure 6.19(a) and Figure 6.19(b). Clearly, soft tissue is a better source for sound. The acceleration term in soft tissue is much larger, and therefore more susceptible for large pressure perturbations. The sound spectrum also clearly shows an increase of 17 dB between the firm and soft tissue results. It can be concluded that is very important to use the correct mechanical properties for the structural mesh, since large deviations can occur between different acoustic results.

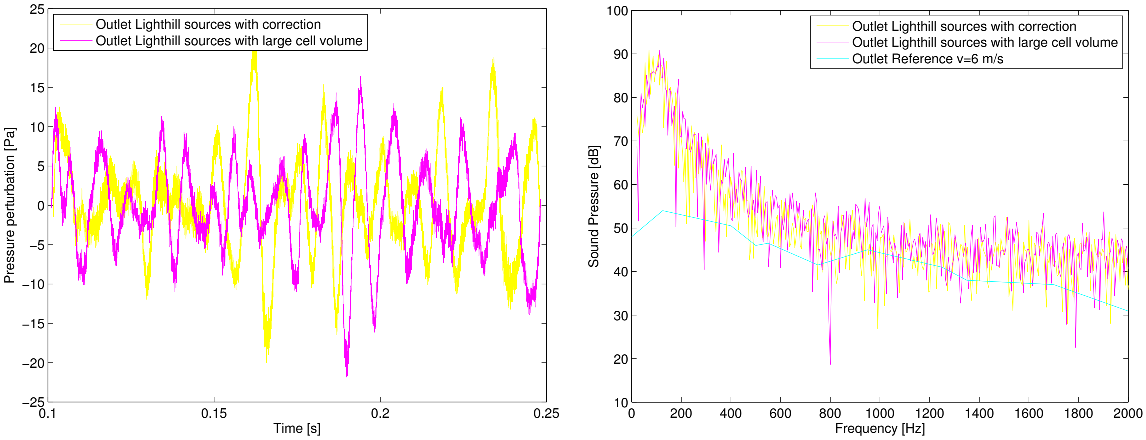

(a) Resulting pressure perturbation data (b) Zoomed sound pressure data

**Figure 6.18:** Quadrupole sources results from the outlet probe of the standard and extended 3D diaphragm model

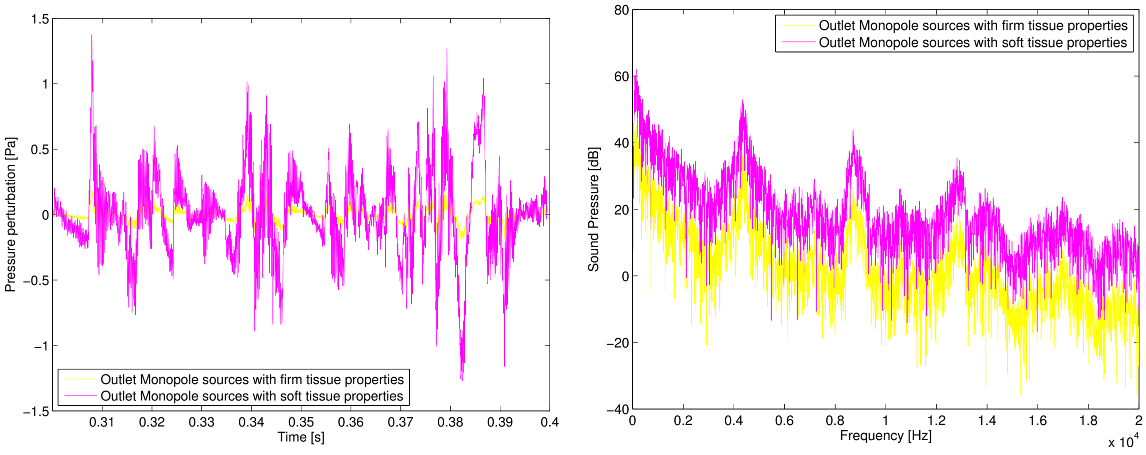

(a) Resulting pressure perturbation data (b) Overall sound pressure data

**Figure 6.19:** Monopole sources results from the outlet probe of the firm and soft tissue model around the 3D diaphragm model

### Two-dimensional diaphragm analysis

The 2D acoustic results are not discussed in this section, since the result from previous section showed that the CFD results were not accurate enough. Since the acoustic results are coupled with the CFD results, it is not useful to discuss any 2D acoustic results. However, the model was found useful for verifying the correct implementation of boundary and initial conditions in OpenFOAM®. With this model, also the implementation of a impedance boundary condition (as discussed in Section 4.5.5) is tested by Lynch (2012). Using the impedance value of the human tissue, the impedance boundary condition was compared with a zero gradient boundary condition. The use of an impedance condition hardly affected the results. Only a difference of ±0.5 dB was observed. Therefore, this boundary condition is removed from any further simulations in this thesis.

# Chapter 7

# Analysis of a simplified upper airway model

Now that the three acoustic sources are validated, it is time to deal with the geometry of an upper airway. For this, a simplified upper airway model (SUAM) is used. The model, already introduced in Section 2.1.7 can be used to give some insight into the flow conditions, as well as in the mesh density that is required to capture all the important flow phenomena. The model is derived from real airway geometries and shows the same type of flow structures that are encountered in a real airway. The model has been used in literature for a Large Eddy Simulation (LES) simulation (Jayaraju et al. (2008)) but is also used in a Particle Image Velocimetry (PIV) experiment (Brouns et al. (2006)). The verification of the solver with respect to the SubGrid-Scale (SGS) model has already been performed by Lynch (2012) and will therefore not be repeated here. However, the CFD and acoustic results will be discussed and compared to investigate the effects of a constriction in the flow.

## 7.1 Geometry

The geometry of the SUAM model is already discussed in Section 2.1.7 and schematically displayed in Figure 2.7. For the sake of completeness, a 3D model of one the models is added in Figure 7.1. There are three different models, each with another level of constriction. First, there is a model without any constriction. Next, there are models with 50 % and 75 % constriction. The air flows in at the top of the model through the inlet which makes a transition to the oral cavity. From here, the flow needs to bent 180° to the nasopharynx. Next a sharp edge can be seen. This is normally the place where the epiglottis would be in a real human airway. Further downwards the area reduces as the air flows through the glottis, and widens again when transitioning to the trachea.

The reason for choosing a 50 % and 75 % constriction model is that a doctor can start diagnose tracheal stridor from about 50 %, while at 75 %, the patient will have severe breathing problems and further medical assistance is required. All constrictions are cylindrical in the

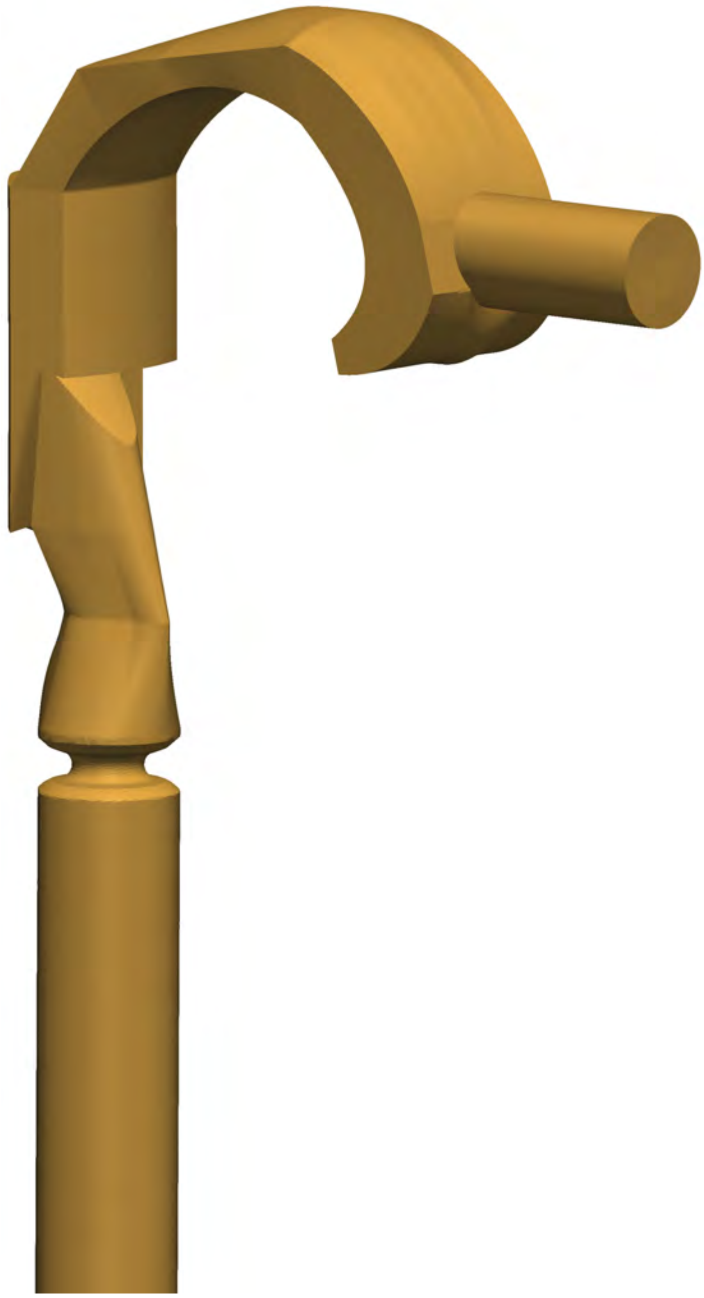

**Figure 7.1:** Three dimensional overview of the $75$ % constricted SUAM

SUAM and in a real airway this can be present due to, for example, scar tissue. With these models, it is possible to investigate the sound production relations with respect to the constriction size.

Since the CFD model, as well as the mesh of the SUAM is already verified by Lynch (2012), only one fine mesh is used. The mesh counts approximately $2.52 \cdot 10^6$ cells for all models. The SUAM model is run without structural model. The reason will become clear in further sections.

## 7.2 Boundary and initial conditions

The boundary conditions used in the upper airway are slightly different compared to the validation method from previous chapter. The inflow of an airway does not need to be uniform whereas the outflow should be more or less uniform. Therefore, the inlet and outlet conditions are changed with respect to the diaphragm model. A pressure-pressure boundary condition is not very useful, since the required pressure difference is not known beforehand. This condition would require many iterations, which is inconvenient given the approximate time of one month for a complete simulation. At the inlet a uniform differential pressure is set and the velocity is determined automatically by the pressure difference. This creates a non-uniform flow, which might result in a better inflow of air. At the outlet the pressure has a von Neumann condition and the velocity is imposed such that the correct mass flow is achieved. A flow rate of 30 L/min is used, which is extracted from Brouns et al. (2006).

For the acoustics, an convective outflow boundary is used, even for selected regions near the inlet and outlet. This allows waves that are non parallel to the inlet and outlet also to leave the domain. Further more, near the inlet and outlet, the quadrupole (volume) source term is set to zero to avoid numerical noise caused by the boundary conditions of the inlet and outlet. Smoothing is applied at the inlet, to counteract the large velocity peaks originating from the non-uniform inflow.

## 7.3 CFD results

To gain some insight into the flow characteristics of the simplified upper airway model, it is useful to start looking at stream line vectors. The velocity vectors are plotted for all three models in Figure 7.2. The color map is based on the magnitude of the velocity. As can been seen, the flow enters the model smoothly. Some vortices are created at the entrance due to the increased cross sectional area at the end of the tube. Also below the inlet, a region of circulating flow is present. Further, after the flow bends 180° and hits the epiglottis (sharp edge), the flow seems to become turbulent. Next, the flow is accelerated due to the decrease in cross-section, smoothing the streamlines. Below the glottis the flow attaches to the anterior (right) wall. On the other side, a recirculation zone is present. After this point, the three different constriction models vary in the level of turbulence as can been seen from the colored arrows. Increasing the constriction size, increases the mixing, the size of the recirculation zone before the constriction but also the jet attachment point.

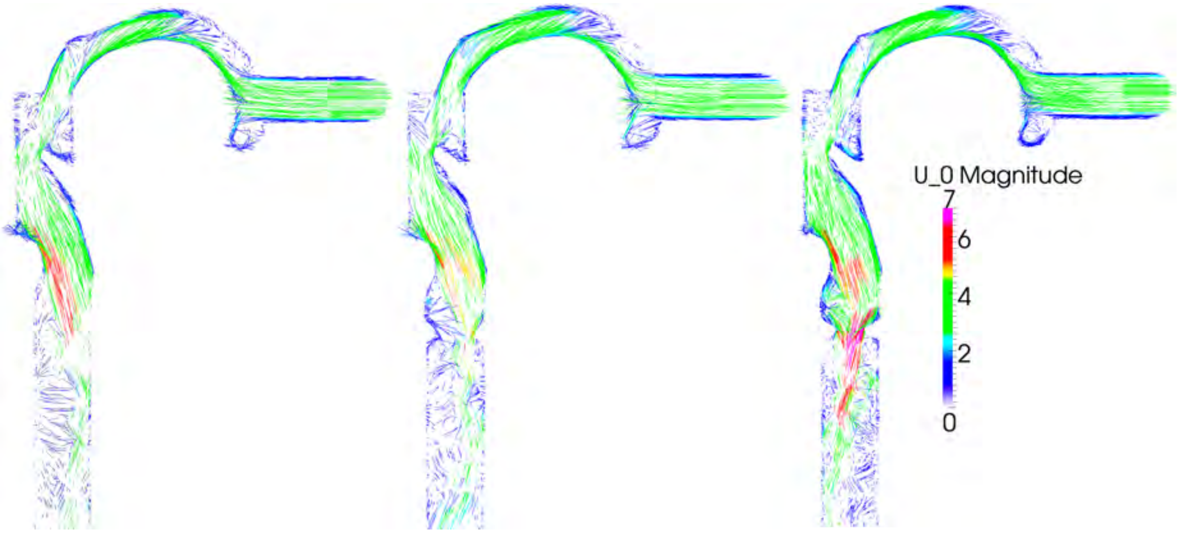

**Figure 7.2:** Snapshot of streamlines for the original (left), 50 % constriction (middle) and 75 % constriction (right) SUAM

To further investigate the mixing and the recirculation zone after the constriction, the velocity in vertical direction is plotted in Figure 7.3. As a first observation, all three models shows a similar velocity field with similar minimum and maximum values in the area above the epiglottis. Hence, the constriction itself will hardly influence the flow above in the model. Below the constriction, indeed the size of the circulation zones vary. The back flow and jet velocity are increasing with increasing constriction size. Different zones are present in the 75 % constriction model. However keep in mind that the flow is three dimensional and that Figure 7.3 is a two dimensional slice of the model. Not everything can be shown in this plot. Also, when comparing the jets from the 50 % and 75 % case, the jet location is different. With 75 % constriction, the jet comes off the wall and divert to the opposite side of the trachea, the posterior side, while in the 50 % constriction case the jet attaches to the anterior side.

Also the magnitude of the flow inside the SUAM is plotted. The results of the three models are shown in Figure 7.4. Again above the epiglottis, no clear differences can be found. Below, near the constriction ,the 0 % and 50 % case do also not vary much. Approximately the same minimum and maximum are reached. However, the 75 % case shows a velocity magnitude which is 2× larger compared with both other models. Also, the jet is decreasing in length due to faster mixing with the surroundings. Due to redirection of the jet to the middle (in case of constriction), more mixing is possible and the large stresses near the wall thereby reducing the jet length.

Now that the velocity is discussed, the vorticity should be discussed. This will give more insight into the three dimensionality of the flow. As can be seen from Figure 7.5, the 50 % constriction model has more vorticity compared with the model without constriction. The

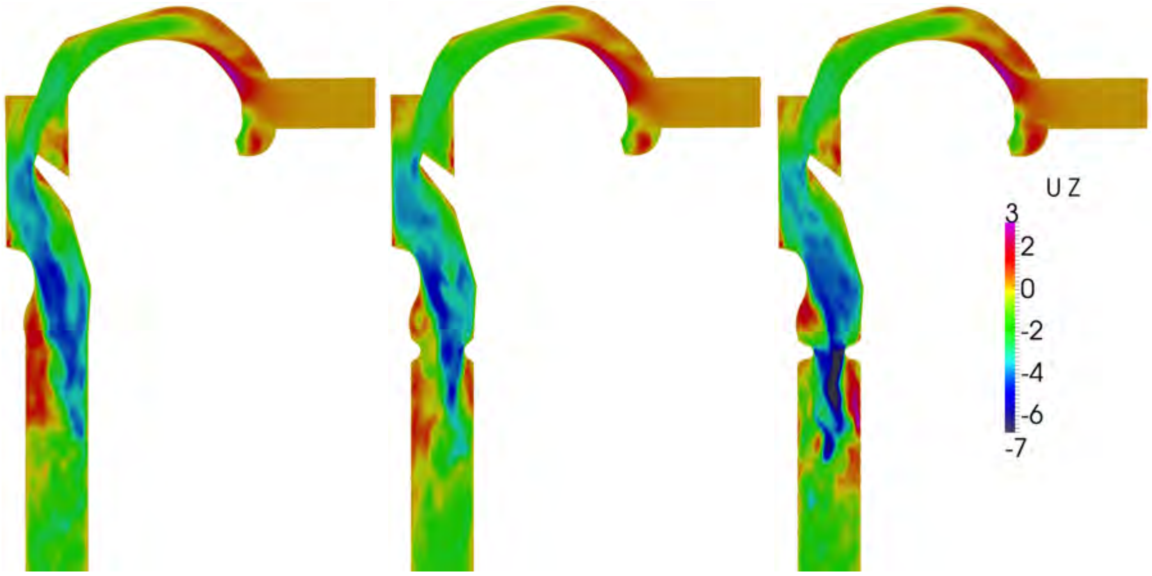

**Figure 7.3:** Snapshot of the instantaneous velocity in vertical direction for the original (left), 50 % constriction (middle) and 75 % constriction (right) SUAM

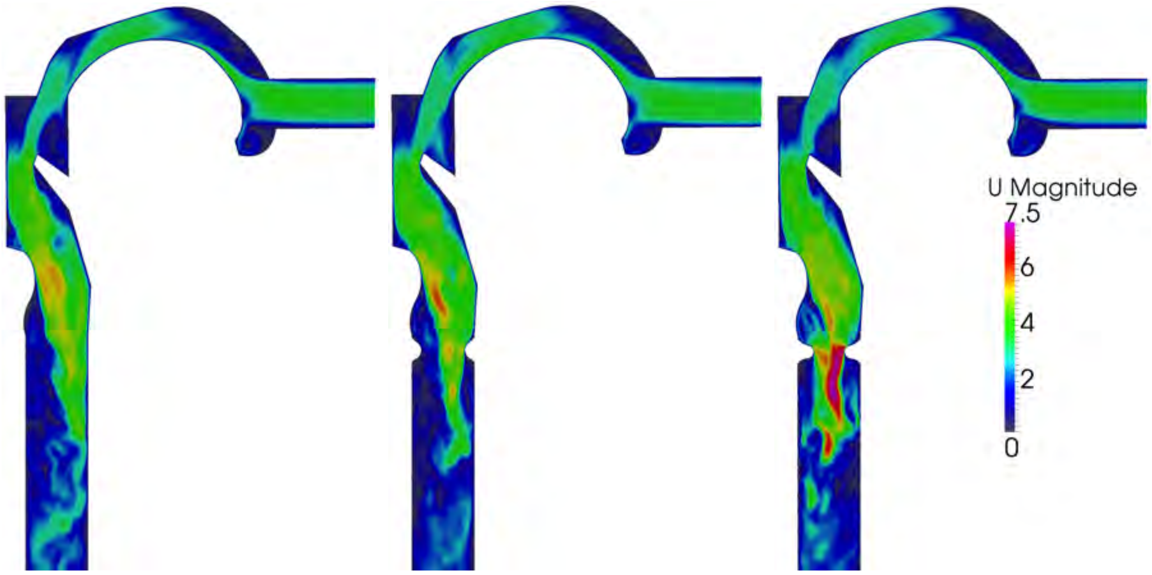

**Figure 7.4:** Snapshot of the instantaneous velocity magnitude for the original (left), 50 % constriction (middle) and 75 % constriction (right) SUAM

level of vorticity is however approximately the same. For the extreme constricted model, both the mixing and strength are increased. The vorticity is also spread over a larger area (more downstream), indicating a larger area with turbulent flow. The vorticity result is linked to the quadrupole volume source term, making a higher sound pressure more likely in a more constricted area. These results are presented in the next section.

**Figure 7.5:** Snapshot of the vorticity modulus $\|\omega\|$ for the original (left), 50 % constriction (middle) and 75 % constriction (right) SUAM

The last interesting parameter to discuss is the pressure (Figure 7.6). The pressure drop (normalized with the density in OpenFOAM®) for the original model is approximately 10 Nm/kg, for the 50 % constriction model approximately 15 Nm/kg and for the 50 % constriction model this increases to approximately 30 Nm/kg. Thus, the area reduction between the normal and 50 % case is less influencing the pressure compared with the area reduction from 50 % to 75 %. A person with 75 % obstruction will thus experience breathing problems. The contraction of the intercostal muscles should be much larger, to generate a larger under pressure in the lungs, for the same amount of air.

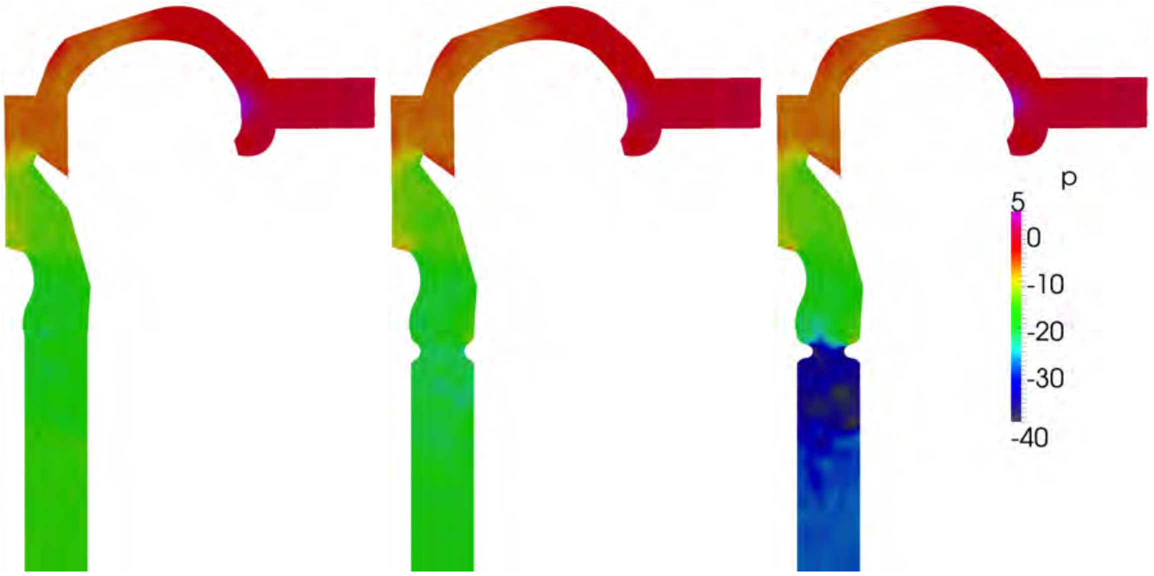

**Figure 7.6:** Snapshot of the pressure for the original (left), 50 % constriction (middle) and 75 % constriction (right) SUAM

## 7.4 Acoustic results

For the acoustic results, some fluid quantities are required. To avoid any interpolation, the acoustic mesh is similar to the fluid mesh. First, a qualitative analysis of both quadrupole and dipole source are discussed. The monopole source data is unavailable, since the structural mesh is discarded in this model. The section continues with discussing probe results from the inlet and outlet of the model and the results are compared with respect to percentage of obstruction.

### 7.4.1 Qualitative analysis

Lighthill's analogy consists of quadrupole sources, derived from the velocity volume field. A snapshot of the result of the quadrupole term is plotted in Figure 7.7. The three different constrictions show a similar result above the epiglottis. Below, the mixing increases for increasing constriction size, and therefore the quadrupole source term shows larger sinks and sources (alternating blue and red areas). As expected, the magnitude of the sources also increases.

The dipole source term is derived from the fluid pressure at the boundary. Therefore, a three dimensional plot of the boundary is required to clearly visualize the dipole term. In Figure 7.8, the walls of the three different models are presented. It should be clear that, when increasing the constriction size, the larger the under pressure, the larger the dipole term is going to be. At 75 % of constriction, a significant increase in magnitude below the constriction can be found. Not only below the constriction the source term is very active, but

**Figure 7.7:** Snapshot of the quadrupole source term for the original (left), 50 % constriction (middle) and 75 % constriction (right) SUAM

also at the constriction itself the source term is active. This is different with for example, the quadrupole source term, which is only significant behind the constriction downstream, near the lungs.

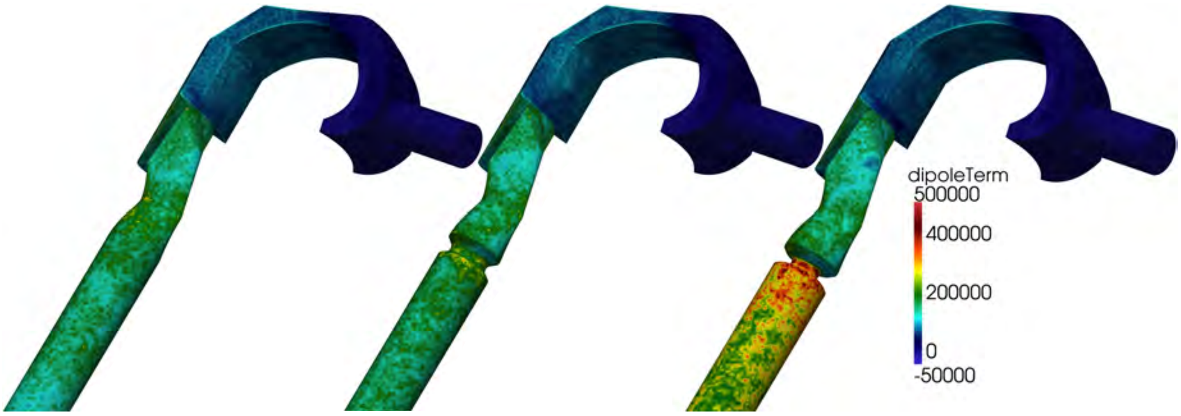

**Figure 7.8:** Snapshot of the dipole source term for the original (left), 50 % constriction (middle) and 75 % constriction (right) SUAM

### 7.4.2 Inlet probe results

Now that both source terms are qualitatively discussed, it is useful to investigate the acoustic field using inlet at outlet probes. First, observe the acoustic pressure results from the inlet probe. In Figure 7.9(a) and Figure 7.9(b), the pressure perturbation and Sound Pressure Level (SPL) spectrum is plotted. The pressure perturbations are derived from the raw pressure data, by an moving average filter of 50 Hz. During the simulation, the amplitude and frequency of all sources stays approximately the same, which is a requirement for comparing different sound spectra. Clearly, all quadrupole sources are dominant with respect to the dipole sources. This result is counter intuitive after the comparison of both source terms in Section 4.4. However, as already mentioned in previous chapter, it is likely that the quadrupole term is somewhat over-predicted. When looking at the sound spectrum, no distinctive peaks can be observed. The highest sound pressure is positioned at the lowest frequencies. The frequencies near the 20, 000 Hz are also increased for the 0 % and 75 % constriction case. This is possibly due to high frequency noise, to be discussed in next section.

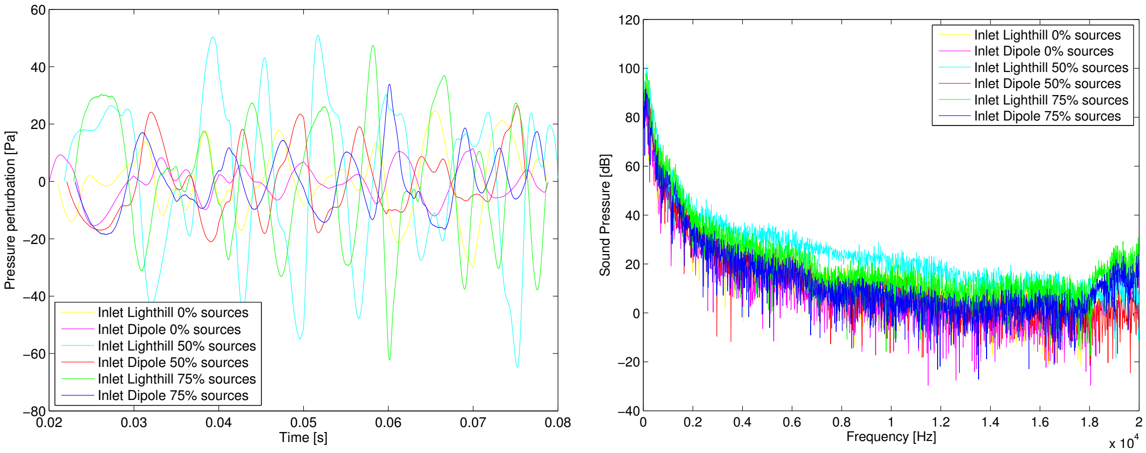

(a) Resulting pressure perturbation data versus time

(b) Overall sound pressure data versus frequency

**Figure 7.9:** Acoustic pressure results from the inlet probe of the SUAM

### 7.4.3 Outlet probe results

For the outlet probe similar results can be found for the pressure perturbations (Figure 7.10(a)) and sound pressure (Figure 7.10(b)). The major difference with the inlet results are the magnitudes of the perturbation and sound pressures. The amplitude of the perturbations are increased by a factor 1.7 while the sound pressure at higher frequencies is increased by approximately 20 dB. Another interesting observation is the enormous increase of sound pressure for frequencies near the 20, 000 Hz. Again, this could be assigned to high frequency noise. This is clearly visualized by the bolder green and blue lines (which is in fact a continuous fluctuating line) in Figure 7.10(a). To check if this is really noise, and not part of the acoustic spectrum, Figure 7.11 is plotted. Here, a small part of Figure 7.10(a) is plotted. Sharp peaks are observed around an average solution. This is a clear indication that the fluctuations are not wanted, and that they can be considered as a numerical error in the signal. A possible reason for this noise is the difference in fluid and acoustic time step, which is varying at around the order of $5.0 \cdot 10^{-5}$. During the sub-cycles of the acoustic part, the fluid results are fixed at a certain time-step. This leads to the same fluid quantities for each acoustic sub-cycle step and therefore to a large step in source term amplitude at the end of an old and start of a new sub-cycle. Overall, again no clear peaks are visible in the sound pressure spectrum besides the large sound pressure level near 0 Hz. It might be the case, that however this simplified model is accurate enough to visualize the correct flow field in an upper airway, it lacks accuracy for an accurate acoustic analysis. This is also the main reason to not implement a structure model in the simplified airway model. This time-consuming process can better be performed in a more realistic model. It is therefore much more important to also model and analyze a realistic model of an upper airway, and to compare it with clinical results. This analysis will be performed in the next chapter.

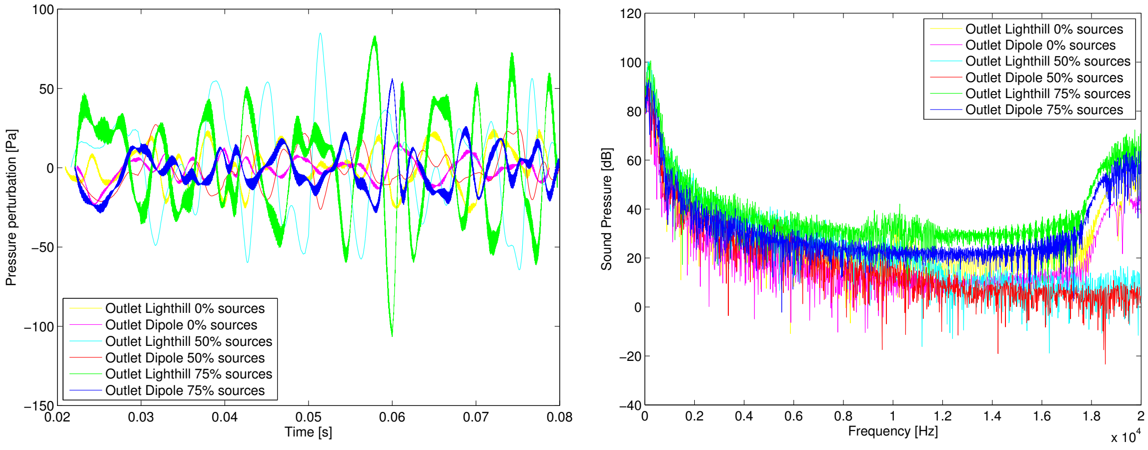

(a) Resulting pressure perturbation data versus time

(b) Overall sound pressure data versus frequency

**Figure 7.10:** Acoustic pressure results from the outlet probe of the SUAM

### 7.4.4 Comparison between inlet and outlet

To compare the results at the inlet and outlet per model, Figure 7.12 can be used. Each model (0 %, 50 % and 75 %) has its own plot. Evidently, all the quadrupole and dipole sources have an increased amplitude at the outlet with respect to the inlet. The quadrupole sources however, show a much larger increase at the outlet compared with the dipole sources, which show only a minor increase in pressure amplitude. This can be explained by the fact that most noise from the quadrupole sources is generated after the constriction, near the outlet. If this noise wants to reach the inlet probe, it should propagate through the smaller cross-sectional area at the constriction, to the epiglottis and finally rotating 180° to end up in the mouth, where the inlet probe is located. Due to the difference in cross-section, the signal can be blocked. With respect to the dipole term, the source term is also active at the

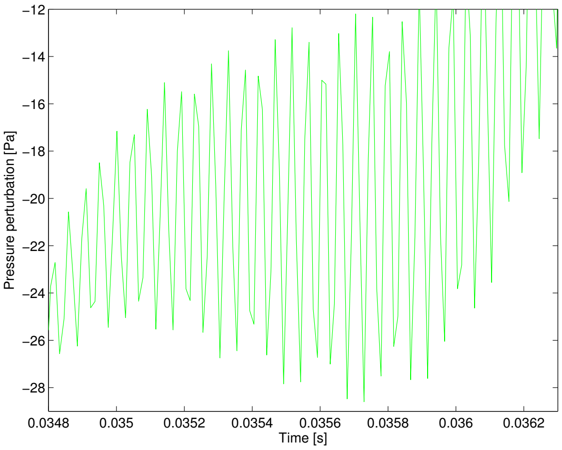

**Figure 7.11:** Zoomed part of the resulting pressure perturbation data versus time of the SUAM containing high frequency noise

constriction. This result is also substantiated by the qualitative analysis, at the beginning of this section, and will be further investigated in next paragraph using a set of new diagrams.

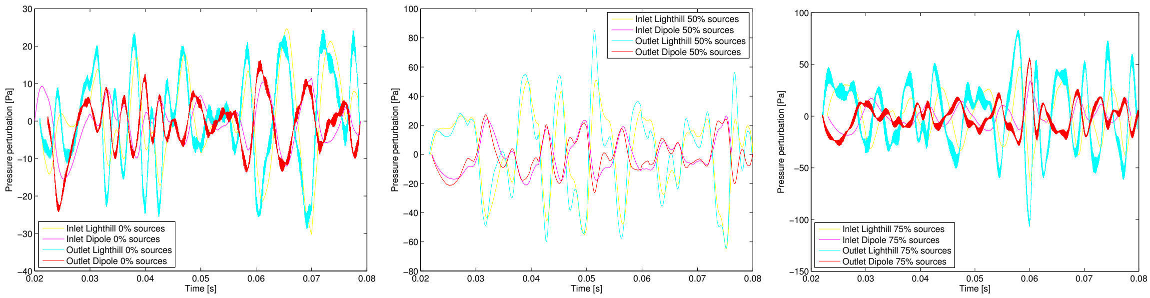

**Figure 7.12:** Resulting pressure perturbation data versus time for the original (left), 50 % constriction (middle) and 75 % constriction (right) SUAM

### 7.4.5 Comparison between different levels of constriction

To observe the differences per model, four diagrams are plotted. In Figure 7.13(a) and Figure 7.13(b), the quadrupole sound pressure results from the inlet and outlet probe are plotted. On the other hand, the dipole sources are analyzed separately in Figure 7.14(a) and Figure 7.14(b). Increasing the constriction size, leads to an increase in mixing and also an increase in sound pressure. From clinical research it is derived, that from 50 % constriction and onwards, a clear increase in sound-pressure result can be observed Zwartenkot et al. (2010). When looking at the quadrupole sources for the outlet (Figure 7.13(b)), a logical pattern of increasing sound pressure is found. A normal airway produces less noise than an airway with constriction. When looking at the inlet probe (Figure 7.13(a)), a different result is found. Here, the result from the 50 % constriction model is dominant with respect to the result from the 75 % constriction model. The noise, generated behind the constriction, has to travel upstream to the inlet probe. It therefore must cross the constriction again. A larger constriction will lead to a larger blockage of noise, thereby reducing the sound pressure at the inlet.

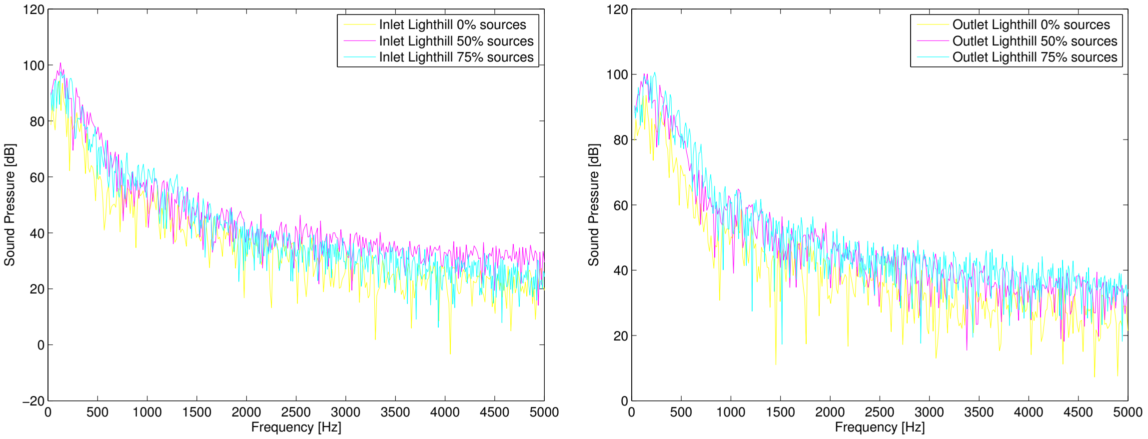

(a) Zoomed sound pressure data from the inlet probe

(b) Zoomed sound pressure data from the outlet probe

**Figure 7.13:** Quadrupole source sound pressure results versus frequency from the inlet (left) and outlet (right) probe of the SUAM

It is also useful to analyze the dipole sources in a similar fashion as the quadrupole sources. At the outlet (Figure 7.14(b)), the 75 % constriction model shows the largest sound pressure, while the clean model shows the lowest sound pressure. This is according to the theory and similar as the result from the Lighthill sources. At the inlet (Figure 7.14(a)), the results from the 50 % and the 75 % constriction model are showing approximately the same sound pressure levels. At the lowest frequencies, the 75 % model is dominant, while at the higher frequencies the 50 % model has a higher SPL. This result is more in line with the theory and the explanation for this behavior was already mentioned at the beginning of Section 7.4.1. Here, we already concluded that part of the noise generation was produced at the constriction itself, and not downstream the constriction. Probably, the sound creation part at the constriction is not blocked now, increasing the pressure levels at the inlet microphone.

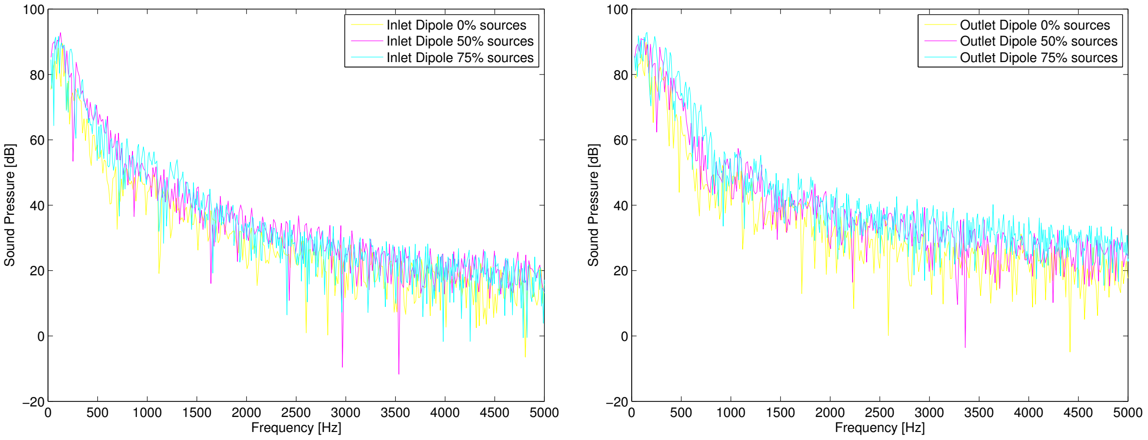

(a) Zoomed sound pressure data from the inlet probe

(b) Zoomed sound pressure data from the outlet probe

**Figure 7.14:** Dipole source sound pressure results versus frequency from the inlet (left) and outlet (right) probe of the SUAM

# Chapter 8

# Analysis of a realistic CT-scan derived airway model

Using the results and experience from the simpified model in previous chapter, it is now interesting to investigate a Realistic Upper Airway Model (RUAM). A stridorous geometry is captured from a CT-scan, while a healthy person is modeled by Lynch (2012) with the help of H. Hoeve. By comparing both models, the predictive capability of the detection method can be investigated. More important is to see how the sound production varies between both models and how this will affect the results at the inlet probe. It will also give insight which source term is sufficiently good for the analysis of a realistic upper airway. First, the geometry is discussed. Afterwards, the boundary and initial conditions are introduced. This is followed by an extensive discussion of the fluid flow and (vibro)-acoustic results.

## 8.1 Geometry

The RUAM consists of two different models: the first one is directly derived from a CT-scan of a patient suffering from stridor (geometry is captured by W. Vos at FluidDA), while the other version is an adapted version of the stridorous model. The model is adapted by Lynch (2012) such that it represent a healthy person. Both models were already introduced in Figure 2.8. Since the geometry is rather complex, another three dimensional view is added in Figure 8.1, also containing a detailed image of the structural shell model.

First of all, it should be mentioned that the top part of the model is not present (the right side on the top picture in Figure 8.1). The algorithm to convert a CT-scan to a three dimensional CAD model is not optimized for the nasal cavity. Therefore, the model is cut near the nasopharynx. This can influence the results in two ways. First, the inlet condition should be set differently with respect to the SUAM, where the flow traveled through the mouth thereby making a bend of 180° to reach the nasopharynx. There is a possibility that the

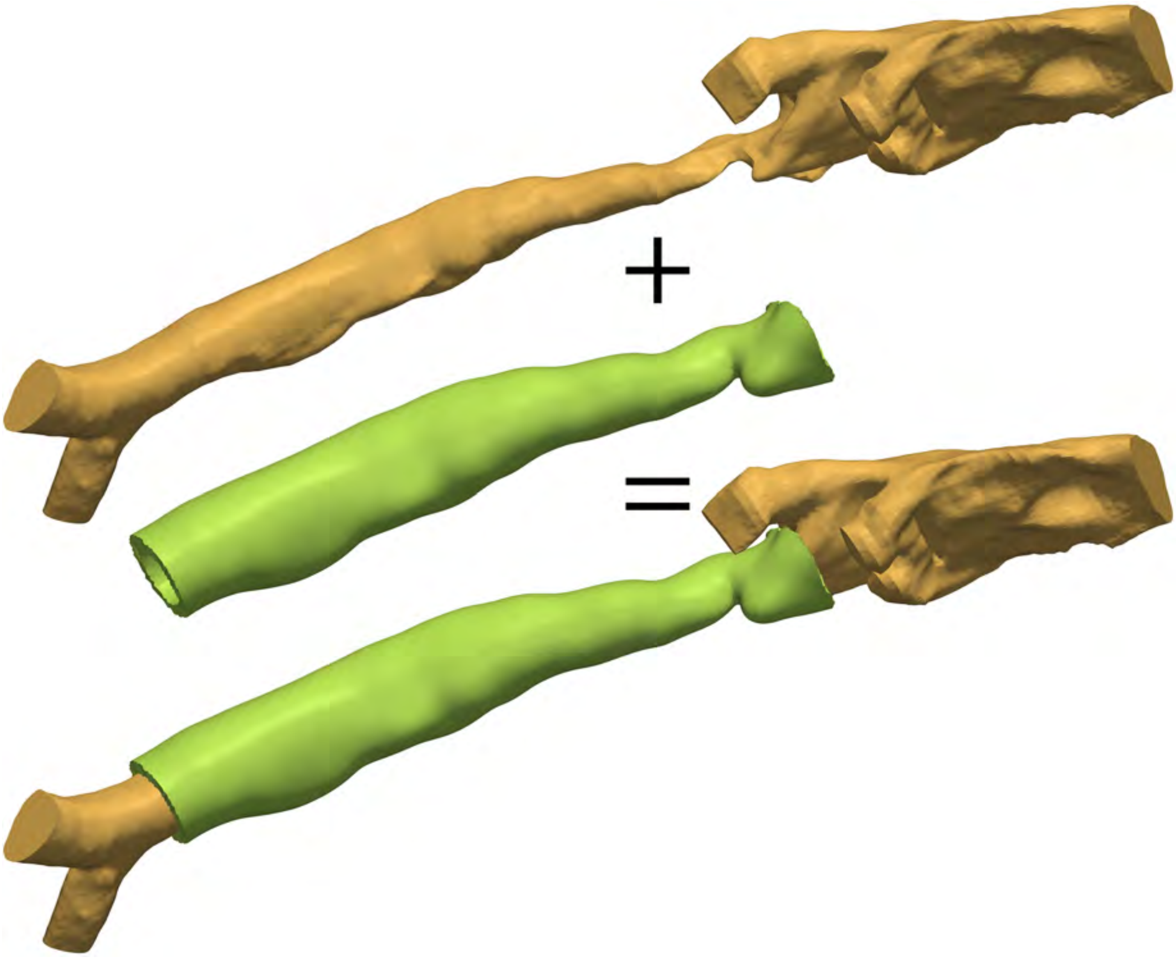

**Figure 8.1:** Three dimensional overview of the RUAM, derived from a CT-scan of a patient suffering from stridor. The model on top is used for the flow equations, while the model in the middle is used for the structural equations. The model at the bottom is a combination of both, used in OpenFOAM®

flow might become turbulent or separated before reaching the nasopharynx. Hence, the inlet of the RUAM can not fully represent the correct flow. On the other hand, an extra sound source at the inlet might be canceled now, making the sound production fully dependable on the major sound source at the trachea. Also the location of the inlet probe is now different (nasopharynx), with respect to the SUAM (mouth). However, this will probably only influence the amplitude of the signal, which is not the main concern in this study. The focus lies only on the differences between the constricted and normal model and its clinical application.

Concerning the anterior side of the model in Figure 8.1, two dead end air pockets are observed. This is caused by the tissue that is connected to the epiglottis and the epiglottic vallecula. On the posterior side there are air pockets which are caused by the esophagus. Further downwards (to the left on the picture) a v-shaped region can be observed. This is the place of the vocal cords. A small bump over there is caused by the connection points of the vocal cords. Below the vocal cords a subglottic stenosis is located at the constricted model. In the clean model, the stenosis is removed, thereby increasing the cross-sectional area. Further downstream the trachea becomes bigger, and split up into the two bronchi.

Next to the fluid mesh, a structural mesh is created for evaluating the vibrations at the wall. As can been seen, only part of the model is surrounded by this model. At these locations, it is likely that the flow is going to be turbulent, thereby introducing vibrations. The thickness of the trachea wall varies between 1 mm for children, to 3 mm for adults Standring (2008). Since the fluid model is based a CT-scan of an adult, an off-set of 3 mm is used for the shell of the structural mesh. Next, a three dimensional tetra-mesh is used to fill the shell.

The final result can be found at the bottom picture in Figure 8.1. This model is used in OpenFOAM®, to solve for the acoustic analogies. One mesh density was used, which was already verified by Lynch (2012). The fluid mesh consists of $2.08 \cdot 10^6$ cells and the structural mesh consists of $4.49 \cdot 10^5$ cells, making the run time of approximately 0.5 s one month.

## 8.2 Boundary and initial conditions

The boundary and initial conditions for the RUAM are approximately the same as for the SUAM. At the inlet, a differential, density normalized, uniform pressure is set. The velocity is determined automatically based on the pressure difference between the inlet and outlet. This allows for an non-uniform inflow, which is wanted due to the fact that the oral and nasal cavity are not available in the computational model.

At the outlet the pressure has a zero-gradient condition and the velocity is imposed such that the correct mass flow is achieved. Unfortunately, for the RUAM model, no reference data is available (even no patient measurement data). It is assumed that during the CT-scan, the patient was breathing slowly. Therefore, the geometry of the upper airway model is only valid for slow breathing problems. To fulfill this requirement, a boundary condition of 12 L/min is chosen, based on the research performed in Chapter 2.

For the acoustical waves, again a convective outlet equation is used. The wall close to the in and outlet also have a convective boundary condition for better convection of waves perpendicular to the inlet and outlet. This was already introduced in the SUAM model. Also the quadrupole source term is set to zero near the inlet and outlet, to reduce numerical noise caused by these parts of the model. This solution strategy is already extensively discussed in the diaphragm validation model.

The structural mesh consists of two boundary conditions, similar as the diaphragm validation model. On the outside, the model is fixed, while on the interface, the pressure is set on the wall as a force using the traction boundary condition.

## 8.3 CFD results

Due to the complexity of the model, it is useful to first discuss two vector plots of the most important regions of the RUAM. This way, a good overview of the model can be obtained. In Figure 8.2, a vector plot near the constriction for a single time-step is displayed. Especially below the vocal cords (which is positioned at the top of the figure), the jet causes a transition from laminar to turbulent flow. For the stridorous patient (right picture) a strong back-flow is observed on the left side of the jet (posterior side), see the lower part of the image. Here, the blue arrows are pointing upwards. Also below the jet, the flow stays three-dimensional. For the healthy patient (left image of Figure 8.2) no extreme high jet velocity is observed. However, behind the vocal cords, on the anterior side of the model, a couple of recirculation zones are observed. These are characterized by the different whirls.

The exact placement of the jet, recirculation zones and back-flow together with the exact velocities can better be observed in a velocity plot. In Figure 8.3, the instantaneous vertical velocity is plotted for the healthy and stridorous patient on the same color-map. There is a large difference in velocity between the normal and constricted model. The velocity of the jet of the constricted model is approximately 19 m/s in vertical direction, while in the normal model the jet reaches a velocity of approximately 8 m/s. This result can also be found in the instantaneous velocity magnitude plot, added in Figure 8.4. This low value in the healthy model is due to the larger cross-section (with respect to the constricted model) and because of the fact that the flow can stream more smoothly into the trachea resulting in a more uniform flow. In the constricted version, the flow needs to bend more, experiencing adverse pressure gradients causing flow separation and jet formation. These regions are clearly visualized by the pink color in the plot. Another important difference between both models is the location of surface attraction, also known as the Coandă effect. With the healthy patient model, the jet attaches to left side (posterior part, consisting of only soft tissue) while with the stridorous patient the jet attaches to the right side (anterior part with c-shaped cartillages, which gives rigidity to the trachea). Note that this result is the opposite with respect to the result from the SUAM. For further studies, a more realistic surface model should be built, including for example the c-shaped cartillages. With this model, a comparison between anterior and posterior jet attraction can be made, taking into account the non-uniform tissue properties.

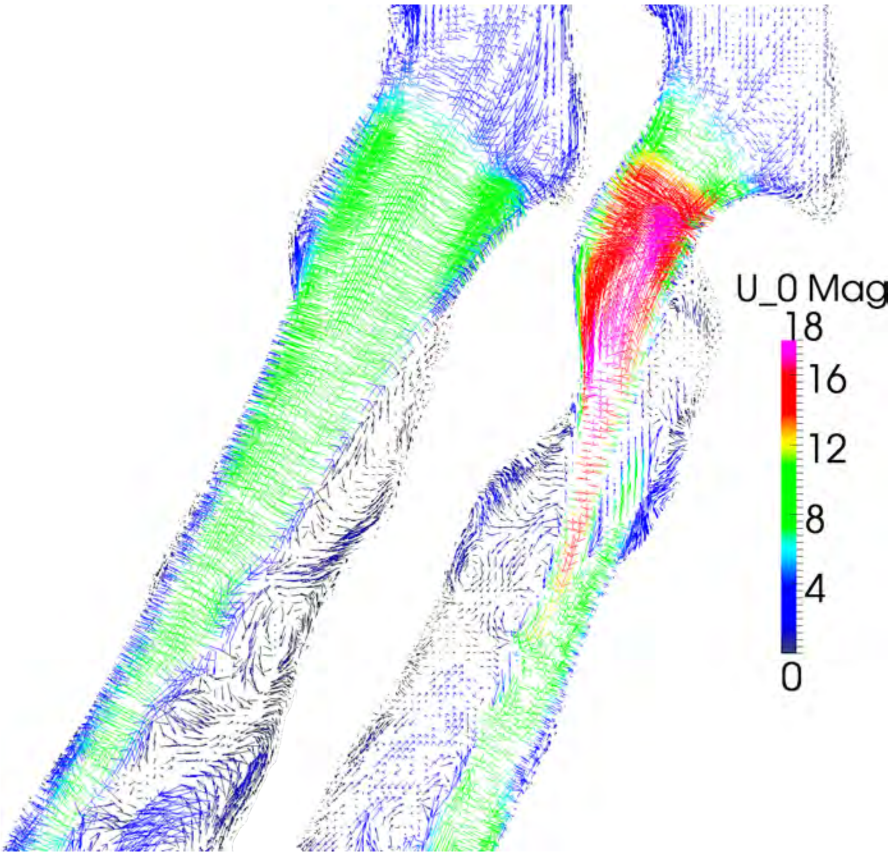

**Figure 8.2:** Snapshot of streamlines for the clean (left) and constricted (right) RUAM

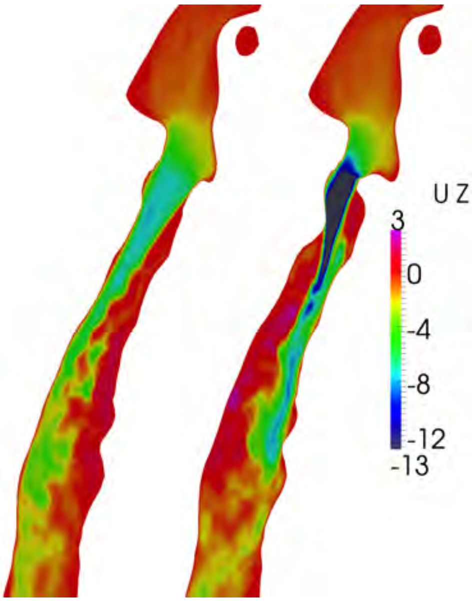

**Figure 8.3:** Snapshot of the instantaneous velocity in vertical direction for the clean (left) and constricted (right) RUAM

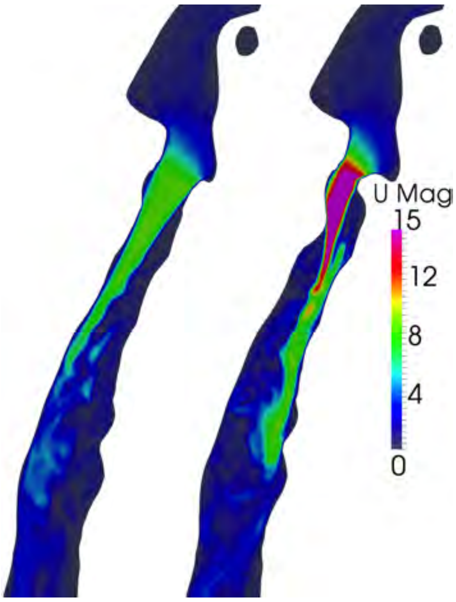

**Figure 8.4:** Snapshot of the instantaneous velocity magnitude for the clean (left) and constricted (right) RUAM

The vorticity is used to calculate the selection function, required for the selective Smagorinsky SGS model. It is also used as the starting point of the indication of sound, using the quadrupole sources. The vorticity result for both models can be found in Figure 8.5. The vorticity in the constricted model is stronger, but is also more spread out over the domain. The regions of vorticity are thicker and the result from the opposite jet attachment can also be observed from the vorticity plots. The result for the quadrupole source term will be discussed in the next section.

Finally, the last interesting fluid parameter is the pressure (Figure 8.6). Despite the same color-map, a large difference can be seen between the two models. The patient suffering from stridor experiences a much larger pressure drop (approximately 250 Nm/kg) which indicates that the patient needs much more effort to obtain the same mass flow as a healthy patient (approximately 50 Nm/kg), even with the conditions for quiet breathing.

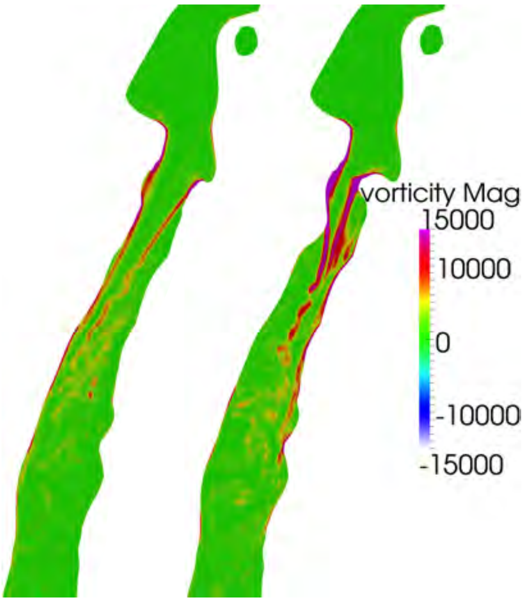

**Figure 8.5:** Snapshot of the vorticity modulus $\|\omega\|$ for the clean (left) and constricted (right) RUAM

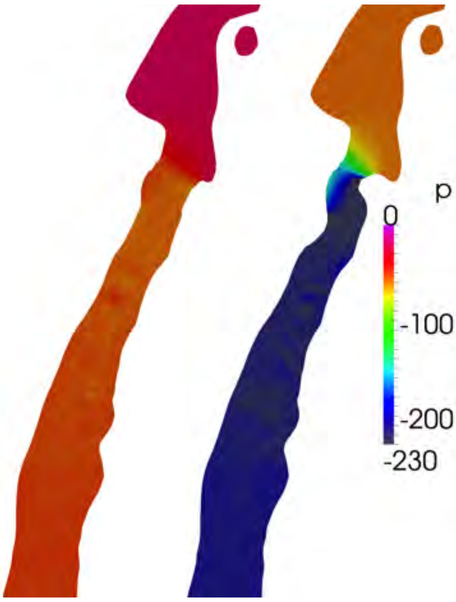

**Figure 8.6:** Snapshot of the pressure for the clean (left) and constricted (right) RUAM

## 8.4 Acoustic results

For the acoustic computations, the same mesh density as in the fluid model is used. A similar analysis as for the SUAM is done. Hence, first the raw density results are dentrended by a cut-off of frequencies of 50 Hz in order to perform a Fourier analysis. For the quantitative analysis, the first 0.02 s are clipped and the simulation is run until 0.12 s. However, first a short qualitative analysis will be performed.

### 8.4.1 Qualitative analysis

When looking at the quadrupole source term in Figure 8.7, similarities with the vorticity plot can be obtained. First of all, the acoustic sources for the constricted model are about 5 times stronger than the clean model. They are also much more active in a larger part of the domain. Still, the healthy person shows much noise next to the jet, at the location of the recirculation zones. A possible reason is that the upper airway is not modified enough to perform as a healthy model. Therefore, for further research, it would be useful to obtain a CT-scan derived model of a healthy person.

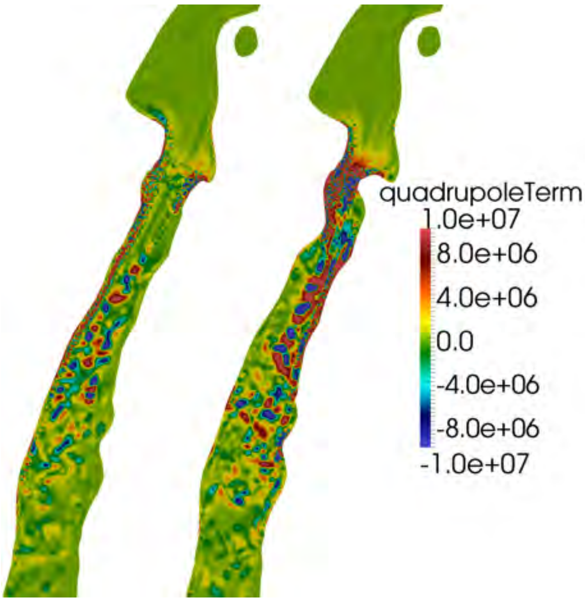

**Figure 8.7:** Snapshot of the quadrupole source term for the healthy (left) and stridorous (right) patient RUAM

The dipole term is also illustrated in Figure 8.8. A different color-map is used, to clearly visualize the fluctuations within the model. Clearly, due to the large difference in pressure per model (see previous section), the dipole term also varies a lot between both models. Important here is that, the source term is already active at the constriction and not only after the constriction. This might lead to larger noise values at the inlet compared with the quadrupole source term results. Results will be discussed later. Above the vocal cords, the dipole term is approximately zero.

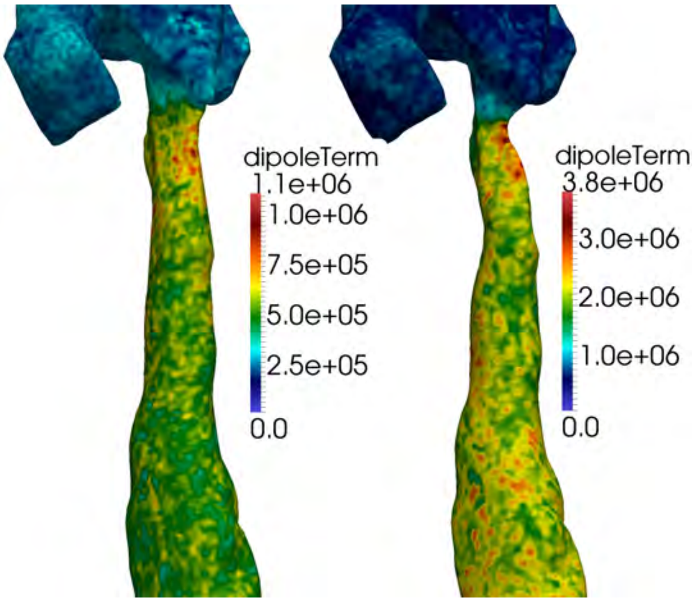

**Figure 8.8:** Snapshot of the dipole source term for the healthy (left) and stridorous (right) patient RUAM

## 8.4.2 Inlet probe results

Now that both source terms are qualitatively discussed (monopole term will be discussed later), it is interesting to discuss the inlet and outlet probe results. First, the pressure perturbations of the inlet probe are plotted in Figure 8.9(a) together with the overall sound pressure data of the inlet probe (Figure 8.9(b)). As can been seen from the pressure perturbation plot, the quadrupole sources have a much larger amplitude with respect to the dipole sources. On the other hand, the dipole sources have more oscillations, hence a larger frequency. Also, the amplitudes of the signal of the constricted model are somewhat higher compared with the normal model. Within the result of the healthy model, high frequency oscillations are present. This can also be observed in the sound pressure plot, where a frequency peak is present around the 5600Hz for both Lighthill sources. This can be caused by internal reflections in the model or a sharp edge at the boundary. However, for this difficult geometry, it is hard to find the underlying cause. One possibility could be that reflection of noise just above the glottis. The distance between the anterior and posterior side is 30mm. A wave should then have a frequency of about $346.15/(0.03 \cdot 2) = 5767$Hz. When looking at the dipole sources, multiple peaks are found at the higher frequency ranges. This could indicate stridor noise. However, from research from Zwartenkot (2010) is known, that common stridor noise is located between 150Hz and 2500Hz. Nevertheless, this noise is still within the human hearing limits and could be captured by a microphone.

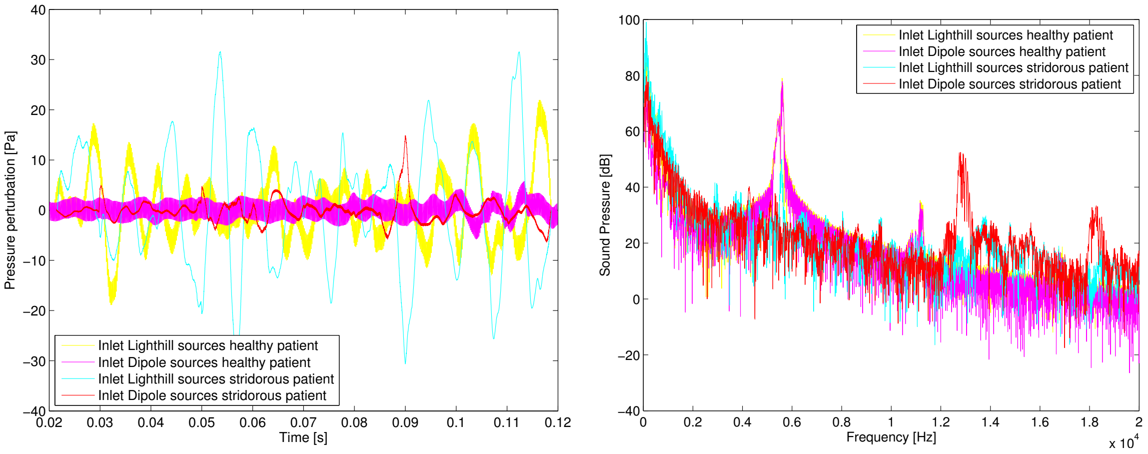

(a) Resulting pressure perturbation data versus time

(b) Overall sound pressure data versus frequency

**Figure 8.9:** Acoustic pressure results from the inlet probe of the RUAM

### 8.4.3 Outlet probe results

Similar results are derived from the outlet probe of the RUAM. The main difference with respect to the inlet probe is the larger amplitude of pressure perturbations, see Figure 8.10(a). The differences between the healthy and stridorous patient are now also more pronounced. This result is also clearly visualized in Figure 8.10(b), where the differences between the stridorous and healthy model are very clear for frequencies above $10,000$ Hz. A large Sound Pressure Level (SPL) is observed at high frequencies. Even higher peaks are observed for the dipole sources. At this point, it is too difficult to assign such peaks to certain phenomena. More research is therefore required. However, what can be concluded is that the sound source is not present in the healthy model, where for example turbulent flow is less present. Please also mind the axis scaling between the inlet and outlet probe results.

### 8.4.4 Comparison between inlet and outlet

To further compare the inlet and outlet results, Figure 8.11 is used. Here the inlet and outlet probe results are plotted per model. As a first observation, the dipole sources for both the inlet and outlet, and models are showing high frequency oscillations. This result was already found before. Another clear difference is the inlet versus outlet signal. At the outlet of the constricted and clean model, the signals are much stronger. The same result was found for the SUAM. See previous chapter for more details.

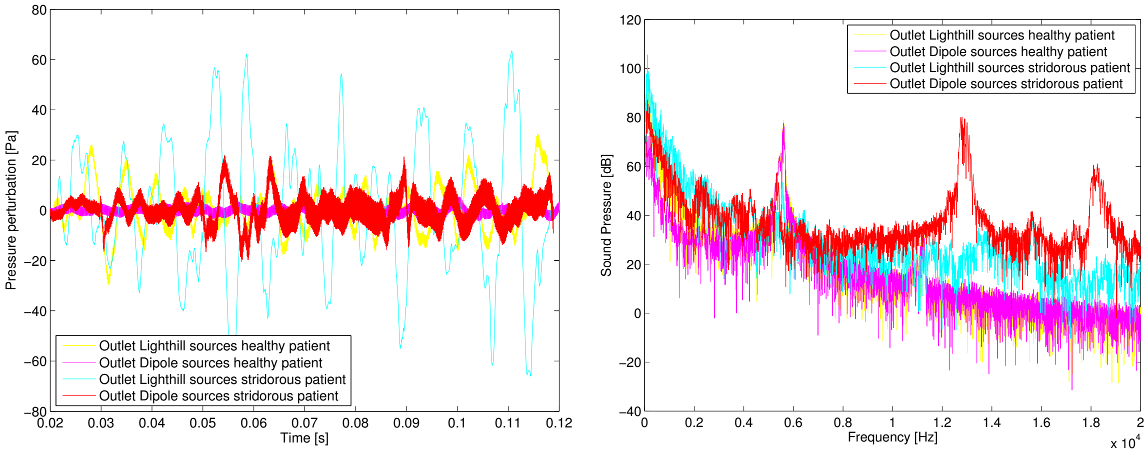

(a) Resulting pressure perturbation data versus time

(b) Overall sound pressure data versus frequency

**Figure 8.10:** Acoustic pressure results from the outlet probe of the RUAM

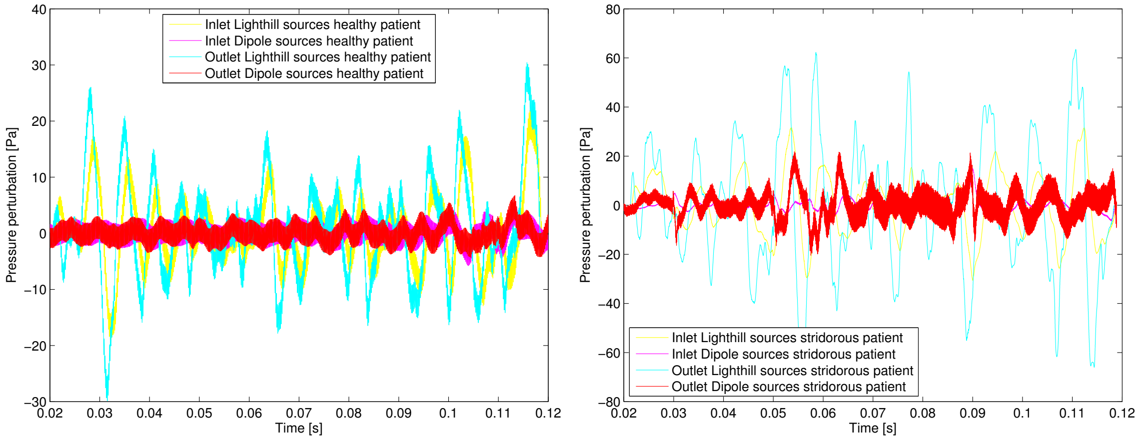

**Figure 8.11:** Resulting pressure perturbation data versus time for the healthy (left) and stridorous (right) patient RUAM

### 8.4.5 Comparison between different levels of constriction

Finally, a comparison per model is made. This analysis is essential for the scope of this project and will answer one of the first main questions: Does a constricted model shows an increase in sound pressure level at the inlet compared with a normal model? To discuss the results, all sources will be discussed separately. Starting with the quadrupole sources, the result is depicted in Figure 8.12(a) and Figure 8.12(b). At the outlet, the result is as expected: the acoustic sound from the quadrupole sources is much higher for the stridorous patient with respect to the healthy patient. A difference of approximately 15 dB is observed. This large difference is decreased to 5 dB for the inlet probe, but still present. The noise generation of the constricted model is thus stronger, which is a different result with respect to the SUAM. Nevertheless, it is also important to mention that for the higher frequencies, the healthy patient model becomes dominant with respect to the SPL. For both the inlet and outlet, the stridorous SPL shows small peaks at 3000 Hz, 3700 – 3800 Hz and 4600 Hz. These small variations in the pattern of the sound spectrum could be indicators of a stridorous tone.

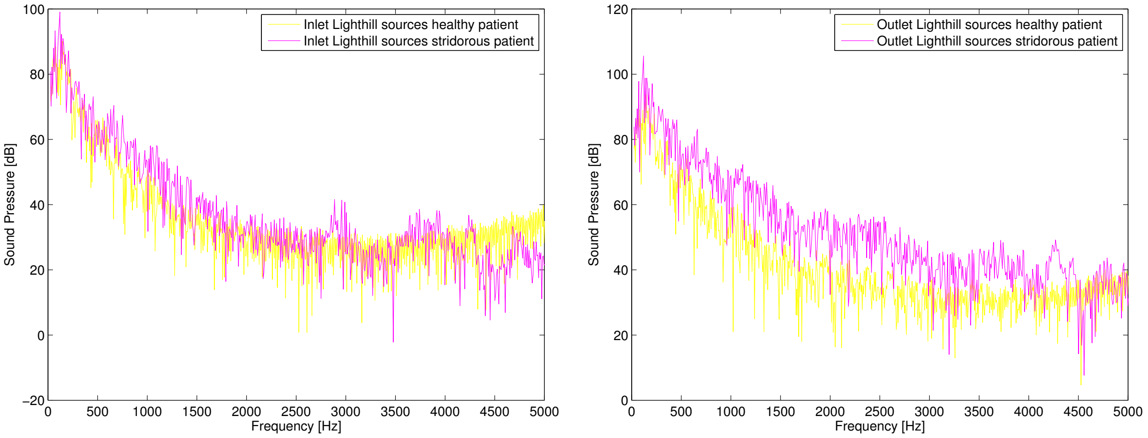

(a) Zoomed sound pressure data from the inlet probe

(b) Zoomed sound pressure data from the outlet probe

**Figure 8.12:** Quadrupole source sound pressure results versus frequency from the inlet (left) and outlet (right) probe of the RUAM

Further research is thus required for comparing the healthy patient and stridorous patient model. The same research can be held for the dipole sound sources. The results for the inlet and outlet are plotted in Figure 8.13(a) and Figure 8.13(b) respectively. Both images show expected results: the constricted model has a more pronounced sound spectrum with respect to the clean model. In the case of the outlet probe, the difference is approximately 20 dB while for the inlet, the difference is measured at 10 dB. Compared with the quadrupole sources, the difference between both models at the inlet is much larger for the dipole source term, making this source term more active at the input probe. Also, similar to the quadrupole source results, the stridorous model shows some variances in the higher frequency spectra (between 2000 – 5000 Hz). These are again indicators for an increase in turbulence, and probably for stridorous sound.

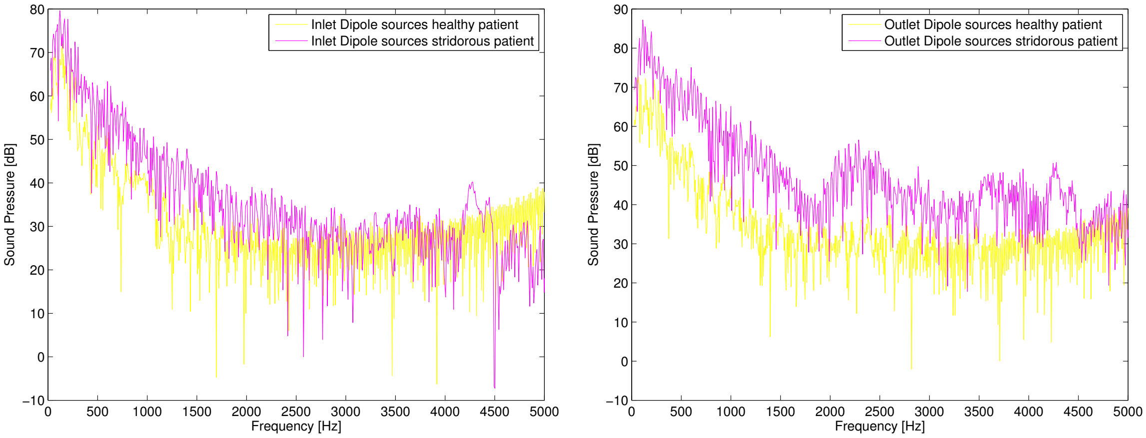

(a) Zoomed sound pressure data from the inlet probe

(b) Zoomed sound pressure data from the outlet probe

**Figure 8.13:** Dipole source sound pressure results versus frequency from the inlet (left) and outlet (right) probe of the RUAM

### 8.4.6 Comparison with patient reference data

Both results from previous section can be compared with results from Zwartenkot (2010). From this technical report, patient information is obtained using a microphone near the mouth. Three examples are attached in Figure 8.14(a), with in the legend of the plot a description of the type of stridor. Clearly, each patient shows different results. This makes an accurate detection model very difficult. Only one of these results shows similarities with the results from the RUAM. The data from a 1-month-old boy with laryngomalacia and subglottic stenosis is used. The reference data, together with the simulation data from the inlet probe of the constricted model is plotted in Figure 8.14(b). Please note the difference in ages between the reference and simulation data. The simulation model is from an adults upper airway model, while the reference line contains data from an neonate. However, the overall resemblance of the sound spectrum of the simulation is similar as the result from Zwartenkot (2010). Nevertheless, a large peak after the first peak is missing, which is definitely an important part of the stridor noise of this specific patient. Much more noise data was present in Zwartenkot (2010). However, this data does not have the same stridor cause as in the RUAM, and could not be considered.

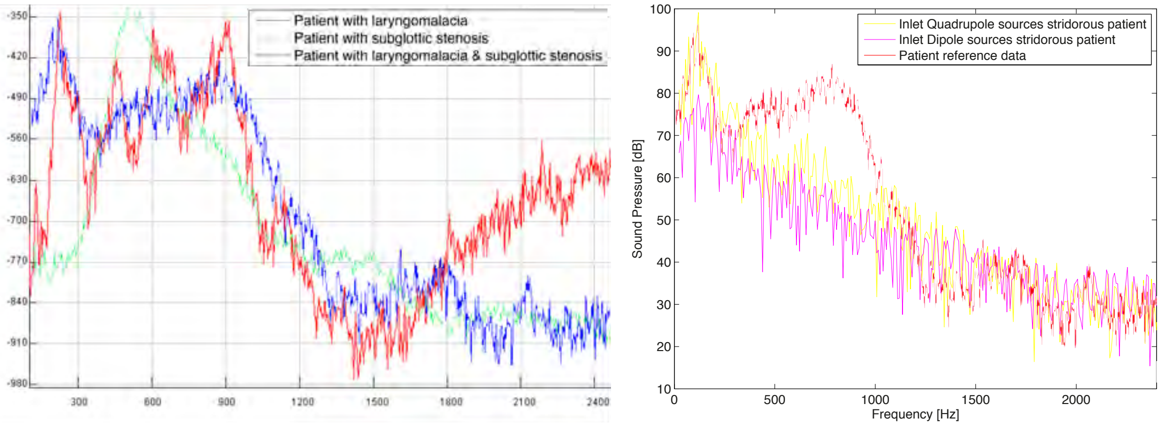

(a) Sound pressure data from three different patient models

(b) Zoomed sound pressure data from the inlet probe of the RUAM and patient data

**Figure 8.14:** Sound pressure results versus frequency from the inlet (left) probe of the RUAM compared with actual patient data from Zwartenkot (2010)

### 8.4.7 Monopole term analysis

As a final investigation into the sound production of the RUAM, the monopole source term should be discussed. This term, derived from the structural displacement vector, gives an indication of the sound production due to vibration. This vibration is introduced due to the pressure distribution in the fluid domain. More information can be found in Chapter 5. To discuss the source term, first the structural model is investigated. The displacement result at the interface wall is plotted in Figure 8.15 for two soft tissue models. A large difference per model is observed (a factor six). However, the absolute displacement values are very low ($1 \cdot 10^{-7}$ m). Nevertheless, the acceleration term of the tissue, the parameter used for the monopole source term, can still be large because of the high frequency of vibrations. It reaches values of $1 \cdot 10^5$ m/s$^2$.

From this information, the monopole source term is extracted. Two cases are investigated: a comparison between the healthy model and stridorous model and a comparison between two extremes of mechanical properties of the structural mesh. The values are adapted according to the values in Table 5.1. Hence, a firm tissue and soft tissue investigation is performed. The results are presented in a similar fashion as the results of the two previous source terms. However, since this model only has run for a very short time (due to the fact that at this point the interpolation scheme between fluid and structure does not support parallel application running), the data is not very accurate and can not be compared with other source terms. Improving the coupling procedure and thereby decreasing the run-time of the monopole sources should be part of any further study.

The pressure perturbations and sound spectrum results for the three simulations can be found in Figure 8.16(a) and Figure 8.16(b). Comparing both structural meshes of the stridorous

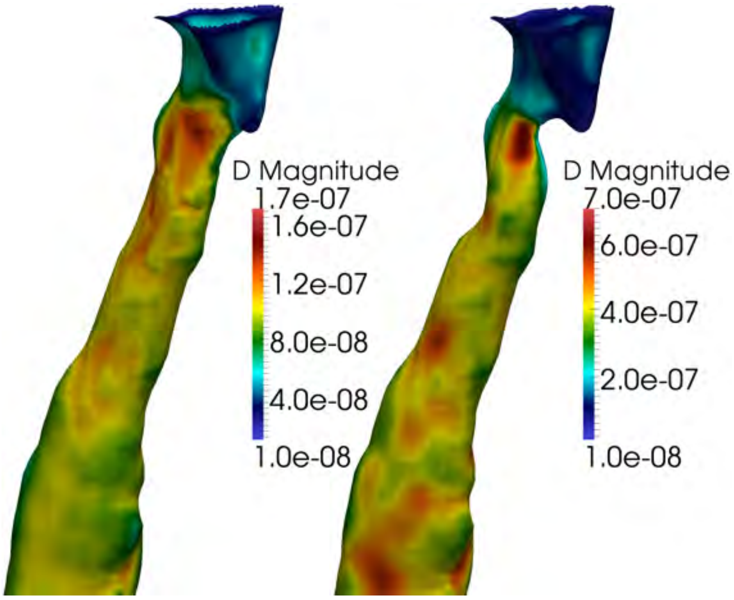

**Figure 8.15:** Snapshot of the displacement magnitude at the interface boundary of the soft tissue structural mesh for the healthy (left) and stridorous (right) patient RUAM

model, both pressure perturbation amplitude and sound pressure level are increasing with softer tissue properties. Such a large difference is less pronounced comparing both soft tissue results from both models. Both soft tissue models show similar sound pressure levels, indicating that even the healthy model is already producing noise. This is due to the very soft tissue properties, chosen for this simulation. The main differences between the healthy and stridorous model are the two large peaks for the stridorous patient models with soft tissue properties. Those peaks, located around 3500 Hz and $16,000$ Hz, might be an important source for the sound production of stridor. However, according to Zwartenkot (2010), stridor noise is low frequency noise, produced in the $0 - 5000$ Hz region. This indicates that the second peak is not a distinctive stridorous peak.

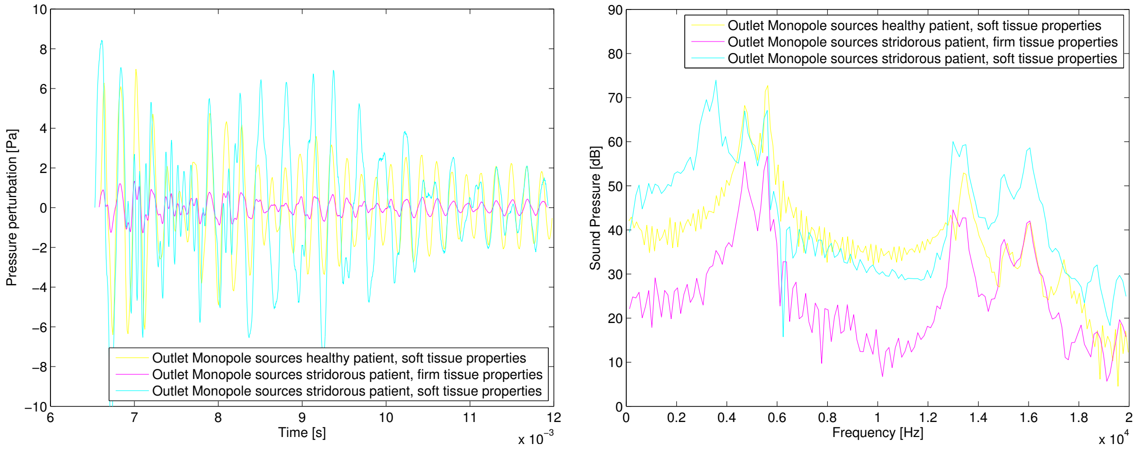

(a) Resulting pressure perturbation data versus time

(b) Overall sound pressure data versus frequency

**Figure 8.16:** Monopole source acoustic pressure results from the outlet probe of the RUAM

# Chapter 9

# Conclusions and recommendations

In this MSc thesis, the numerical investigation of a patient's upper airway suffering from stridor is investigated using a fluid-structure-acoustic interaction simulation in OpenFOAM®. The geometry of an upper airway model is very difficult, leading to various cross sections and a large spectrum of flow phenomena. Next, there is a large difference in geometry per patient, especially with respect to age. Also, taking into account the various possible causes of stridor, current detection methods are scarce and mostly unsuccessful. There are too many variables and there is too much variation in a detection model in order to accurately predict the noise. This thesis investigates a numerical detection method, allowing to change one variable each time a simulation is run. The main results and conclusions together with a discussion about the possible further study opportunities are mentioned in different sections below.

## 9.1 Conclusions

### 9.1.1 Physics and modeling

To start building a detection method, a simulation model has to be built. A fluid-structure-acoustic interaction model is created using:

- A flow model based on the Navier-Stokes equation.
- A Large Eddy Simulation used to accurately predict the turbulence flow.
- Direct wall modeling.
- A subgrid-scale model based on selective Smagorinsky is used, to close the fluid flow model.

- A new in-house solver implemented in OpenFOAM®, together with a new acoustic and structural solver.
- An acoustic solver based on the hybrid methodology. Instead of using the integral solution of an acoustic analogy, the complete partial differential equation is solved. On the right hand side the Ffowcs-Williams and Hawkings (FW-H) sources are used, consisting of quadrupole, dipole and monopole sources.
- A Finite Volume linear stress analysis solver to solve the structural displacements, required for the acoustic analysis.

### 9.1.2 Validation

The in-house solver is validated using various analytical models. For the quadrupole sources, a co-rotating vortex pair is used while for the dipole and monopole sources, the analytical integral solution of the FW-H analogy is used. The overall resemblance is good, the numerical models closely match the (approximate) analytical solution. The diaphragm model, more closely related to an upper airway model, is used for validation of the fluid and acoustic domain. Important results and conclusions are:

- The Computational Fluid Dynamics (CFD) results for the two-dimensional case are poor, while the three-dimensional case show accurate results with respect to the reference paper.
- Acoustical reference data was available, making it possible to verify the acoustic sound spectrum:
  - The acoustic results for the dipole source term are showing the same pattern and amplitudes as the reference.
  - The quadrupole sources on the other hand, seems to be somewhat over-predicted. This is counter-intuitive from the theory presented in this thesis. A possible reason is the cut-off of the source term in the middle of a source/sink combination. To solve this issue, the increase of the cell-area near the end of the domain of the diaphragm, thereby simulating a longer domain to damp out the turbulence, is proposed. However, the result from this simulation turns out to be similar to the original model, where the cut-off method was used.
  - The monopole source term is very effective in the diaphragm model. This sound source is simulated twice with varying tissue properties. The result shows a clear difference between soft and firm tissue modeling, with large and small pressure perturbations respectively.

### 9.1.3 SUAM

Before a realistic upper airway can be modeled, the in-house solver is validated using a simplified upper airway model (SUAM). Three models are used (0 %, 50 % and 75 % constriction) to observe the difference between the constriction sizes. The most important results and conclusions are summarized below:

- The CFD results are as expected: when increasing the constriction size the
  - Jet velocity increases.
  - More turbulence regions are observed.
  - Larger and stronger recirculation zones appeared.
  - The backflow velocity increased.
  - Strength of the vorticity increased.
  - Larger pressure drops were observed.
- These fluid characteristics are affecting the noise spectrum. Important conclusions are:
  - The quadrupole sources are the most dominant noise sources
  - No distinctive peaks at all frequencies can be found. This makes the SUAM not suitable for validating noise prediction and propagation.
- Another study into the differences between the inlet and outlet signal showed that the outlet signal is much stronger than the inlet signal. This is due to the fact that the majority of the noise production takes place behind the constriction, closer to the outlet probe. The constriction itself also blocks the noise, leading to a lower sound pressure level (SPL).
- The different models are also compared per constriction with respect to their inlet and outlet probe results:
  - In case of the quadrupole sources, the 50 % constriction case shows the largest SPL at the inlet probe. This is strange, since much more vorticity is observed at the 75 % case. However, as is known from previous study, the constriction will block part of the noise. In case of the 75 % constriction model, more noise is blocked than extra created compared with the 50 % constriction case.
  - When looking at the dipole source term results, the result is the opposite. As expected, the largest SPL at the inlet is observed at the 75 % case. Probably, this is due to the fact that a large part of the noise is generated at the constriction, instead of below the constriction (as in the case of quadrupole sources).
  - At the outlet probes, the noise levels are as expected and the 75 % case is showing the most dominant SPL's.

### 9.1.4 RUAM

As final model, the realistic upper airway model (RUAM) is simulated. A stridorous model, as well as a healthy model are solved. The most important conclusions are:

- The CFD results are approximately the same as in the SUAM model:
    - The same characteristics are found, as well as the connection with increasing constriction size.
    - One interesting observation is the wall location of the jet attachment. This is changed per model, due to the constriction. The result is opposite to the SUAM result.
- With respect to the noise inlet and outlet results, the general conclusions are:
    - The source term magnitudes for the stridorous patient model are much higher compared to the healthy patient model.
    - Investigating the pressure perturbations, the quadrupole sources can be recognized by a large amplitude while the dipole sources can be identified by many low amplitude oscillations.
    - On the entire noise spectrum, clear different frequency peaks are present. The quadrupole and dipole sources are each showing different peaks, which are difficult to assign to a phenomenon. The geometry is too difficult for that.
- An investigation into the inlet versus outlet probe results shows that at the outlet probe of the constricted model a much higher SPL is observed compared with the inlet probe. The same holds for the healthy model, but the difference between inlet and outlet are much smaller. This is probably due to the fact that there is no constriction, so the blockage of sound is negligible.
- The inlet probe results per model are also compared. The result is as expected: the stridorous model has the most dominated SPL for both the quadrupole and the dipole term.
- A comparison with patient data shows reasonable resemblance with the quadrupole results. One peak is found for a patient with a similar stridor cause. However, the simulation data is from an adult, while the acoustical data is from a neonate.
- The structural mesh is verified using soft and firm tissue. The displacements for the soft tissue were six times higher compared to the firm tissue mesh. The same results are presented in the SPL plot. In addition, the stridorous model shows extra peaks in the lower frequency range, probably indicating stridor noise.

## 9.2 Recommendations

The results and conclusions presented before show that there is still some work to do to reach the final goal; being able to accurately predict sound from a given geometry and using these results, determining the inverse solution. This following list describes some ideas for further work:

- More stridor causes should be observed to enlarge the database of results. From experimental data it is known that different stridor causes result in a different sound pressure spectrum. It is thus useful to, for example, investigate more flexible stridor problems with larger deformations, as well as more stiff stridor causes.

- Now, only a first order scheme for the second time derivative is used. With this scheme, a very small time step is required for an accurate solution. In the future, a second order scheme should be used to decrease computational time.

- The in-house solver is based on a weak, one-way coupling between the fluid, structure and acoustic domain. For further research, this method should be adapted, thereby creating a strong-coupling interaction method. One should start by implementing a strong coupling between the acoustics and structure: noise created in the volume (quadrupole sources) should propagate through structures, thereby creating new vibrations at the interface boundary of the model. A next step should be mesh motion (in case of observing flexible stridor causes) by creating a strong coupling scheme between acoustics/structure and fluid. In the case of flexible constrictions, the mesh adaption will influence the fluid flow.

- Also, currently only simplified models (such as the diaphragm) can be solved in parallel. The in-house solver consists of a difficult interpolation scheme, to interpolate data between the structure and fluid mesh. This solver needs to be updated in order to solve more difficult geometries (such as the SUAM and RUAM) in parallel.

- Now, when verifying the acoustical data, the raw pressure line is detrended using a cut-off frequency. This is an unwanted extra step which should be avoided. An improvement in the acoustical solver, by for example fixing the inlet or outlet raw pressure value might save this extra step.

- As a validation tool, an analytic solution is very useful. Now, the acoustic sources are only checked using a two-dimensional model. For further studies, more validation studies are needed. For example, using three-dimensional geometries that are different then the current two-dimensional models.

- Constantly, the result from the Lighthill sources seems to be over-predicted with respect to reference solutions. To solve this, in this thesis a longer domain with larger cell-area is attempted. However, no good results were obtained. Therefore, other options should be investigated, such as the adaption of the viscosity at the end of the domain. This might damp out turbulence quicker, resulting in a total capture of the turbulence.

- Now, the monopole source term is solved using soft and firm tissue properties. This investigation can be extended by varying more quantities at different locations (such as different structural properties per section of wall). More research into the tissue and stiffness of an upper airway has to be performed, which can be used to simulate a more realistic structure model. Think about the improvement of the structural model using the c-shaped cartilages. This can eventually lead to a research into the effect of tissue stiffness on sound production.

- The monopole term is dependent on the structural mesh. At this point, the structural mesh consists of two boundary condition: the traction condition and the clamped condition. An advanced boundary condition has to be developed at the outside of the domain to better represent the reality. Think about a freely moving boundary condition, based on the back pressure generated by the intercostal muscles. The averaged under pressure can be used for this, and set on the outer wall. This creates a realistic picture of breathing inside the human body.

- The SUAM should be extended to a fully fluid-structure-acoustic interaction model. Now, only the quadrupole and dipole sources can be investigated, since no structural model is present to take into account monopole sources.

- The RUAM model is derived from an actual patient suffering from a subglottic stenosis. Unfortunately no actual acoustic data is present from this patient. It should be useful for further study to have a new CT-scan derived model, with acoustic patient data. After a surgery of this patient, a new CT-scan together with an acoustic record of breathing should be made. This way, a realistic healthy model can be obtained together with actual patient noise data. This is then useful to compare with the stridorous model of the same patient.

# Bibliography

S. Ahmed and D. Giddens. Velocity measurements in steady flow through axisymmetric stenosis at moderate reynolds numbers. *Journal of Biomechanics*, 16:505–516, 1983.

J. Anderson. *Computational Fluid Dynamics: the Basics with Applications*. McGraw-Hill, 1995.

C. Bailly, P. Lafon, and S. Candel. Computation of noise generation and propogation for free and confined turbulent flows. *2nd AIAA/CEAS Aeroacoustics Conference, State College*, 96:1732, 1996.

J. Baun. *Physicial Principles of General and Vascular Sonography*. Internet production, 2009.

K. Brentner and F. Farassat. An analytical comparison of the acoustic analogy and kirchhoff formulations for moving surfaces. *AIAA Journal*, 36:1379–1386, 1998.

M. Breuer, B. Kniazev, and M. Abel. Development of wall models for les of separated flows using statistical evaluations. *Computers and Fluids*, 36:817–837, 2007.

M. Brouns, S. Verbanck, J. van Beeck, S. Vanlanduit, J. Vanherzeele, and C. Lacor. Piv on the flow of a simplified upper airway model. *13th Int Symp on Applications of Laser Techniques to Fluid Mechanics, Lisbon, Portugal*, (1120), 2006.

M. Brouns, S. Jayaraju, C. Lacor, J. de Mey, M. Noppen, W. Vincken, and S. Verbanck. Tracheal stenosis: a flow dynamics study. *J Appl Physiol*, 102:1178–1184, 2007.

R. Calay, K. Kurujareon, and A. Holdo. Numerical simulation of respiratory flow patterns within human lungs. *Respiratory Physiology and Neurobiology*, 130:201–221, 2001.

D. Caridi. *Industrial CFD Simulation of Aerodynamic Noise*. PhD thesis, Università degli Studi di Napoli Frederico II, 2008.

CES-Edupack. *Material Database Software*. Granta Design Limited, Cambridge, UK, 2011.

X. Chen, X. Zhang, C. Morfey, and P. Nelson. A numerical method for the computation of sound radiation from an unflanged duct. *Journal of Sound and Vibration*, 270:573–586, 2004.

J. Claes, A. Boudewyns, P. Deron, V. van der Poorten, and H. Hoeve. Management of stridor in neonates and infants. *B-ENT*, 1:113–122, 2005.

R. Cotton and J. Reilly. *Congential Malformations of the Larynx.* Number 1299-1306. Saunders, Philadelphia, 3 edition, 1996.

N. Curle. The influence of solid boundaries upon aerodynamic sound. *Proceedings of the Royal Society of London*, 231:505–514, 1955.

J. de Backer, W. Vos, C. Gorlé, P. Germonpré, B. Partoens, F. Wuyts, P. Parizel, and W. de Backer. Flow analysis in the lower airways: Patient - specific model and boundary conditions. *Medical Engineering and Physics*, 30(7):872–879, 2008a.

J. de Backer, W. Vos, S. Verhulst, and W. de Backer. Novel imaging techniques using computer methods for the evaluation of the upper airway in patients with sleep-disordered breathing: A comprehensive review. *Sleep Medicine Reviews*, 12:437–447, 2008b.

E. Dekker. Transition between laminar and turbulent flow in human trachea. *J Appl Physiol*, 16:1060–1064, 1961.

M. Escobar. *Finite Element Simulation of Flow-Induced Noise using Lighthill's Acoustic Analogy.* PhD thesis, Technischen Fakultät der Universität Erlangen-Nürnberg, 2007.

F. Farassat. Introduction to generalized functions with applications in aerodynamics and aeroacoustics. *NASA Technical Paper*, 3428, 1996.

F. Farassat and H. Tadghighi. Can shock waves on helicopter rotors generate noise? a study of quadrupole sources. *Annual Forum Proc American Helicopter Society*, 1(323-346), 1990.

M. Farhadi and M. Rahnama. Large eddy simulation of separated flow over a wall-mounted cube. *Scientific Iranica*, 13(2):124–133, 2006.

A. Farkas and I. Balásházy. Simulation of the effect of local obstructions and blockage on airflow and aerosol depostion in central human airways. *Aerosol Science*, 38:865–884, 2007.

W. Finlay, K. Stapleton, and J. Yokota. On the use of computational fluid dynamics for simulating flow and particle deposition in the human respiratory tract. *Journal of Aerosol Medicine*, 9(3):329–341, 1996.

X. Gloerfelt and P. Lafon. Direct computation of the noise induced by a turbulent flow through a diaphragm in duct at low mach number. *Computers and Fluids*, 37:388–401, 2007.

D. Hanson and M. Fink. The importance of quadrupole sources in prediction of transonic tip speed propeller noise. *Journal of Sound and Vibration*, 62(1):19–38, 1979.

A. Haton, S. Hopkins, W. Johnson, D. McLaughlin, and J. LaHart. *Human Biology and Health.* Number ISBN 0-12-981176-1 108-118. Englewood Cliffs: Prentice Hall, 2009.

A. Heenan, E. Matida, A. Pollard, and W. Finlay. Experimental measurements and computational modeling of the flow field in an idealized human oropharynx. *Experiments in Fluids*, 35:70–84, 2003.

J. Hirschberg. Acoustic analysis of pathological cries, stridors and coughing sounds in infancy. *International Journal of Pediatric Otorhinolaryngology*, 2:287–300, 1980.

Y. Hu, P. Liao, W. Shih, X. Wang, and P. Chang. Study on the acoustic impedance matching of human tissue for power transmitting/charging system of implanted biochip. *IEEE 3rd International Conference on Nano/Molecular Medicine and Engineering*, pages 201–205, 2009.

Y. Huang, A. Malhotra, and D. White. Computational simulation of human upper airway collapse using a pressure-/state-dependent model of geniosglossal muscle contraction under laminar flow conditions. *J Appl Physiol*, 99:1138–1148, 2005.

S. Hulshoff. Ae4133 part 2: Computation and modelling of turbulence. course notes. Technical report, Aerodynamics Department, Faculty of Aerospace Engineering, Delft University of Technology, 2011.

R. Issa. Solution of the implicitly discretised fluid flow equations by operator-splitting. *Journal of Computational Physics*, 62:40–65, 1986.

H. Jasak and H. Weller. Application of the finite volume method and unstructured meshes to linear elasticity. *International Journal for Numerical Methods in Engineering*, 48:267–287, 2000.

S. Jayaraju, M. Brouns, C. Lacor, B. Belkassem, and S. Verbanck. Large eddy and detached eddy simulations of fluid flow and particle deposition in a human mouth–throat. *Aerosol Science*, 39:862–875, 2008.

S. Jeong, W. Kim, and S. Sung. Numerical investigation on the flow characteristics and aerodynamic force of the upper airway of patient with obstructive sleep apnea using computational fluid dynamics. *Medical Engineering and Physics*, 29:637–651, 2007.

K. Keyhani, P. Scherer, and M. Mozell. Numerical simulation of airflow in the human nasal cavity. *Biomechanical Engineering*, 117:429–441, 1995.

G. Kirchhoff. Theorie der lichtstrahlen. *Annalen der Physik und Chemie*, 18:663–695, 1883.

T. Klassen. Croup. a current perspective. *Pediatric Clinical North America*, 46:167–178, 1999.

M. Lalakea and A.H. Messner. Retropharyngeal abscess management in children. *Otolaryngol Head Neck Surg*, 121:398–405, 1999.

A. Leiberman, A. Cohen, and A. Tal. Digital signal processing of stridor and snoring in children. *International Journal of Pediatric Otorhinolaryngology*, 12:173:185, 1986.

M. Lighthill. On sound generated aerodynamically i: General theory. *Proceedings of the Royal Society of London*, 211:564–587, 1952.

G. Link, M. Kaltenbacher, M. Breuer, and M. Dollinger. A 2d finite-element scheme for fluid-solid-acoustic interactions and its application to human phonation. *Comput. Methods Appl. Mech. Eng.*, 198:3321–3334, 2009.

K. Liow, M. Thompson, and K. Hourigan. Computation of acoustic waves generated by a co-rotating vortex pair. *14th Australasian Fluid Mechanics Conference*, 2001.

G. Ludwig. The velocity of sound through tissue and the acoustic impedance of tissues. *The Journal of the Acoustical Society of America*, 2(6):862–866, 1950.

H. Luo and Y. Liu. Modeling the bifurcation flow in a ct-scanned human lung airway. *Journal of Biomechanics*, 1:2681–2688, 2008.

X. Luo, J. Hinton, T. Liew, and K. Tan. Les modelling of flow in a simple airway model. *Medical Engineering and Physics*, 26:403–413, 2004.

C. Lynch. The numerical and acoustic and fluid flow analysis on a ct-scan derived upper airway model. Master's thesis, Aerodynamics Department, Faculty of Aerospace Engineering, Delft University of Technology, 2012.

S. Majumdar. Paediatric stridor. *Arch Dis Child Educ Pract Ed*, 91:101–105, 2006.

M. Mihaescu, S. Murugappan, M. Kalra, S. Khosla, and E. Gutmarka. Large eddy simulation and reynolds-averaged navier–stokes modeling of flow in a realistic pharyngeal airway model: An investigation of obstructive sleep apnea. *Journal of Biomechanics*, 41:2279–2288, 2008.

P. Milenkovic. Vocal area functions from two-point acoustic measurements with formant frequency constraints. *IEEE Transactions on Acoustics, Speech and Signal Processing*, 32 (6):1122–1135, 1984.

B. Mitchell, S. Lele, and P. Moin. Direct computation of the sound from a compressible co-rotating vortex pair. *Journal of Fluid Mechanics*, 285:181–202, 1995.

M. Miyamoto, Y. Ito, K. Takahashi, T. Takami, T. Kobayashi, A. Nishida, and M. Aoyagi. Numerical study on sound vibration of an air-reed instrument with compressible les. *Physics Fluid Dynamics*, 2010.

A. Modrykamien, R. Gudavalli, K. McCarthy, X. Liu, and J. Stoller. Detection of upper airway obstruction with spirometry results and the flow-volume loop: Detection of upper airway obstruction with spirometry results and the flow-volume loop: A comparison of quantitative and visual inspection criteria. *Respiratory Care*, 54(4):474–479, 2009.

G. Mylavarapu, S. Murugappan, M. Mihaescu, M. Kalra, S. Khosla, and E. Gutmark. Validation of computational fluid dynamics methodology used for human upper airway flow simulations. *Journal of Biomechanics*, 42:1553–1559, 2009.

D. Olsen, M. Sudlow, K. Horsfield, and G. Filley. Convective patterns of flow during inspiration. *Arch Intern Med*, 131(1):51–57, 1973.

OpenFOAM. *OpenFOAM: The Open Source CFD Toolbox Programmer's Guide*, 2011.

M. Piellard and C. Bailly. Several computational aeroacoustics solutions for the ducted diaphragm at low mach number. *16th AIAA/CEAS Aeroacoustics Conference*, 2010.

M. Piellard and C. Bailly. Validation of a hybrid caa method. application to the case of a ducted diaphragm at low mach number. *14th AIAA/CEAS Aeroacoustics Conference*, 2008.

D. Rixen. Coupled analysis of structures and acoustics. Technical report, Delft University of Technology, 2010.

P. Sagaut, E. Montreuil, and O. Labbé. Assessment of some self-adaptive sgs models for wall bounded flows. *Aerospace Science and Technology*, 6:335–344, 1999.

F. Schmitz and Y. Yu. Helicopter impulsive noise theoretical and experimental status. *Journal of Sound and Vibration*, 109(3):361–427, 1986.

E. Slawinsky and D. Jamieson. Studies of respiratory stridor in young children: acoustical analyses and tests of a theoretical model. *International Journal of Pediatric Otorhinolaryngology*, 19:205–222, 1990.

J. Smagorinsky. General circulation experiments with the primitive equations. *Monthly Weather Review*, 91:99–164, 1996.

C. Spa, A. Garriga, and J. Escolano. Impedance boundary conditions for pseudo-spectral time-domain methods in room acoustics. *Applied Acoustics*, 71(5):402–410, 2010.

S. Standring. *39th Edition of Gray's Anatomy: The Anatomical Basis of Clinical Practice*. Elsevier, Churchill, Livingstone, 2008.

K. Stapleton, E. Guentsch, M. Hoskinson, and W. Finlay. On the suitability of k-e turbulence modeling for aerosol deposition in the mouth and throat: a comparison with experiment. *Journal of Aerosol Science*, 31(6):739–749, 2000.

S. Sung, S. Jeong, Y. Yu, C. Hwang, and E. Pae. Customized three-dimensional computational fluid dynamics simulation of the upper airway of obstructive sleep apne. *Angle Orthod*, 76 (5):791–799, 2006.

C. Testa. *Acoustic Formulations for Aeronautical and Naval Rotorcraft Noise Prediction Based on the Ffowcs Williams and Hawkings Equations*. PhD thesis, Università degli Studi di ROMA TRE, 2008.

S. Turteltaub. Continuum mechanics course notes ae3035 2009 - 2010. Technical report, Delft University of Technology, 2009.

S. Uosukainen. *Foundations of Acoustic Analogies*. VTT Publications, 2011.

W. van der Velden. Fluid-structure-acoustic interaction simulation of a patient's upper airway suffering from stridor. Technical report, Aerodynamics Department, Faculty of Aerospace Engineering, Delft University of Technology, 2012.

S. Verbanck, T. de Keukeleire, D. Schuermans, M. Meysman, W. Vincken, and B. Thompson. Detecting upper airway obstruction in patients with tracheal stenosis. *J Appl Physiol*, 109: 47–52, 2010.

C. Wagner, T. Hüttl, and P. Sagaut. *Large-Eddy Simulation for Acoustics*. Cambridge University Press, 2007.

Y. Wang, J. Wang, Y. Liu, S. Yu, X. Sun, S. Li, S. Shen, and W. Zhao. Fluid–structure interaction modeling of upper airways before and after nasal surgery for obstructive sleep apnea. *International Journal for Numerical Methods in Biomedical Engineering*, 2012.

F. White. *Fluid Mechanics.* McGraw-Hill, New York, 1994.

J. Ffowcs Williams and D. Hawkings. Sound generation by turbulence and surfaces in arbitrary motion. *Philosophical Transactions of the Royal Society of Londen A*, 264:321–342, 1969.

J. Xi, X. Si, J. Kim, and A. Berlinski. Simulation of airflow and aerosol deposition in the nasal cavity of a 5 year old child. *Journal of Aerosol Science*, 42:637–651, 2011.

G. Xia, M. Tawhai, E. Hoffman, and C. Lin. Airway wall stiffening increases peak wall shear stress: A fluid–structure interaction study in rigid and compliant airways. *Annals of Biomedical Engineering*, 38(5):1836–1853, 2010.

C. Xu, S. Sin, J. McDonough, J. Udupa, A. Guez, R. Arens, and D. Wootton. Computational fluid dynamics modeling of the upper airway of children with obstructive sleep apnea syndrome in steady flow. *Journal of Biomechanics*, 39(11):2043–2054, 2006.

D. You, H. Choi, M. Choi, and S. Kang. Control of flow-induced noise behind a circular cylinder using splitter plates. *AIAA Journal*, 36(11):1961–1967, 1998.

Z. Zhang, C. Kleinstreuer, and C. Kim. Micro particle transport and deposition in a human oral airway model. *Aerosol Science*, 33:1635–1652, 2002.

W. Zhu. *Aero-Acoustic Computations of Wind Turbines.* PhD thesis, Technical University of Denmark, Department of Mechanical Engineering, 2007.

J. Zwartenkot. Fast fourier spectral analysis of inspiratory stridor in children. Technical report, Department of Otorhinolaryngology Erasmus Medical Centre, Sophia Childrens Hospital Rotterdam, 2010.

J. Zwartenkot, H. Hoeve, and J. Borgstein. Inter-observer reliability of localization of recordered stridor sounds in children. *International Journal of Pediatric Otorhinolaryngology*, 74:1184–1188, 2010.